Technische Universität München

Fakultät für Physik

Lehrstuhl für Physik E19

Investigation of the structure and reactivity of nanostructured surfaces

Stanislav Pandelov

Vollständiger Abdruck der von der

Fakultät für Physik der Technischen Universität München

zur Erlangung des akademischen Grades eines

Doktors der Naturwissenschaften

genehmigten Dissertation.

Vorsitzender: Univ.- Prof. Dr. Manfred Kleber

Prüfer der Dissertation:

1. Univ.-Prof. Dr. Ulrich Stimming

2. Univ.-Prof. Dr. Dr. h.c. Alfred Laubereau

Die Dissertation wurde am 04.12.2006 bei der

Technischen Universität München eingereicht und durch die

Fakultät für Physik am 31.05.2007 angenommen.

Contents

Introduction

Whereas the 19-th century was the stage of the steam engine and the 20-th century was the stage of the internal combustion engine, it is likely that the 21st century will be the stage of the fuel cell. Fuel cells have captured the imagination of people around the world as the next great energy alternative. They are now on the verge of being introduced commercially, revolutionizing the present way of power production. Fuel cells can use hydrogen and oxygen, or air as a fuel, offering the prospect of supplying the world with clean, sustainable electrical power, heat and water.

This work is focused on the hydrogen evolution reaction, further called HER, since this reaction is of outmost importance in developing and improving fuel cell devices. It is directed principally towards hydrogen electrocatalysis using bi-metallic surfaces, such as Pd/Au(111) electrodes, due to their good catalytic properties and lower prize.

It was shown by now that the physical and chemical characteristics of deposited Pd layers on Au reveal enhanced catalytic properties [1-10]. Baldauf *et al.* [2] have pointed out that ultra-thin Pd overlayers on Au or Pt single crystal surfaces manifest an elevated reactivity with respect to formic acid oxidation. The catalytic properties of the Pd overlayers depend mainly on the film thickness, the surface crystallographic orientation, and the substrate material. Baldauf *et al.* assign these differences in the catalytic properties to the different atomic spacing of the pseudomorphic Pd films, which could alter the electronic properties of their surfaces. El-Aziz *et al.* [3] have investigated pseudomorphically grown Pd overlayers on Au(111), which show a slight decrease in reactivity towards CO adlayer oxidation compared to massive Pd(111) electrodes. This can be explained by geometric and electronic modification of the surface. In addition, Uosaki and coworkers [9] have found that the electrochemical behavior of epitaxially electrodeposited Pd thin layers formed on Au(111) and Au(100) were strongly dependent on their surface structure and thickness. It hase been reported that the epitaxially grown ultra thin Pd layers on Au(111) and Au(100) substrates revealed a very high electrocatalytic activity for the reduction of oxygen. Kibler *et al.* [5-7] have shown that the electrochemical characterization of pseudomorphic Pd overlayers on Au(111) compared to massive Pd(111) provides

important information about basic relations between structure and reactivity. They supposed that the impact of Pd film thickness on the adsorption behavior and the reactivity can be explained by a change in lateral strain due to pseudomorphic growth that approaches bulk behavior for thicker layers. Stimming and coworkers [11-14] reported that the reactivity regarding hydrogen evolution reaction measured by STM tip at a single supported Pd nanoparticle on Au(111) is two orders of magnitude higher compared to bulk Pd. This finding can be explained with the spillover of adsorbed hydrogen from Pd particle to the Au(111) substrate. New scientific question about the origin of the enhancement of the reactivity of Pd nanoparticle on Au(111) arises. Several theoretical calculations attribute the enhanced reactivity of Pd/Au(111) systems to the change in the electronic structure of the Pd layers [15-25]. Hammer *et al.* [15-17] applied density functional theory to calculate adsorption properties and activation energies for surface chemical reactions. It has been shown that the electronic and geometrical factors can be separated and that both are important for the reactivity. The low coordinated or "expanded" metal atoms are more reactive than highly coordinated or "compressed" metal atoms. Rojas *et al.* [26, 27] report that the adsorption energy decreases with increasing of the coverage degree of Pd adlayer on Pd, Au and Pt substrates.

All these investigations illustrate that the reactivity regarding the hydrogen evolution reaction of Pd/Au(111) depends strongly on the electronic properties and the geometry of the surface. A more detailed research in this direction will probably enable a better understanding of the catalytic properties of adlayers. The purpose of the work is to develop a model, which can explain the catalytic properties of metal layers in the monolayer and sub monolayer range, e.g. Pd monolayers on Au(111). Therefore, the dependence of the number of deposited monolayers on the reactivity will be investigated. The case of sub-monolayers coverage will be studied in more details because of its simplified morphology parameters. The aim of this work can be achieved through Frank van-der-Merwe monolayer by monolayer growth mode [28, 29]. The last can be achieved only in systems where under potential deposition (UPD) occurs. Naohara *et al.* [30, 31] have shown that in $HClO_4 + PdCl_4^{2-}$ solution palladium grows monolayer by monolayer for the first three or four monolayers. Also Kolb and co-workers [32] have found that in solution from 0.1 mM H_2PdCl_4 in 0.1 M H_2SO_4 the first two deposited Pd monolayers grow layer by layer on Au(111). Additionally, they pointed out that the same result can be achieved in solution

from 0.1 mM $PdSO_4$ in 0.1 M H_2SO_4 [33]. The above presented facts support the suggestion, that it is possible to deposit Pd monolayers on Au(111) in perchloric acid solutions. The Pd/Au(111) samples were prepared in chloride-free solution to avoid their chloride contamination.

In the first chapter of this work a theoretical survey of the experimental techniques and reactions is presented. Chapter 2 contains the experimental set-up, preparation and characterization of the Au(111) substrates and the STM tips. In addition the preparation of pH micro- and nano-sensors is discussed.

The experimental result of the electrochemical deposition of Pd on Au(111) from 0.5 mM $Pd(NO_3)_2$ in 0.1 M $HClO_4$ solution are reported and discussed in chapter 3. Additionally, the deposition of Pd nano-islands with narrow size distribution is explained.

In chapter 4 the characterization and the stability of the deposited Pd monolayers and nano-islands on Au(111) are presented. Furthermore FTIR and XPS measurements are discussed.

The last chapter exhibits the results and the discussions of the reactivity measurements regarding hydrogen evolution reaction on Pd monolayers and monoatomically high nano-islands in 0.1 M $HClO_4$ solution. Theoretical model and explanations of the results are also presented.

Chapter 1

Basic theory of the experimental techniques and reactions

In the present chapter a short overview of the theoretical aspects of the used techniques is presented in order to achieve a better understanding of the experimental results of this thesis. At the beginning the basic principles of scanning tunneling microscopy (STM) are described and the case of STM in electrolytes is included, subsequently. Additionally, the basic theories of the measurement techniques are briefly explained and finally the theoretical principles of the hydrogen evolution reaction are discussed.

1.1 Scanning Tunneling Microscopy

Since its invention by Binning and Rohrer in 1982 [34], the Scanning Tunneling Microscope (STM) has become a frequently used tool in surface science. Its setup basically consists of a sharp metal tip which in the ideal case has only a single apex atom, i.e. it is mono-atomically sharp (Fig. 1.1). Using piezo-crystals as x,y,z-drivers this tip can be moved in all three dimensions on a 0.01 Å scale. If the tip is moved close to the sample (up to a distance in the range of a 0.5-2 nm) electrons can tunnel through the barrier from the tip into the surface and vice versa. In the case of a conductive sample and with an applied

bias voltage this effect can lead to a current of electrons tunneling between the systems. This tunneling current, typically in the order of a few nA is the basic unit measured in a STM experiment. The tunneling current depends exponentially on the tip-surface distance. This property of the tunneling current plays a significant role in STM and allows to control the sample-tip distance with high vertical resolution. An STM image is obtained while the tip scans over the surface and corresponds quite closely to the topography of the surface electronic states. The principle of the STM is schematically shown in Fig. 1.1.

The models for the explanation of the tunneling effect between two electrodes have been modified and improved during the time. In 1963 Simons [35] found a relation which explained the tunneling of electrons through a vacuum barrier without consideration of the geometry of the contacting surfaces (equation 1.1).

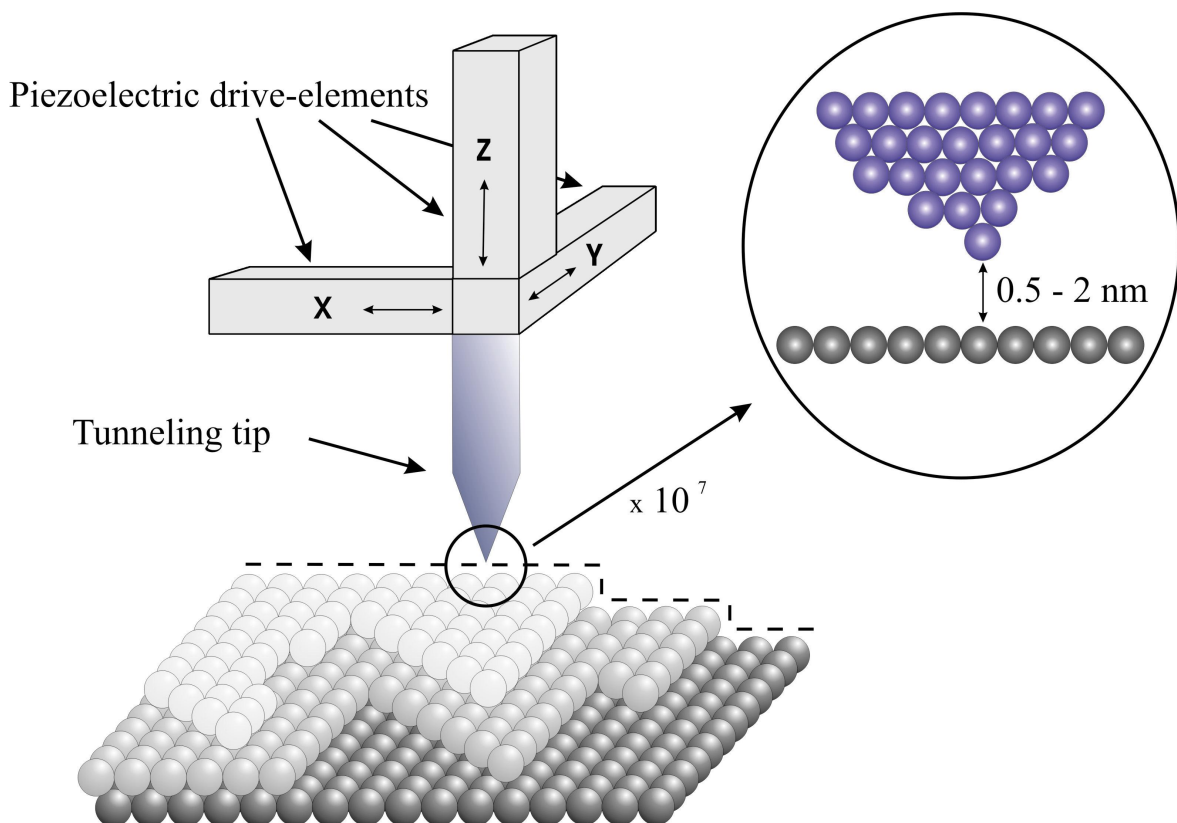**Fig.1.1:** The principle setup of STM. The tip is attached to the piezoelectric drive-elements which can move the tip in x-, y-, z- directions. The STM tip scans over the substrate in x-, y- directions. The STM image is obtained by recording the movement of the tip in z- direction referring to a defined x-, y- position or by recording the changes in the tunneling current at constant height (z is constant).

Simmons's model pointed out that the tunneling current I_T reveals an exponential dependence on the distance between the tip and the sample surface *s* and the barrier height ϕ_T.

Also, the tunneling current depends proportionally to the applied tunneling bias U_T. One important parameter in the characterization of the tunneling processes is the barrier height (see Fig.1.2) and can be experimentally defined by measuring the tunneling current I_T as a function of the distance between the tip and the sample surface *s*. From the barrier height the work function of the sample can be defined. Since its value depends on the material and the crystal orientation it can be used to characterize these properties of a sample surface on a nanometer scale.

Subsequently, the model of Simmons was improved from Tersoff and Hamann [36, 37] taking into account the surface geometry of the tunneling tip. In this improved model the

$$I_T \propto U_T e^{-2As} \qquad (1.1)$$

I_T	:	Tunneling current
U_T	:	Applied tunneling bias
Φ_T	:	Barrier height
s	:	Tunneling distance (distance tip-sample surface)
A	:	$\dfrac{\sqrt{2m_e\Phi_T}}{\hbar}$, m_e - mass of the electron
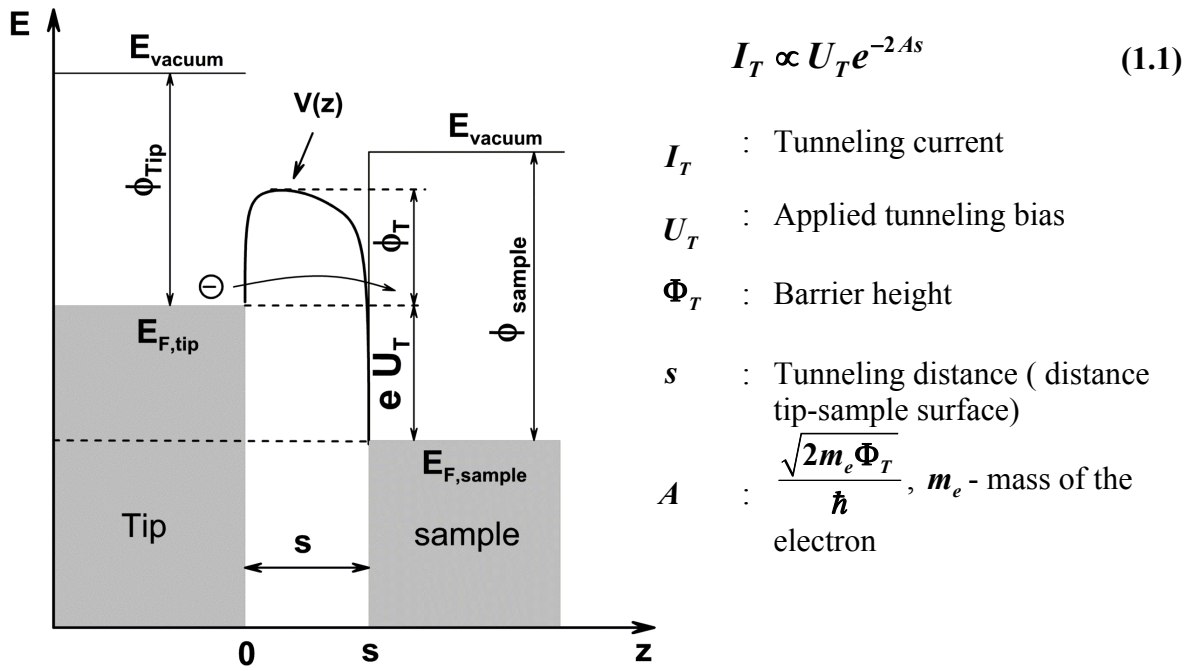
Fig.1.2: Schematic representation of the band model of the electron tunneling between two electrodes. ϕ_{Tip} and ϕ_{sample} are the work functions of the tip and the sample surface, respectively. $E_{F,i}$ is the fermi level of the tip and the surface, E_{vacuum} energy of vacuum, U_T the applied bias voltage. At the equilibrium the Fermi levels of the tip and the sample are equal. By applying a bias voltage the Fermi level of the tip (or of the sample) will be shifted and electrons will tunnel from one side to another one. The tunneling current arising in such a case is given by Eq. 1.1, where Φ_T is the height of tunneling barrier.

wave-function of the outermost tip atom is assumed to be an atomic s-wave-function. Since the tunneling current depends on the overlap of the wave-functions of the tip and the sample, and since the wave-function decays exponentially in vacuum, only the orbitals localized at the outermost tip atom will be of importance for the tunneling process. The tip can be modelled as a locally spherical potential (Fig.1.3), with curvature R around the center r_0. According to this model the tunneling current is proportional to the density of states of the tip and sample, Eq. 1.2, where ϕ is the work function of both the tip and the sample (for simplicity assumed to be equal), ζ_T and ζ_S are the density of states, respectively.

As it can be seen from Eq. 1.2, the tunneling current depends not only on the tip-sample distance but also on the electronic structure of the sample and the tip. For several materials of the tip, as metals, such contribution can be assumed to be minimal and the final STM image can be usually attributed only to the electronic properties of the sample. This is highly desirable due to the fact that we wish to study the sample, not the tip. A quantitative interpretation of STM images in terms of a measured tunneling current as a function of the bias voltage, tip-sample distance, and further details of tip and sample is obviously impossible within this model. The great success of the Tersoff-Hamann [36, 37] model is the possibility of qualitative interpretation of STM images. This justifies the seemingly crude assumptions, and it is an excellent starting point for the interpretation of STM data.
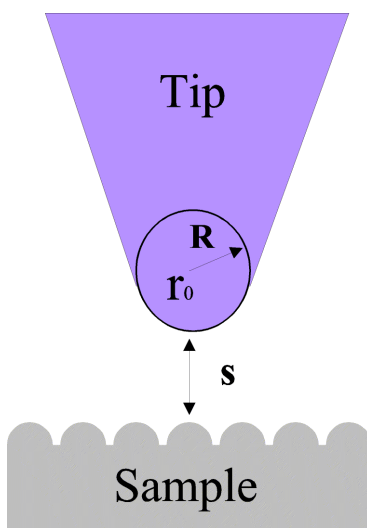
$$I_T = \frac{32\pi^3 e^2}{\hbar} U_T \frac{\phi^2}{A^4} R^2 \zeta_T(E_F) e^{2AR} \zeta_S(r_0, E_F) \qquad (1.2)$$

where $\quad \zeta_S(r_0, E_F) \propto e^{-2A(R+s)}$

e	:	Elementary charge
$\hbar$	:	Planck's constant
ϕ	:	Work function of the tip and the surface
ζ_T	:	Density of states (tip)
ζ_S	:	Density of states (sample)

Fig.1.3: The Tresoff-Haman [36, 37] presentation of the tunneling geometry. The tip is assumed to have a spherical shape with radius **R** and center **r₀**.

1.1.1 Tunneling in electrolytes

In 1986, Hansma and coworkers [38] demonstrated for the first time, that the scanning tunneling microscopy can be used in a liquid medium. Soon afterwards, atomic resolution of a surface in organic solution was achieved [39]. Subsequently, after series of improvements the electrochemical scanning tunneling microscopy (EC-STM) become a powerful instrumentation for investigations of the solid/liquid interfaces. Besides that, a lot of electrode processes as potential-induced surface reconstruction were for first time *in situ* investigated using the EC-STM. Furthermore, the investigation of the initial stages of metal deposition becomes available by using EC-STM technique. Zhang *et al.* [40] observed for first time copper dissolution from the electrode surface within a nanometer resolution. Hugelmann *et al.* [41] demonstrated that the tunneling process at the solid/liquid interface depends on the actual configuration of interfacial water in the tunneling gap. It was concluded that the tunneling spectroscopy in liquids should be sensitive to electronic states of solvent molecules or adsorbates in the tunneling gap.

Fig. 1.4 shows a schematic drawing of an EC-STM. The STM-tip is dipped into an electrolyte-filled electrochemical cell during image recording. The EC-STM cells are actually four-electrode cells, where both the tip and the substrate are working electrodes. The investigated sample is the working electrode (WE). The reference electrode (RE) and the counter electrode (CE) ensure the control over electrochemical processes within the
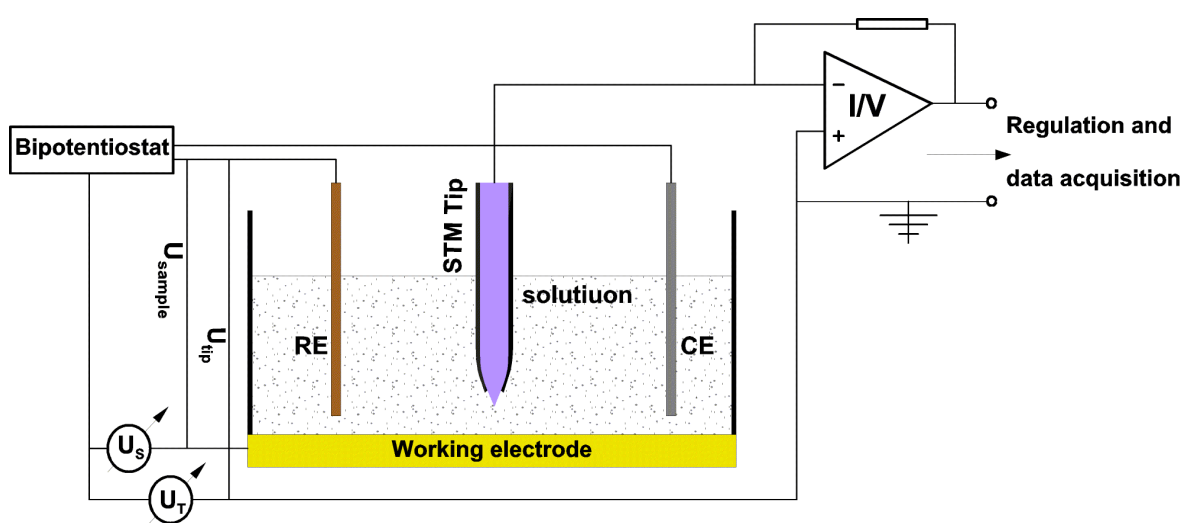

Fig.1.4: Schematic setup of an electrochemical scanning tunneling microscope. **RE** and **CE** are the reference and counter electrode, respectively.

cell and at the working electrode surface. For the tunneling process a voltage bias is applied between the tip and WE. Therefore, the tip itself serves as an additional electrode within the cell. The total current, measured with the STM in an electrochemical environment, is given by the sum of the tunneling current and the Faradic current, the latter results from electrochemical processes both at the substrate-electrolyte and the exposed tip-electrolyte interface. Typical electrochemical currents are in the range of µA, too large to detect an underlying tunneling current down to several nA. Therefore, to reduce the unwanted contribution from the Faradic current to a small percentage, the exposed tip-electrolyte interfacial area has to be reduced. This can be achieved by coating the tip with an electrically insulating material, leaving only some 100 nm^2 of the tip end exposed. Thus, the residual Faradic current can usually be kept below 100 pA.

1.1.2 STM Operating Modes

For imaging surfaces the STM can be operated in constant current or constant height modes, both are schematically presented in Fig. 1.5.

Scanning tunneling microscopes are most commonly operated in constant current mode (Fig.1.5b) for imaging of structures with sizes in the range of several µm to several hundreds nm. In this mode, using an electronic feed-back loop, the vertical distance between tip and sample is adjusted to yield a constant tunneling current at each lateral position (x,y) of the sample. Scanning a surface in this mode and recording the changes in vertical distance Δz as a function of the lateral position (x,y) results in a topographic image $\Delta z(x,y)$ of the sample surface. The final STM image represents a 2D array of heights at some specific surface features. Due to the limitations of the feedback electronics and mechanical vibrations of the piezo-ceramics, this operation mode is commonly performed at relatively small scan rates.

In the constant height operating mode (Fig.1.5a) the height and bias are maintained constant simultaneously, whereas a variation of tunneling current is measured. These variations arise during scanning over different surface structures. The image in this case display changes of the tunneling current. One of the most important advantages of this mode is the faster scan rate, which is not limited by the time response in z-direction of the piezo-ceramics. However, this is useful only for very flat surfaces, such as silicon and

HOPG, for example, or very small scanning areas. Unfortunately, in this mode there is some danger to destroy the tip apex.
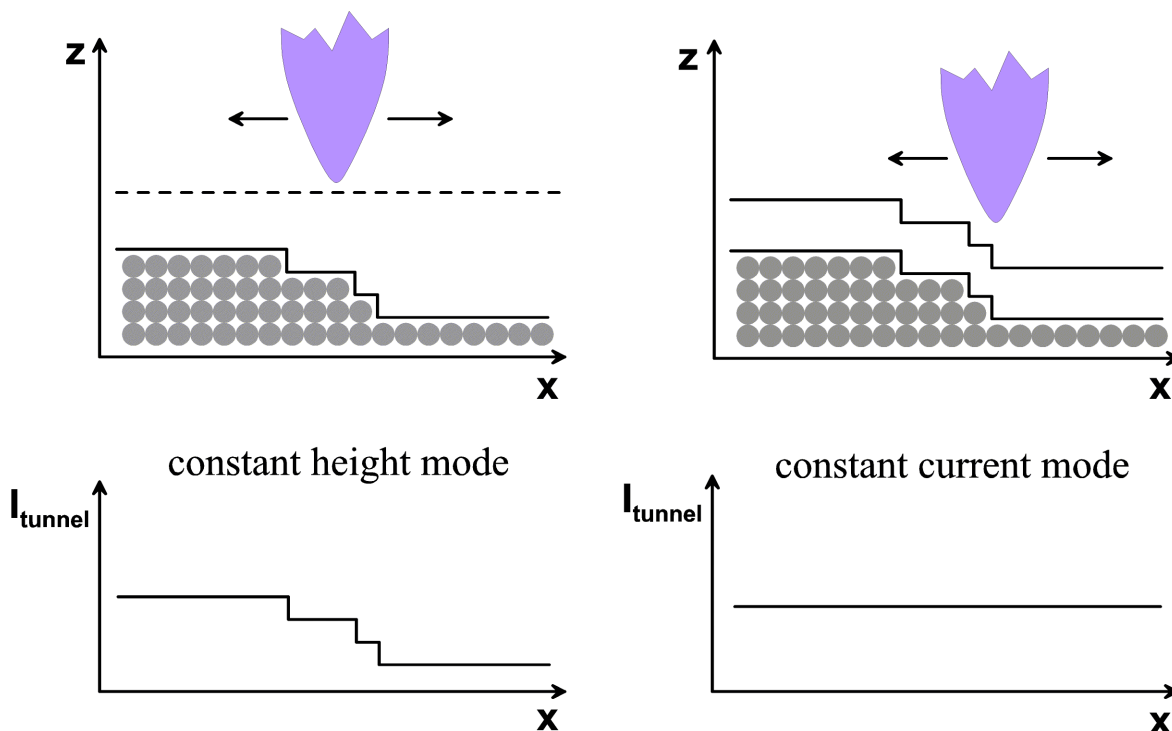
Fig.1.5: Schematic representation of the STM operating modes: (a) constant height, where changes of current are recorded and (b) constant current, where variations of height are measured.

1.2 Measurement techniques

1.2.1 Cyclic voltammetry

Cyclic voltammetry (CV) is one of the most frequently used electrochemical methods because of its relative simplicity and high information content [42]. The efficiency of the CV results from the capability for a rapid observance of the redox behavior over a wide potential range. Voltammetry is an electroanalytical method in which information about the investigated electrode is obtained from the measurement of current as a function of an applied potential. For the 3-electrode configuration, the potential is applied to the working electrode with respect to a reference electrode, and a counter electrode is used to complete the electrical circuit. The excitation wave in CV is a linear potential scan with a triangular

waveform, as shown in Fig.1.6. The potential is linearly scanned from an initial value U_i, to a predetermined limit U_f, where the direction of the scan is reversed. Cyclic voltammogram is obtained by measuring the current at the working electrode during the potential scan.
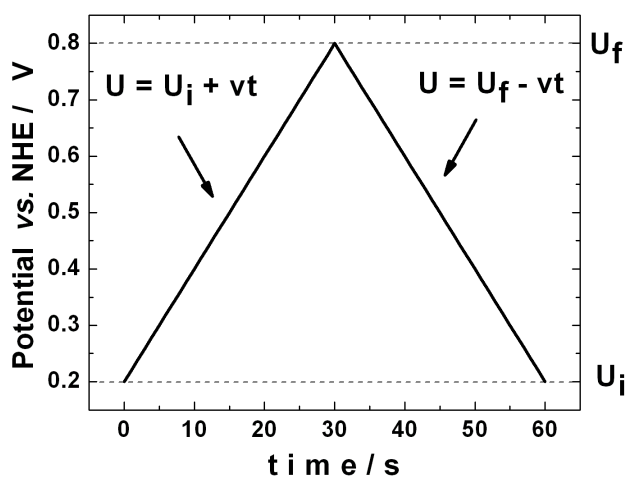
Fig.1.6: Potential sweep during cyclic voltammetric measurement. U_i is the initial potential, U_f is the predetermined turn-round potential and **v** is the sweep rate (V/s).

1.2.2 Pulse Techniques

It is well known from the literature that in electrochemistry two phenomena arise measuring at a long time scale [43]. The term "long" must be understood in a technical way. The first one is the impurity adsorption onto the electrode from the solution. Thus, the catalytic surface of the electrode is reduced or "poisoned". The second one is the influence of the limiting diffusion current. At longer time the overall reaction process is in diffusion control, i.e., the measured current is defined by the diffusion of ions from the solution to the electrode surface. Therefore, the measurement at "short times" "transients" has obvious advantages. The measured current density j can be written as the following equation [43]:

$$\frac{1}{j} = \frac{1}{j_F} + \frac{1}{j_L}$$
(1.3)

where j_F is the current density due to Faradaic electron-transfer processes and j_L is the limiting diffusion current density. Therefore, if one wants to obtain data dominated by the reaction at the interface, one has to be sure that some of the following condition is fulfilled:

$$j_F < 10 j_L \quad \text{- for } j \ 90 \text{ \% free from the influence of diffusion control}$$

$$j_F < 100 j_L \quad \text{- for } j \ 99 \text{ \% free from the influence of diffusion control}$$

Obviously, one needs to make j_L as large as possible in order to make realizable a diffusion-free measurement at a very high rate. This can be achieved, by using a rotation disk electrode or ultramicroelectrodes. Thus, j_L can be increased several orders of magnitude compared with its value at a flat plate in a still solution. To understand how can be increased the limiting diffusion current j_L in the case of a flat plate electrode in still solution, one must write the next equation:

$$j_L = \frac{DnFc}{\delta} = \frac{DnFc}{\sqrt{\pi Dt}} \tag{1.4}$$

where D is the diffusion constant of the reactant, n is the number of electrons in the reaction, F is the Faraday constant, c is the concentration of the reactant in the bulk and $\delta = \sqrt{\pi Dt}$ is the diffusion layer thickness. From equation (1.3) is clear that when j_L increases if t decreases. For example, at times of 0.1 ms and 1 s, j_L will be about 100 times larger at the lower times than at the higher one. Using short time measurements "transients" will give a big advantage in respect to the upper limits of current density at which an electrode kinetic measurement can be made free of diffusion control. The maximum measuring time of the transient can be calculated from equation (1.4) with respect to the conditions mentioned before. In the case of electrochemical reactions with adsorbed intermediate radicals, there is a danger of using transients. If the measuring time is made to short, to get a large j_L and eliminate diffusion regime, there will be not enough time for the intermediate reaction radicals to reach their steady-state surface coverage. Thus, the time range of the transient measurements should be considered also with the necessary time of steady-state surface coverage of the reaction intermediates.

1.2.3 Current pulse (Galvanostatic) technique

By galvanostatic transient measurements, one understands applying a current pulse at the electrode and measure the responding of the electrode potential as a function of the time. In Fig.1.7 a sketch of a basic galvanostatic experiment is shown. The applied current and the

measured potential transient are shown in Fig.1.7 (a) and (b), respectively. At time t_0 the current is switched from I_i to I_f. The starting potential is at U_i point A in Fig.1.7b. From A to B, the potential change is due to a IR drop between the end of the Luggin capillary and the electrode. During the time corresponding to B-C of the potential transient, two processes are occurring. The first one is the charging of the double layer to correspond to the change in the potential. This process is dominant at the lower time of the B-C potential transient range. The second one is the passage of electrons across the double layer to ions on the solution side, dominant at longer time of the B-C transient partition. In the period C to D, the double layer charging is almost finished and nearly all the current is going into the passage of electrons across the double layer. Insofar as C-D takes a significant time to become constant, this may be due to the settling down of the intermediate radicals taking part in the multistep electrode reaction.

The relaxation time τ of the double layer capacitance C_{DL} is given by [43]:

$$\tau = R_F C_{DL} \tag{1.5}$$

where R_F is the Faradaic resistance. The value of τ is important for calculation of the minimum time of the transient. Thus, t must be greater than τ to reach a steady state. Knowing the constant current applied to the circuit and the "final" potential in the C-D region, the value of the overpotential corresponding to the current can be estimated. Repeating the measurement for a series of constant currents densities allows plotting logj

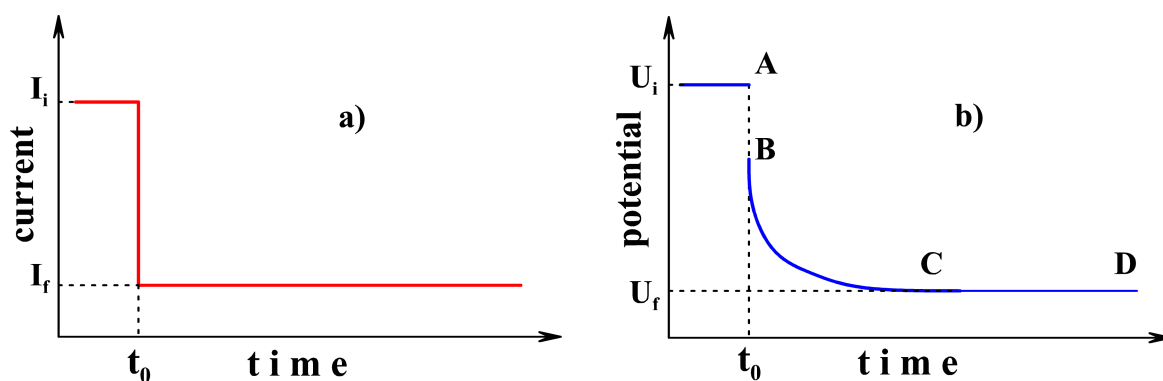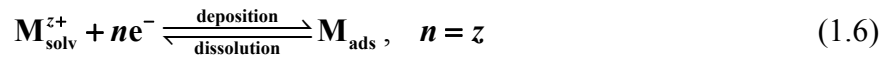**Fig.1.7:** Sketch of the galvanostatic technique. (a) The applied current, at time t_0 the current is switched from value I_i to I_f. (b) The corresponding response of the electrode potential, where U_i is the initial potential corresponding to the I_i, A-B is the IR drop, B-C is the double layer discharging and C-D is the constant potential U_f corresponding to the reaction current I_f.

as a function of the overpotential (Tafel plot). From those plots one can easily determine the exchange current density and the transfer coefficient (slope of the linear part of the plot) for the investigated electrochemical reaction.

1.3 Electrochemical deposition of metals

1.3.1 Thermodynamic and Kinetic Aspects

In this section the deposition of metals onto an electrode surface under the influence of an applied electric field will be discussed. The overall reaction of metal deposition can be written as [28, 42]:

$$\mathbf{M}^{z+}_{\text{solv}} + n\mathbf{e}^- \underset{\text{dissolution}}{\overset{\text{deposition}}{\rightleftharpoons}} \mathbf{M}_{\text{ads}} , \quad n = z \tag{1.6}$$

where $\mathbf{M}_{\text{ads}}$ are the deposited metal ions on the surface, $\mathbf{M}_{\text{solv}}$ are the solvated metal ions in the electrolyte and z is the valence of the metal ions.

The electrode potential at which the direction of the electrochemical reaction (1.6) changes is defined by the electrochemical equilibrium at the interface between the electrolyte and the electrode. An equilibrium at the interface layer is assumed when the electrochemical potentials (Fermilevels) of the species i of the substrate (S) and the electrolyte (El) are equal:

$$\tilde{\mu}_i^{(S)} = \tilde{\mu}_i^{(El)} \tag{1.7}$$

This condition is connected with an equilibrium potential (known also as Galvani potential difference) which can be calculated from the difference of the Galvani potentials of the electrolyte and the substrate. The equilibrium potential of an electrode cannot be separately measured only with respect to reference electrode.

Therefore in electrochemistry the equilibrium potential is measured compared to the standard hydrogen electrode (NHE). Thus, the obtained value represents exactly the equilibrium potential of the metal/electrolyte ($\mathbf{Me/Me^{z+}}$) electrode.

Using the Nernst equation, the equilibrium potential $U_{0,\,\mathbf{Me/Me^{z+}}}$ of a $\mathbf{Me/Me^{z+}}$ electrode is given by:

$$U_{0,\,\mathbf{Me/Me^{z+}}} = U^{\theta}_{\mathbf{Me/Me^{z+}}} + \frac{RT}{nF} \ln \frac{a_{\mathbf{Me^{z+}}}}{a_{\mathbf{Me}_{ads}}} \tag{1.8}$$

where $U_{0,\,Me/Me^{z+}}$ is the Nernst equilibrium potential, $U^{\theta}_{Me/Me^{z+}}$ is the standard potential of the

Me/Me^{z+} electrode, T is the temperature, **R = 8.314 J/molK** the molar gas constant,

F = 9.65 · 10^4 As/mol the Faraday constant and $a_{Me^{z+}}$ and $a_{Me_{ads}}$ are the activity of the

M^{z+}_{solv} ions in the electrolyte and the activity of the deposited metal, respectively. It is

assumed by convention that the activity of the deposited metal is equal to 1 ($a_{Me_{ads}} = 1$). In

the case of diluted solutions, for example, 0.001 molar or lower, the activity in Eq.1.8 can

be replaced by the concentration in mol/l, which yields to:

$$U_{0,\,Me/Me^{z+}} = U^{\theta}_{Me/Me^{z+}} + \frac{RT}{nF}\ln c_{Me^{z+}} = U^{\theta}_{Me/Me^{z+}} + 2.303\frac{RT}{nF}\log c_{Me^{z+}} \qquad (1.9)$$

where $c_{Me^{z+}}$ is the concentration of the metal ions M^{z+}_{solv} in the solution. Thus, the equilibrium

potential of the **Me/Me^{z+}** electrode varies with the concentration of the metal ions in the

solution. By increasing the metal ion concentration with one order of magnitude the

equilibrium potential increases at room temperature (T=298 K) by:

$$2.303\frac{RT}{nF} = \frac{59.2}{n}\;\text{mV} \qquad (1.10)$$

The actual electrode potential **U**, determines the direction in which will the reaction (1.6)

occurs. Hence, if the electrode potential is more negative as compared to the equilibrium

potential ($U < U_{0,\,Me/Me^{z+}}$) the reaction will run in the forward direction, i.e., one gets metal

deposition on the electrode surface. On the other hand, if the electrode potential is more

positive compared to the equilibrium potential ($U > U_{0,\,Me/Me^{z+}}$) the reaction will take place

in the reverse direction, i.e. metal dissolution from the electrode surface occurs.

The metal deposition begins with the nuclei formation of metal atoms on the electrode

surface. Usually, in most of the cases the nuclei emerges on top of a surface defect. Due to

that fact, the mechanisms of metal deposition on native (**Me**) or foreign (**S**) substrates is

strongly dependent on the density of defects on the substrate. The defects are classified on

their dimension as follows:

0D or point defects	Atom vacancies, chemical impurities

1D or linear defects   Steps and screw dislocations

2D or planar imperfections   Grain boundaries, stacking faults

3D or volume imperfections   Domains with different physical or chemical properties

Similar to the surface defects the metal deposition process can be classified by different stages:

0D   - Formation of nuclei or adatoms

1D   - Formation of an atomic row on the steps

2D   - Formation of monoatomic islands and overlayers

3D   - Formation of multilayer 3D islands

With decreasing of the electrode potential the possibility to higher dimensional mechanism increases will occurs:

$$U_{3D\,Me} < U_{2D\,Me} < U_{1D\,Me} < U_{0D\,Me} \tag{1.11}$$

Which "growth mode" type will occur depends on some additional parameters which will be explained later in section (1.3.3).

1.3.2 Underpotential and overpotential deposition

In the previous section have been shown that metal **Me** will be deposited from the solution of M_{solv}^{z+} ions if the electrode potential U is more negative than the Nernst potential of the electrode **Me/Me^{z+}**. Nevertheless, it is known that in many cases metal **Me** can be deposited on a foreign substrate **S** from a solution of M_{solv}^{z+} ions at potentials more positive than the Nernst equilibrium potential of **Me/Me^{z+}** electrode. This electrodeposition of metals is called underpotential deposition (UPD). Therefore, in terms of the actual electrode potential U during deposition and the Nernst equilibrium potential $U(\textbf{Me/Me}^{z+})$ and their difference $\Delta U = U - U(\textbf{Me}/\textbf{Me}^{z+})$, two types of electrodeposition can be distinguished [28, 29]:

       1.   Overpotential deposition, OPD:

$$\Delta U < 0, \qquad U < U(Me/Me^{z+})$$

2. Underpotential deposition, UPD:

$$\Delta U > 0, \qquad U > U(Me/Me^{z+})$$

1.3.3 Metal deposition on a foreign metallic substrate – mechanisms

In the catalysis the metal deposition on a foreign metallic substrate is a very important technique because of the possibility to modify the catalytic properties of the deposited metal. The growth mechanism of metal $\mathbf{Me_{ads}}$ on a foreign metallic substrate $\mathbf{S}$ is determined by two important parameters: first the binding energy between $\mathbf{Me_{ads}\text{-}S}$ and $\mathbf{Me_{ads}\text{-}Me_{ads}}$ and second the crystallographic misfit between $\mathbf{S}$ and 3D $\mathbf{Me}$ bulk deposit, which is defined by [28]:

$$\mathbf{mf} = \frac{d_{0,Me} - d_{0,S}}{d_{0,S}} \tag{1.12}$$

where $d_{0,Me}$ and $d_{0,S}$ are the bulk interatomic distances of the deposit $\mathbf{Me}$ and substrate $\mathbf{S}$, respectively. In the upcoming discussion the deposition process is assumed at nearly equilibrium conditions, negligible kinetic and supersaturating influences and disregarding the alloy formation between depositing metal $\mathbf{Me}$ and the substrate $\mathbf{S}$. So, three "growth modes" are possible changing these two parameters, schematically illustrated in Fig.1.8.

1) The first "growth mode" is called "Vollmer-Weber", known as 3D island formation. This mode is possible when the binding energy between the metal adions $\mathbf{Me_{ads}}$ and the foreign substrate $\mathbf{S}$, $\psi_{Me_{ads}\text{-}S}$, is smaller than between $\mathbf{Me_{ads}}$ and the native substrate $\mathbf{Me}$, $\psi_{Me_{ads}\text{-}Me}$. In this case the crystallographic misfit do not have any effect [28].

2) The second "growth mode" is "Frank von-der-Merve" or layer-by-layer formation. The conditions at which this growing mode occurs are: first the binding energy of the metal adions $\mathbf{Me_{ads}}$ on the foreign substrate $\mathbf{S}$, $\psi_{Me_{ads}\text{-}S}$, is larger than that of $\mathbf{Me_{ads}}$ on native substrate $\mathbf{Me}$, $\psi_{Me_{ads}\text{-}Me}$ and second the crystallographic misfit is negligible small $\mathbf{mf} \approx 0 \implies d_{0,S} \approx d_{0,Me}$ (Fig.1.8b).
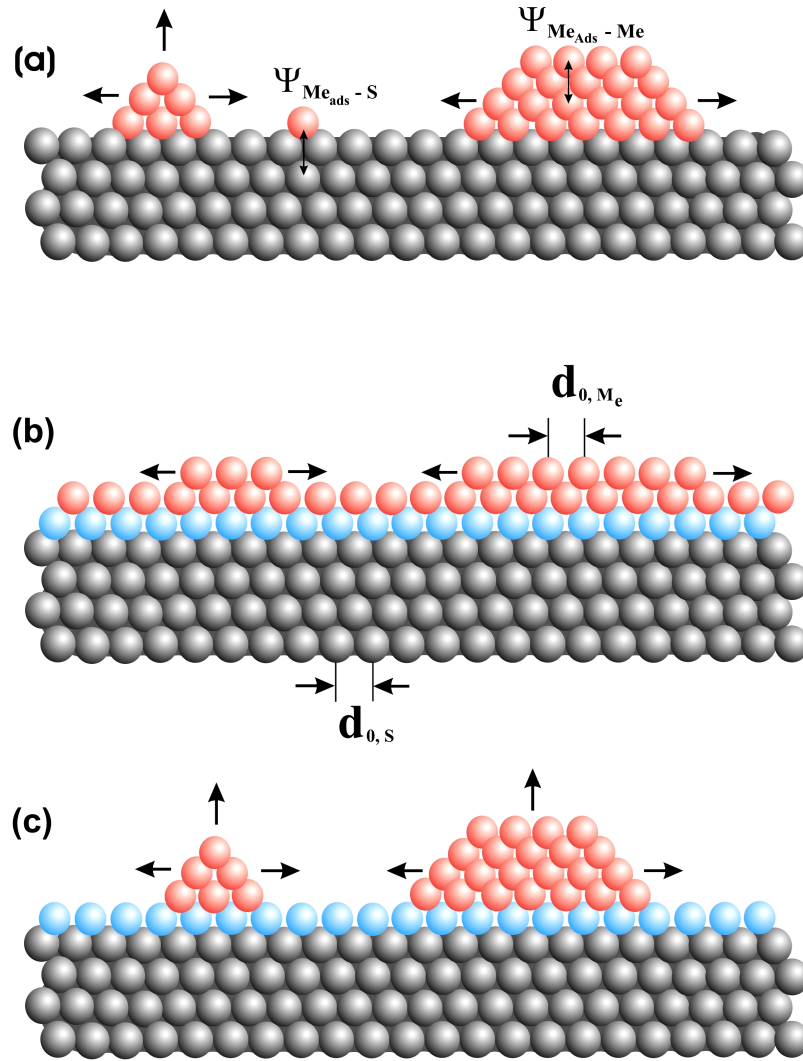
Fig.1.8: Schematic representation of the different "growth modes" of metal (**Me**) deposition on foreign substrate (**S**). The growth modes depends on the comparison between the two binding energies $\psi_{Me_{ads}\text{-}Me}$ (between Me_{ads} and native substrate Me) and $\psi_{Me_{ads}\text{-}S}$ (between Me_{ads} and foreign substrate **S**). The second parameter determining the growth modes is the crystallographic misfit, which is defined as: $\mathbf{mf = (d_{0,Me} - d_{0,S})/d_{0,S}}$

(a) "Volmer-Weber" growth mode (3D Me island formation) for $\psi_{Me_{ads}\text{-}S} \ll \psi_{Me_{ads}\text{-}Me}$ independent of the value for $\mathbf{mf}$.

(b) "Frank van-der-Merwe" growth mode (layer- by- layer formation) for $\psi_{Me_{ads}\text{-}S} \gg \psi_{Me_{ads}\text{-}Me}$ and $\mathbf{mf \approx 0}$.

(c) "Stranski-Krastanov" growth mode (3D **Me** island formation on top of predeposited 2D $\mathbf{Me_{ads}}$ overlayers on **S**) for $\psi_{Me_{ads}\text{-}S} \gg \psi_{Me_{ads}\text{-}Me}$ and $\mathbf{mf < 0}$ (negative misfit) or $\mathbf{mf > 0}$ (positive misfit).

In this mode the deposited metal is growing in a 2D-manner. This means that the deposition of the next layer starts when the previous layer is complete.

3)   The third growth mode is "Stranski-Krastanov". The conditions at which this growing mode occurs are: first the binding energy of the metal adions $\mathbf{Me_{ads}}$ on the foreign substrate $\mathbf{S}$, $\psi_{\mathbf{Me_{ads}\text{-}S}}$, is larger than that of $\mathbf{Me_{ads}}$ on the native substrate $\mathbf{Me}$, $\psi_{\mathbf{Me_{ads}\text{-}Me}}$, similar to the "Frank van-der-Merve" growth mode and second the crystallographic misfit is significant $d_{0,S} \neq d_{0,Me}$. In this case the growth mode is composed of two steps. In the first step a 2D overlayer of $\mathbf{Me_{ads}}$ on $\mathbf{S}$ is formed, and in the second step 3D crystallites grow on top of this predeposited overlayer. The predeposited overlayer contains considerable internal strains, because of the different structure between the predeposited overlayer and the 3D Me bulk phase.

1.3.4 Instantaneous and progressive nucleation

Let $N(t)$ be the number of nucleation centers per unit area at time t. Following Schmickler [44], we assume "first-order kinetics" as follows:

$$N(t) = N_\infty \left[1 - \exp(-k_N t) \right] \qquad (1.13)$$

where k_N is the nucleation rate and N_∞ is the number of active sites on the electrode surface, respectively. There is no reason to believe that the nucleation rate follows some sort of first-order restoring force as $dN/dt = k(N_\infty - N)$, upon which (1.13) depends. But this formula allows an interpolation between two limiting cases, often described in the literature. "Instantaneous" nucleation refers to a situation where the all-possible nuclei have formed before the time of observation of the system. This corresponds to $k_N t \gg 1$ in equation (1.13) and yields to $N(t) = N_\infty$. "Progressive nucleation" refers to the opposite limiting case, where the nucleation process is at its early phase throughout the time of observation. This corresponds to $k_N t \ll 1$ in equation (1.13) and yields to a linearized $N(t) = N_\infty k_N t$.

Of course, these are only limiting cases. In general it is possible to find a system which exhibit both types of behavior, depending upon the rate of nucleation k_N (which may be controllable) and the time scale of the measurement.

Fig.1.9 shows these two cases compared schematically. For each column, the time axis runs downwards. In the instantaneous case (left side), all of the nucleation occurs before the first slide. As time advances, each island grows larger, but no new ones are nucleated. In the progressive case (right side), some islands have already nucleated before the first slide. However, islands continue to be nucleated even as their older siblings grow larger.
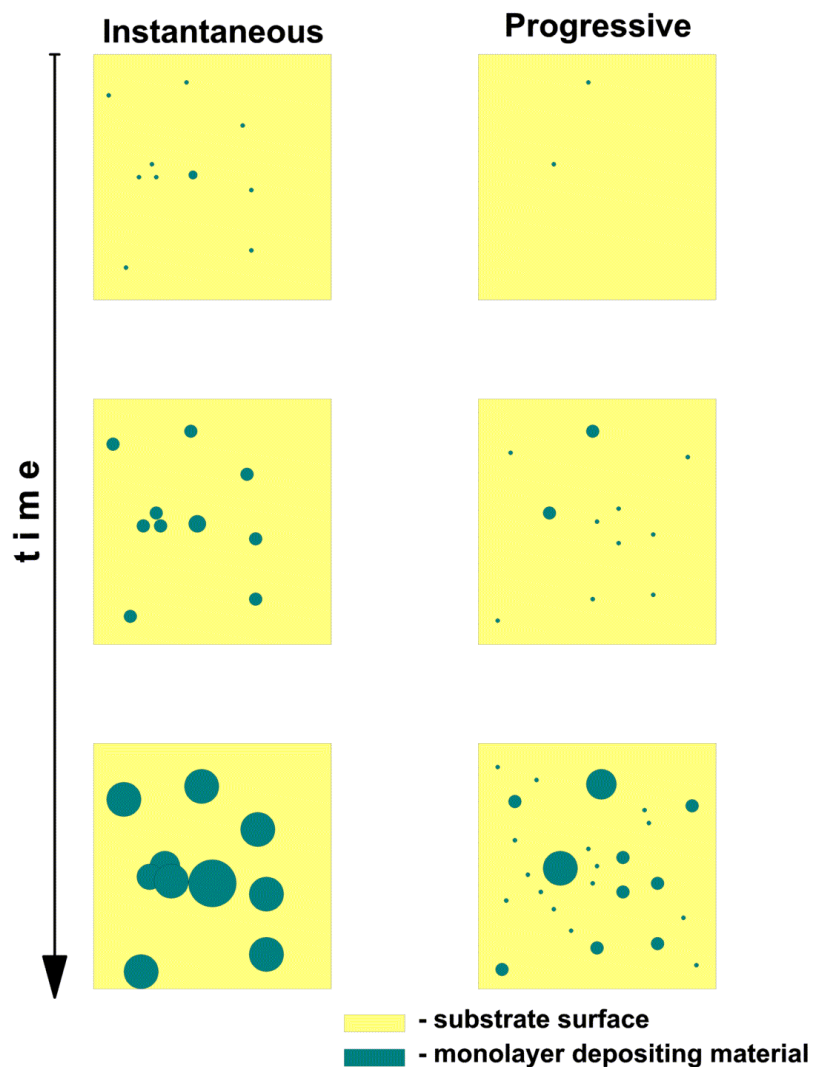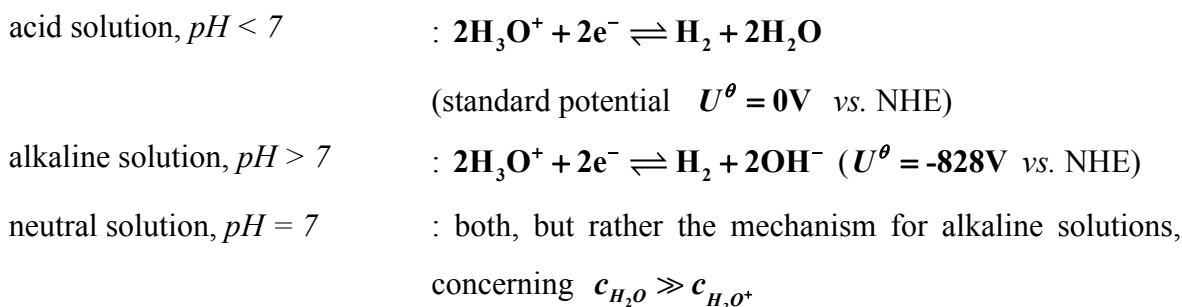

Fig.1.9: Sketch of contrasting progressive and instantaneous nucleation. In the progressive nucleation case (right side), during the growing of the existing nuclei new nuclei arise. In the instantaneous case (left side), all of the nucleation occurs before the first slide and the deposition process is without arising of new nuclei.

1.4 The hydrogen-evolution reaction

The hydrogen evolution reaction (HER) is an electrochemical process that has received a broad attention because of its importance in both fundamental and technological electrochemistry [43]. On one hand, it is one of the standard methods producing hydrogen gas. On the other hand, hydrogen evolution reaction is of fundamental importance in hydrogen-oxygen fuel cells, in corrosion and in electrodeposition. Another important application of the hydrogen evolution reaction is the production of heavy water (D_2O) from a H_2O/D_2O mixture. The principle of the method is that hydrogen (H_2 gas) evolves faster at the electron-source electrode than deuterium (D_2 gas). This leaves a D_2O-enriched solution behind. The operation will depend on the ratio of the electronation currents i_{H_2}/i_{D_2}. The higher is the ratio, the faster is the separation of the isotopes.

Hydrogen evolution reaction runs on a great number of metals. The last fact permits the rate of hydrogen evolution to the studied upon a much larger number of electrocatalysts than any other reaction. Results are available on more than twenty metals and therefore a trend on the reaction rate as a function of the substrate properties can be revealed. In aqueous solutions hydrogen evolution reaction runs in whole *pH* range with the following over all reaction path:

acid solution, *pH < 7*   : $\mathbf{2H_3O^+ + 2e^- \rightleftharpoons H_2 + 2H_2O}$

(standard potential $\mathbf{U^\theta = 0V}$ *vs.* NHE)

alkaline solution, *pH > 7*   : $\mathbf{2H_3O^+ + 2e^- \rightleftharpoons H_2 + 2OH^-}$ ($\mathbf{U^\theta = -828V}$ *vs.* NHE)

neutral solution, *pH = 7*   : both, but rather the mechanism for alkaline solutions,

concerning $c_{H_2O} \gg c_{H_3O^+}$

In the following survey the case of aqueous acid solutions will be the main concern. The hydrogen evolution reaction consists of two steps. The first one is the hydrogen adsorption step onto the metal and the second one is the hydrogen desorption step. The overall reaction can be separated to several partition steps [42, 43]:

1. Mass transport of dissolved hydrogen (H_3O^+ ions) to the surface and physisorption of hydrogen (transfer of the protons through the water chains)

2. Charge transfer: discharge of H_3O^+ and adsorption of hydrogen on the electrode surface; so-called "Volmer"-step:

$$H_3O^+ + e^- \rightarrow H_{ad} + H_2O \qquad (1.14)$$

3. Recombination: evolving of hydrogen gas. The adsorbed hydrogen atoms formed from the discharge step recombine to form hydrogen gas. There are two possible reaction paths:

   a) Chemical-desorption step: Known as "Tafel"- reaction
   $$2H_{ad} \rightarrow H_{2,ad} \qquad (1.15)$$

   b) Electrochemical desorption step: This step is known as "Heyrovsky"-reaction or ion-atom recombination. The protons discharge on top of the adsorbed hydrogen with the simultaneous formation of hydrogen molecules. This step occurs predominantly at higher surface coverage of the adsorbed hydrogen atoms.
   $$H_{ad} + H_3O^+ + e^- \rightarrow H_{2,ad} + H_2O \qquad (1.16)$$

4. Desorption and diffusion of the hydrogen away from the electrode surface

The possible reaction mechanisms of hydrogen evolution are Volmer-Tafel and Volmer-Heyrowsky mechanisms. The first one is known also as "discharge followed by chemical desorption" and the second one as "discharge followed by electrochemical desorption". Each mechanism predominates at different surface coverage of adsorbed hydrogen. At lower coverage the probability of occurrence of Volmer-Heyrowsky mechanism is negligible. On the other hand at higher surface coverage of adsorbed hydrogen the Volmer-Tafel mechanism is insignificant.

In the multistep reactions one step exist, which controls the overall reaction rate. This step is the rate-determining step (rds). The condition of the existence of a single rds is that the

activated state corresponding to the rds is much higher with respect to the initial state for the overall reaction than the activated state matching to any other step. The rate-determining step has the highest standard free energy of the activated state compared with that of the initial state. Let us assume that the activated states of more than one step are within $2 - 4$ **kJ/mol** of the same energy with respect to the initial state. Thus, there will be a multiple control of the rate of the overall reaction. In the case of two steps reactions (her) the activated states are at almost the same energy level with respect to the initial state, the two steps will exercise dual control over the rate of overall reaction (known as *dual mechanism*).

Suppose that the reverse velocities of both partial steps are negligible compared with the forward velocities. Therefore, increase the forward velocity of the first step, and the forward velocity of the second step has to increase to fulfill the steady state hypothesis (concentration of the adsorbed hydrogen constant with time). In such a case (negligible reverse velocities), the forward velocities of the two steps are coupled to each other, and the overall reaction is said to be a *coupled reaction* [43].

Two reaction mechanisms (Volmer-Tafel and Volmer-Heyrowsky) have been suggested for the hydrogen evolution reaction. Both are two steps reactions and each step from these mechanisms can be a rate-determining step. The step other than the rds can be assumed to be in equilibrium if there is no coupled mechanism present. The convention of representing a mechanism is used indicating which step is in equilibrium ($\rightleftharpoons$) and which step is rate determining ($\rightarrow$). Hence, if the discharge step (Volmer) is rate determining, one can write the mechanism in the following way

$$H_3O^+ \xrightarrow{\;\;V\;\;} H_{ad} \underset{\longleftarrow}{\overset{T,H}{\rightleftharpoons}} H_2 \tag{1.17}$$
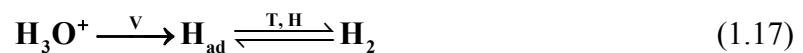
and, if the desorption chemical or electrochemical (Tafel or Heyrowsky) is rate controlling, the mechanism is

$$H_3O^+ \rightleftharpoons^{\;V\;} H_{ad} \xrightarrow{\;\;T,H\;\;} H_2 \tag{1.18}$$

Usually, the slowest reaction step is referred to rds, and the other steps are called fast steps. The terms "slow" and "fast" must be understood in a technical way. In the steady state all steps must proceed at the same net velocity, otherwise, the intermediate concentration would change with time in contradiction to the definition of steady state.

Assume that the rate-determining step is the proton discharge (Volmer-step), thus the formation of adsorbed hydrogen atoms occurs with difficulty and those atoms which do arrive on the surface are wiped away by a fast hydrogen desorption step (Tafel-step). Therefore, the surface concentration of the hydrogen atoms will be very low.

In the other case, if the desorption step is slow, i.e., the rds, then the formation of adsorbed hydrogen atoms will be faster compared to their recombination on the surface. The hydrogen atoms will begin to accumulate on the surface due to the fact that the hydrogen recombination is too slow to wipe them away. Desorption step increases with increasing of the surface coverage of hydrogen. It needs a large fraction of surface coverage before it can encourage the desorption-step to take place at a rate equal to the rate of proton-discharge step. Thus, the surface coverage of adsorbed hydrogen atoms will be relatively high in order to reach steady state.

The determination of a reaction mechanism requires a number of observations. The first one is the measurement of the exchange current density, which gives a general idea of the reaction rate in the standard state of equilibrium. Thus, it is possible to qualify the electrode as a good or bad electrocatalyst for hydrogen evolution reaction. The noble metals have values of exchange current densities for hydrogen evolution in the range of milliamperes.

Because of two electrons transfer in hydrogen evolution reaction the general form of the Butler-Volmer equation for multistep reactions should be applied [43]. The general form of the Butler-Volmer equation is valid for multistep overall electrodic reaction in which there may be electron transfers in steps other than the rate determining step (rds) and in which the rds may have to occur υ times per occurrence of the overall reaction.

$$ j = j_0 \left\{ \frac{\theta_H}{\theta_{H,0}} \exp\left[\frac{\alpha_{eff,a} F}{RT} \eta \right] - \frac{1-\theta_H}{1-\theta_{H,0}} \exp\left[-\frac{\alpha_{eff,c} F}{RT} \eta \right] \right\} \tag{1.19} $$

$$ \alpha_{eff,a} = \left(\frac{n-\gamma}{\upsilon} - r(1-\alpha_a) \right) \tag{1.20} $$

$$ \alpha_{eff,c} = \left(\frac{\gamma}{\upsilon} + r\alpha_c \right) \tag{1.21} $$

$$ \alpha_{eff,a} + \alpha_{eff,c} = \frac{n}{\upsilon} \tag{1.22} $$

n :   The total number of electrons transferred in overall reaction

γ :   Electrons transferred in the steps preceding the rate-determining step (rds)

υ :   Number of rds repetitions per single cycle of the overall reaction

r :   Number of the electrons involved in rds

θ_H :   Surface-coverage, $\theta_H = \frac{\text{blocked adsorption sites}}{\text{total number of the adsorption sites}}$, $\theta_H = \theta_H(\eta)$

$\theta_{H,0}$:   Steady state surface coverage for $\eta = 0$, also in j_0 included

α_c, α_a :   Cathodic and anodic transfer coefficients

$\alpha_{eff,c}$:   Effective cathodic transfer coefficient

$\alpha_{eff,a}$:   Effective anodic transfer coefficient

In the equation it is assumed that in every partial step, except the rate determining step, only one electron is transferred. Only steps with charge transfer are considered.

The second important parameter in the determination of the reaction mechanism is the transfer coefficient. The experimental transfer coefficients can be determined in a simple way. A series of applied current densities are used, and a η versus $\log j$ plot (Tafel plot) is drawn. The slope of such a plot at a constant concentration of reactants, gives the transfer coefficient thought the following equation [43]:

$$\frac{dU}{d \log j} = \frac{2.303 RT}{\alpha_{eff,c} F} = \frac{1}{\alpha_{eff,c}} 59.14 \frac{mV}{Decade} \tag{1.23}$$

The Table.1 exhibit some calculated transfer coefficients and Tafel slopes received from equation (1.23) assuming for $\alpha_c = 0.5$ and $T = 298K$. On the basis of the transfer coefficient evaluations, a distinction between different reaction mechanisms cannot be made. It is clear that the same transfer coefficient exists for different reactions. Nevertheless, it is helpful to know the value of the transfer coefficient because it permits to eliminate some reaction mechanistic possibilities and thus narrows down the number of reaction paths, which have to be considered.

Table.1: Dependence of the effective cathodic transfer coefficient $\alpha_{eff,c}$ on the surface coverage and rds (rate determining step). The indices $_{rds}$ are used in the case of rate determining step.

No.	θ_H	MECHANISM	$\alpha_{eff,c}$	Tafel - slope $\frac{mV}{decade}$	Reference
1.	No limitation	Volmer$_{rds}$ + Tafel	0.5	118	[43, 45]
2.	$\theta_H \to 0$	Volmer + Tafel$_{rds}$	2.0	29	[43, 45]
3.	$\theta_H \to 0$	Volmer$_{rds}$ + Heyrowsky	0.5	118	[43, 45]
4.	$\theta_H \to 0$	Volmer + Heyrowsky$_{rds}$	1.5	39	[43, 45]
5.	No limitation	Volmer + Tafel coupled	0.5	118	[43, 45]
6.	No limitation	Volmer + Heyrowsky coupled	0.5	118	[43, 45]
7.	$\theta_H \to 1$	Volmer + Tafel$_{rds}$	0	∞	[46]
8.	$\theta_H \to 1$	Volmer$_{rds}$ + Heyrowsky	1.5	39	[43]
9.	$\theta_H \to 1$	Volmer + Heyrowsky$_{rds}$	0.5	118	[46]

Chapter 2

Experimental set-up

The experiments, described in this thesis, were performed mainly with a Scanning Tunneling Microscope and a general description of the set-up is presented. In the first part the electrochemical STM set-up and the preparation of the STM tips are explained. In the second part the electrochemical set-up for the reactivity measurements and the substrate treatment technique are discussed. Also the experimental procedure and the fabrication of the STM-tip pH sensor are clarified.

2.1 Electrochemical Scanning Tunneling Microscope

The main set-up of a electrochemical scanning tunneling microscope consists of: a scanning tunneling microscope, a bipotentiostat and a electrochemical STM-cell (Fig.2.1). For the measurements a commercial electro-chemical scanning tunneling microscope (EC-STM) equipment of the company Molecular Imaging from the type PicoSPM$^{®}$ was used. The device is based on the following built-up principle. The piezo drive unit is combined for all three dimensions in a cylindrical piezo. The cylindrical piezo and a preamplifier, which serves for the current/voltage conversion and amplification of the tunneling current, are placed in a compact metal housing. This functional unit is generally called "scanner". The scanner is assembled in a second housing, which is called STM-head. The

ferromagnetic sample holder with the miniature electro-chemical cell is attached to the STM-head with three magnetic micrometer screws. Two of the screws serve for the rough approximation of the STM tip to the sample and are manually adjustable. The third screw is for the fine adjustment of the tip controlled by a stepper motor. The automatic feedback control parameters are selected in such a way that during the adjustment of the tip (by the stepper motor) to the sample, the piezo in z-direction is maximally retracted. One step of the stepping motors corresponds to a reduction of the distance between the tip and sample by a defined distance. After each step the piezo extends in z-directions and the presence of the tunneling current is checked. The maximal extension of the piezo is larger than the achieved reduction of the distance between the tip and the substrate after one motor step.
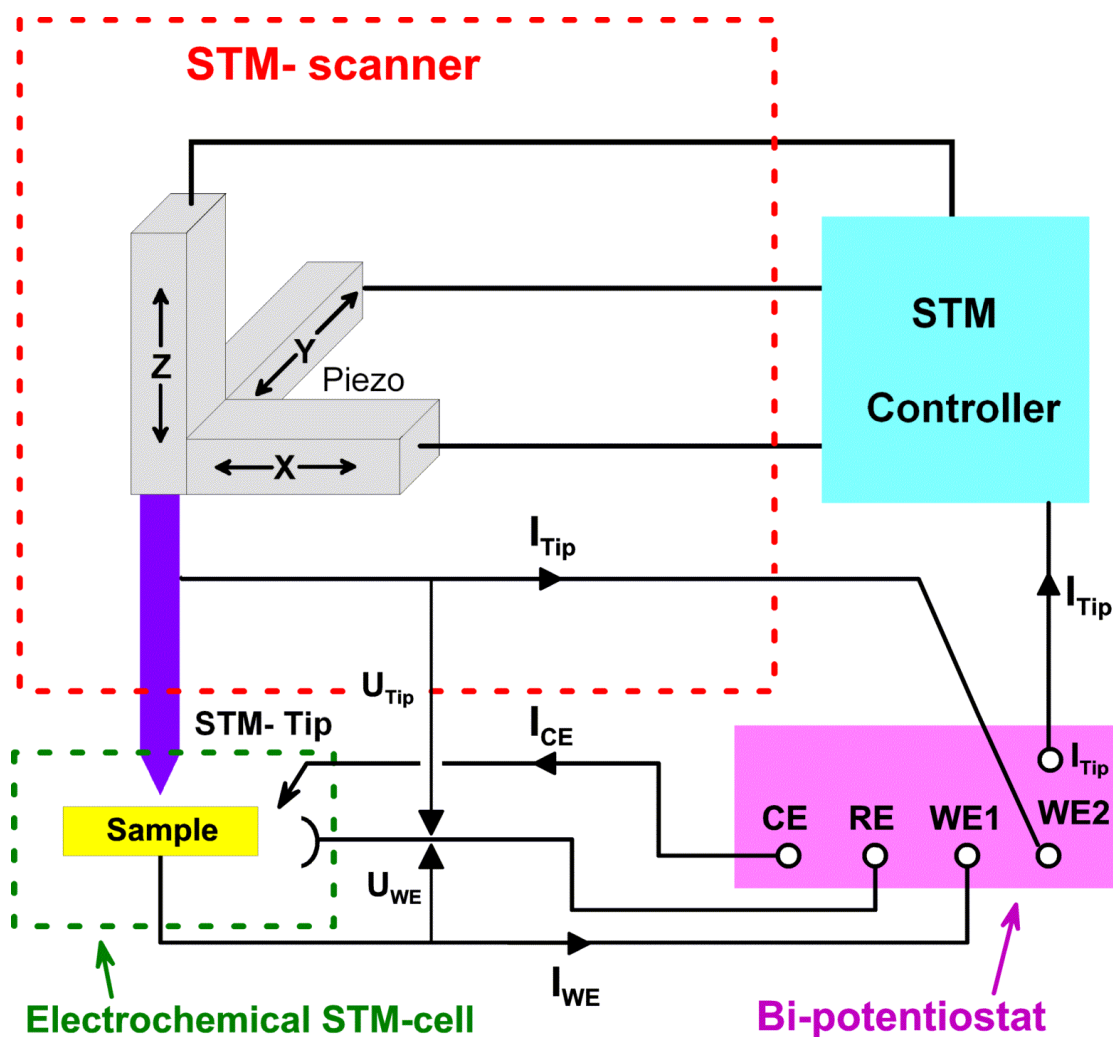

Fig.2.1: Schematic representation of the electrochemical scanning tunneling microscope set-up.

Thus, if the tunneling current was detected, the approach stopped. Otherwise, if the tunneling current was absent, the piezo retracted and the next step of stepping motor was done and so on until the tunneling condition was established.

This procedure allows the piezo to pull back the STM-tip as fast as possible, when the tunneling current is registered, in order to prevent physical contact between the sample and the STM-tip. The miniature electro-chemical cell is fabricated from a Teflon$^{\circledR}$ ring (Fig.2.2). The latter has two different diameters at both ends. The end of the ring, which contacts with the sample, is with 4 mm diameter. The other end is with 8 mm diameter in order to serve enough volume for the counter and the reference electrodes. Therefore, the working electrode area, which contacts with the electrolyte was minimized. A gold wire was used as counter electrode. The shape of the wire was spiral in order to increase the electrode surface. These measures were necessary for the potential pulse experiments, since conventional EC-STM cells exhibited an unfavorable geometry, which leads to potential fluctuations at the STM-tip. An oxidized gold wire was used as reference electrode. It was oxidized in 0.1 M $HClO_4$ at 5 V *vs*. RHE for 2 minutes. In order to reach a stable potential the electrode was left for 30 min at open cell potential for "relaxation". The stabilized reference electrode potential was 1220±10mV *vs*. RHE and it was reliable for at least 6 hours. The scanning unit and the STM electro-chemical cell were in a cylindrical glass chamber to be able to work in inert gas atmosphere.
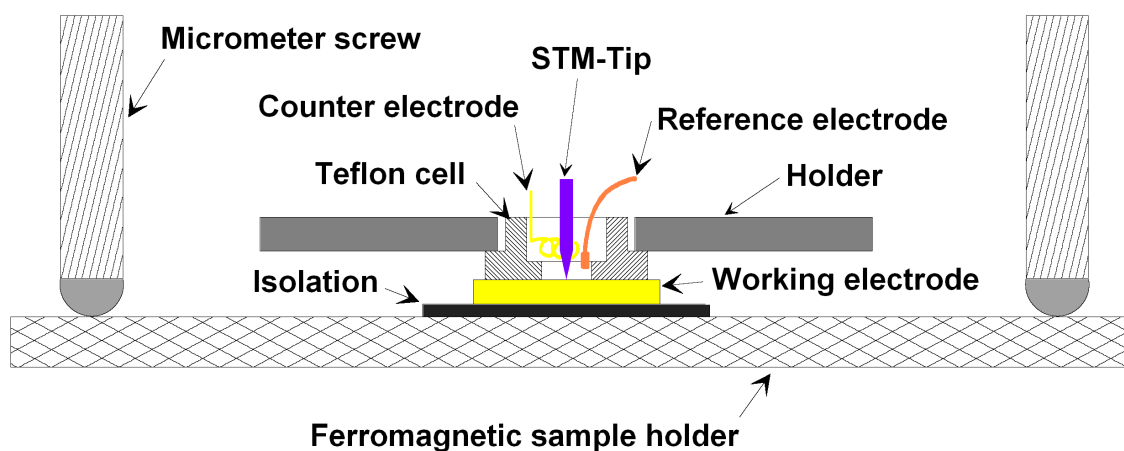

Fig.2.2: Schematic representation of the electrochemical STM-cell [47].

The used bipotentiostat BP-600 (EC-Tec GmbH, Teutschenthal, Germany) has two connectors for the reference and the counter electrode and two for the working electrodes (STM-tip and sample), respectively. Furthermore, the working electrode potentials, the bandwidths and the current ranges are manually adjusted. Two additional inputs for each working electrode were able to permit modulation of the electrode potentials independently with a 3dB-bandwidth > 1 MHz. In contrast to the commercial EC-STM units, the conventional electro-chemical measuring procedures in the STM-cell can be performed. The electrode potentials and the currents of both working electrodes were available to be monitored alternatively from galvanically isolated and non-insulated outputs. The tunneling current passed from the bipotentiostat galvanically isolated to the STM controller, which regulates the tip movement in x, y, z-direction. Furthermore, the controller was used also for the storage and for the processing of the topographic information from the STM measurements (Fig2.1).

2.2 Preparation of the STM-tip

The shape of the scanning tunneling microscope tip is extremely important for the quality of the recorded images. Good lateral resolution is only achieved by a tip radius as small as possible. When the tip is used in electrolyte, the Faraday's current at the top of the tip should be lower than the tunneling current. In such case the STM tip should be well isolated. The preparation of the tip includes two steps, which are described in the next section.

2.2.1 Electrochemical tip etching

The STM-tip is produced by electro-chemical etching in alkaline cyanide solution, which consists of 5M KCN in 3M NaOH. Platinum/Iridium (90/10) wire of 0.25 mm is used for the tip preparation. The wire was cut into pieces of approximately 30 mm length and cleaned by annealing prior to etching.
Fig.2.3 shows the set-up for STM tip preparation. The piece of wire was passed through an 8 mm diameter ring of Pt wire (0.25 mm diameter) as a counter electrode. It was important to position the Pt/Ir wire in the center of the Pt ring; otherwise the future tip would have an

asymmetrical form at the apex. Then the lamella of alkaline cyanide solution was created on the Pt ring [48]. An alternating voltage of 1 kHz and 10 V was applied between the ring and the wire. The entire etching procedure takes approximately 15 minutes and every two minutes the liquid lamella was renewed. At the end of the etching procedure 2 V was applied between the electrodes in order to improve the quality of the tip. The wire immersed into the solution of KCN was etched until its bottom part fell down and the alternating voltage was immediately switched off. The etching was stopped and both parts – upper and lower – could be used for a STM experiment. The tips were rinsed carefully with hot ultra-pure water (18,2 MΩcm und 3 ppb TOC, produced with Milli–Q gradient A10, company Millipore). The freshly prepared clean and dried tips were used for the next step of tip preparation – the tip insulation.

The above mention procedure provides a guarantee of the quality of the measurements; good geometry tips and demonstrates the competence to manufacture same micrometer scale tips. During the tunneling process only the forefront atoms are important. Moreover only part (around 60 %) of all prepared tips for the STM were suitable i.e. the obtained quality of images was enough good to differentiate between monoatomically high terraces of a single-crystal sample.
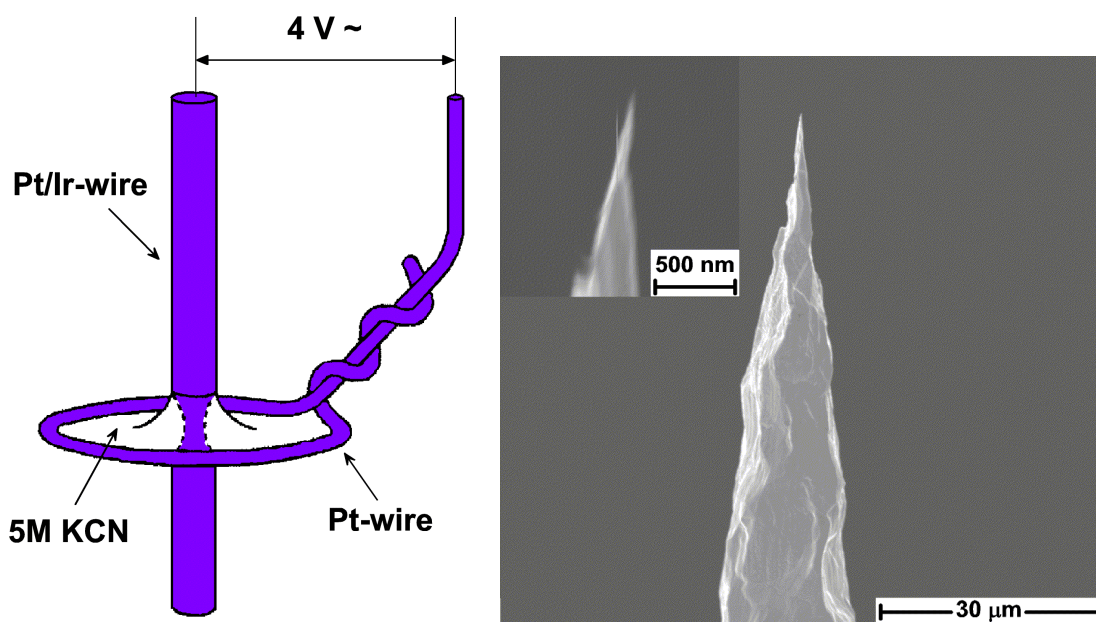

Fig.2.3: Electrochemically STM-tip etching (a) the set-up [47], (b) SEM image of electro-chemically etched Pt/Ir STM tip.

2.2.2 Tip Insulation

In a electrochemical environment the STM-tip has to be insulated in order to reduce the Faraday's current to be negligible compared to the tunneling current. Thus, the feed back control of the STM can work properly. The tips were insulated with an anodic dipping paint (ZQ843211, BASF) using a procedure developed by Bach et. al. [49]. A platinum wire in helical shape is used as a counter electrode and placed around the tip in distance of about 4 mm. The dipping paint was deposed on the STM-tip by applying current of 100 μA for 30 sec between the tip and the counter electrode.

After the deposition the tip is removed from the dipping paint and immediately put in a preheated furnace at 190 °C for 30 minutes. The dipping paint contains polyacrylcarboxyl acid, which hardens and constrict after baking, thereby leaving the tip apex uncovered.

2.3 Electrochemical set-up

Palladium deposition of Pd monolayers on Au(111) and the reactivity measurements were performed in a separate experimental set-up. It included a classical two-compartment electrochemical three-electrode glass cell, a Potentiostat PG300 (HEKA Elektronik Dr. Schulze GmbH) and a computer with the data acquisition software PotPulse v 8.54 (HEKA Elektronik Dr. Schulze GmbH). The sampling rate of the potentiostat was 200 MHz with 16 000 maximum dada-points. The deposition and the reactivity measurements were performed in separate cells in order to avoid Pd contaminations. The classical two-compartment electrochemical three-electrode glass cell consists of a working electrode, a counter electrode and a reference electrode (Fig.2.4). The reference electrode was attached in the first compartment. The working and the counter electrodes were included in the second compartment. Both compartments are connected with a small glass tube, so-called "Luggin capillary". The latter ends at about 1 cm from the working electrode in order to reduce as much as possible the potential drop in the electrolyte between the working and the reference electrodes. The headspace of the cell and the electrolyte can be purged with inert gas in order to remove the oxygen from the electrolyte. A glass tube was used as a gas inlet. The gas outlet passed trough a small glass reservoir filled with water, in order to
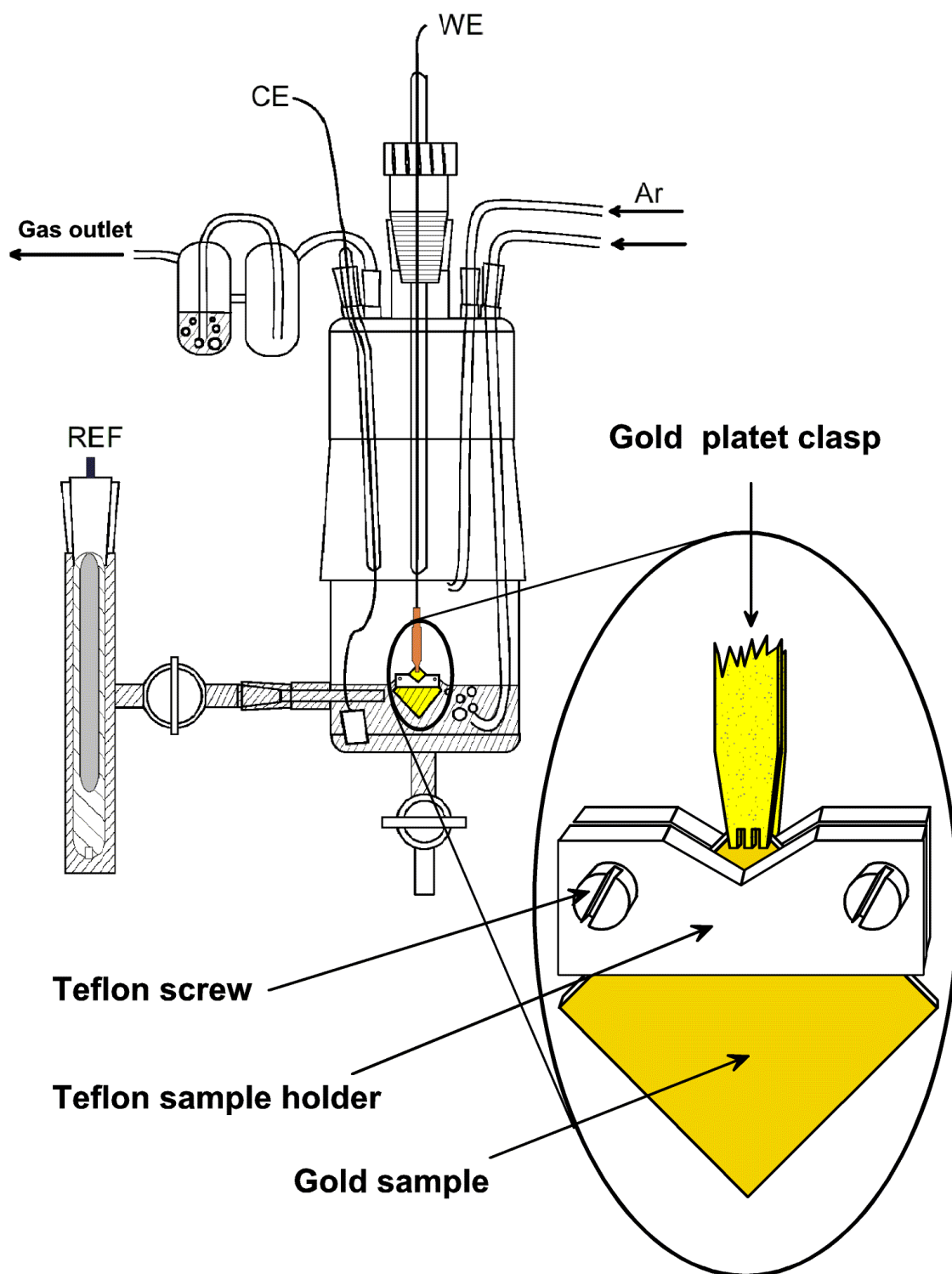
Fig.2.4: Construction of the electrochemical cell [47]. WE: working electrode; CE – counter electrode; RE – reference electrode.

prevent the diffusion of air back into the cell. The reference electrode connection to the potentiostat passed through a voltage-follower with higher input impedance. In such a way during the measurements the current through the reference electrode was minimized. The gold sample was attached to the connectors by gold plated peg ("crocodile"). A Teflon$^{®}$ holder was used to fix the sample area, which was in a contact with the solution.

2.3.1 Cleaning of the electrochemical cells

The glass parts of the electrochemical cells were cleaned separately. First they were cooked in a five-liter glass beaker filled with concentrated sulfuric acid (95-97 % Sulfuric Acid for Analysis, Merck Eurolab GmbH). Thus, the organic contaminations were dissolved and removed. Afterwards, the parts were cooked between 8 and 12 times with ultrapure water until all ions were removed (Milli-Q Gradient A10, Company Millipore, 18.2 MΩcm, TOC = 3 ppb). The Teflon$^{®}$, gold and platinum parts were cleaned in so-called " Piranha water" (H_2O_2: H_2SO_4) and then cooked also in ultrapure water. After the cleaning procedure and prior cell assembling, the gold parts were flame annealed. In this way the gold oxide formed in the previous experiments were reduced.

2.3.2 Preparation of the electrolytes

The solutions were prepared from HClO$_4$ (Merck, Suprapur), and Pd(NO$_3$)$_2$ (MaTecK) with Millipore-MilliQ water (18.2 MΩ cm, 3 ppb total organic carbon). They were kept in a refrigerator at lower positive temperatures (°C) in order to be stable longer time. The solutions were renewed periodically and the glass containers were cooked with ultrapure water prophylactically. The cleanness of the HClO$_4$ solution and the electrochemical cells were proved with the CVs of Au(111) or Pt wire, which are well known from the literature [50-53].

2.4 Preparation and characterization of the substrates

All used substrates (working electrodes) were made of evaporated gold films on tempax glass (Metallhandel Schroer GmbH). The film structure of the substrates was as follows: 250 nm gold, 2.5 nm chromium layer and 1.1 mm borosilicate glass with a 11x11 mm square size. The gold film exhibits a polycrystalline structure. Therefore, the substrate was flame annealed in order to achieve a film of crystallites with atomic flat terraces. The flame annealing procedure was as follows: the sample was placed on a ceramic plate and heated slowly and homogeneously with butane/air flame until it became reddish and then the temperature was kept for about 2 minutes constant. Subsequently the substrate was cooled to ambient temperature in a nitrogen stream to protect the annealed surface from contaminations coming from air. Thus, the higher temperature increased the mobility of the surface gold atoms and they achieved the thermodynamically favorable order represented in large (111) oriented terraces. The images of such substrates after flame annealing are shown in Fig.2.5. The size of the crystallites varied from several 100 nm to 2 μm. The single crystallites consisted of monoatomic flat terraces separated from monoatomic high steps. The last one formed 60° angle, which characterize the Au(111)-surface (face centered cubic).

The Au(111) substrate is inert in a wide potential range – approximately from 0 V up to about 1.1 V, where the gold oxide formation starts [50, 51]. The gold double layer potential range coincides with the Pd oxide formation and reduction potential regions. Thus, the characteristics of the deposited sub-monolayers Pd can be investigated without influence of the gold substrate. Fig.2.6a shows the cyclic voltammogram of the evaporated gold substrate after flame annealing in 0.1 M $HClO_4$. The potential was scanned between – 0.15 and 1.6 V from 0.5 V initially in the positive direction by 50 mV/s. Two anodic peaks corresponding to the gold oxide formation were observed at 1.28 V and 1.48 V, respectively [50-53]. In the negative-going sweep the cathodic peak arises due to the reduction of the formed, in the positive-going sweep, gold oxide [52, 53]. The image in Fig.2.6b shows the surface during the potential sweep from 1.6 V to 0.5 V. At 1.6 V the surface was covered with oxide layer represented as a rough grain structure. Subsequently, after scanning of the potential down to 0.5 V the gold oxide was reduced and the surface

was covered with monoatomically deep pits. These pits were formed due to the place exchange processes during the gold oxide formation.

a

b

4 μm x 4 μm   150 nm x 150 nm
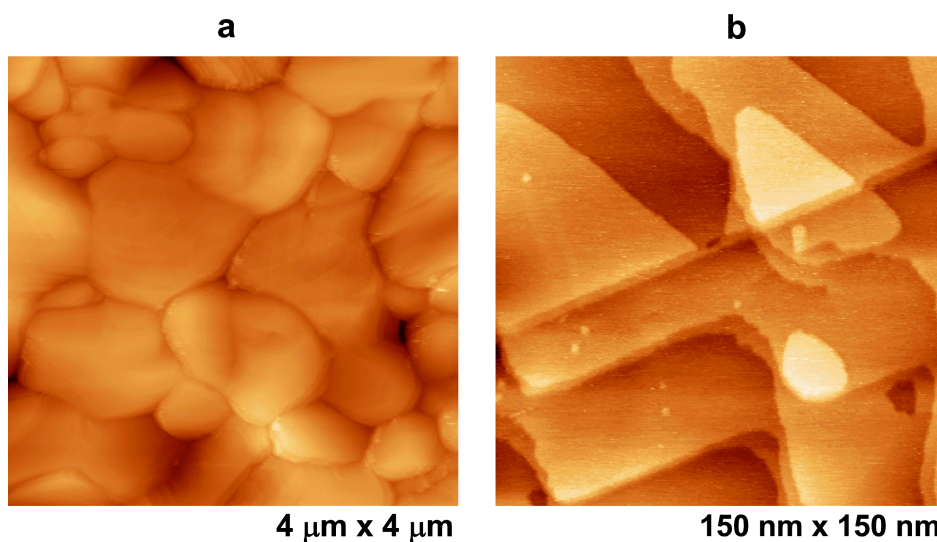
Fig.2.5: EC-STM images of evaporated gold films in 0.1 M HClO$_4$, U$_{WE}$ = 600 mV *vs.* RHE, I$_{Tun.}$ = 1 nA, U$_{Tun}$ = 100 mV. (a) size = 4 μm x 4 μm , (b) size = 150 μm x 150 μm.

a

b
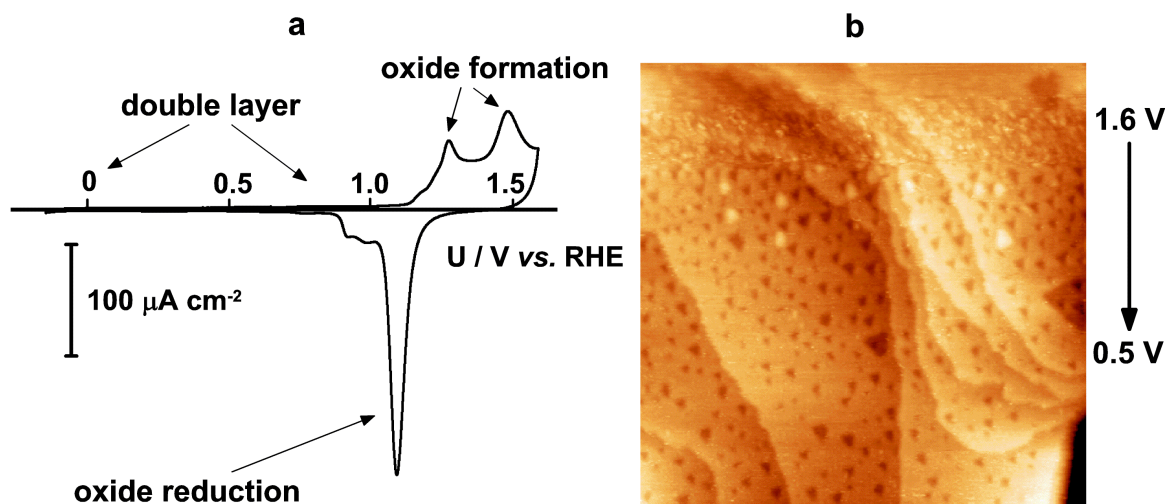
Fig.2.6: (a) Cyclic voltammogram of freshly flame annealed evaporated gold film in 0.1 M HClO$_4$. Sweep rate 50 mV/s. (b) corresponding in situ EC-STM-image of the surface during potential sweep from 1.6 V down to 0.5 V, I$_{Tun}$ = 0.8 nA, U$_{Tun}$ = 100 mV, size 100 x 100 nm.

2.5 Experimental procedure

2.5.1 STM measurements

First the STM cell was filled with Pd free 0.1 M $HClO_4$ solution, and the potential was adjusted at 0.84 V in the double layer region, where no Pd deposition took place. Subsequently, defined a quantity of $Pd(NO_3)_2$ concentrated solution was added to obtain 0.5 mM $Pd(NO_3)_2$ concentration in the STM-cell. The last procedure was used in order to exclude undefined potentials by connecting the electrochemical STM cell with the potentiostat. In the case of a Pd containing solution an undefined potential could lead to uncontrolled Pd deposition. Prior to the measurements the gas chamber, where the STM electro-chemical cell was placed, was purged with nitrogen for at least 20 min. When the tunneling conditions were reached, the place of interest was found. First, a maximum surface area (1x1μm) was scanned. Afterwards, the place of interest was observed at different potentials and the Pd nucleation process on Au(111) was investigated.

In case of potential pulse deposition, the cell chamber was purged in all experiments exactly for one hour with the same gas flow in order to achieve equal concentration of the oxygen. Before the potential pulse was applied, the surface was proved with STM images for Pd deposits. Subsequently, the STM tip was withdrawn 30 μm away from the surface in order to avoid its influence during the deposition process. After the pulse was applied the surface was imaged. The imaged place was chosen in such way that the whole image consists of only one Au(111) terrace with Pd islands. That is important for the image evaluation procedure.

2.5.2 Electrochemical measurements

Prior to the measurements the electrochemical cell was purged with nitrogen for at least 20 minutes. The cleanness and the oxygen containing was proven with CVs of Au(111) in the used Pd free solution of 0.1 M $HClO_4$.

The samples with Pd sub-monolayers deposited in the STM cell were rinsed with ultrapure water to avoid further Pd deposition after being transferred into the Pd-free solution. The used initial potential was 0.5 V, which results in no reaction at the Pd nano-islands and at the Au(111) surface. First the samples were characterized with cyclic voltammograms and

the deposited amount of Pd was controlled for additional deposition. The reactivity measurements were performed, subsequently.

The immersion of the sample in the Pd containing solution was performed under potential control in order to avoid undefined deposition. The used initial potential was chosen in the potential range from 0.85 V up to 1.05 V where no Pd deposition or Au(111) oxidation occurred.

2.6 Preparation of a pH sensor

2.6.1 The phenomena

The ability of palladium hydride to serve as a pH-electrode can be understood through the palladium/hydrogen phase diagram (Fig.2.7). At room temperature, the palladium-hydrogen phase diagram consists of a low hydrogen-containing α - phase, an intermediate miscibility gap consisting of two phases: α - and β - phase coexist over the H/Pd atomic ratio range of 0.02-0.6, and a high hydrogen-containing β - phase [54, 55]. Inside of the α - phase, the activity (or chemical potential) of hydrogen varies depending on the amount of hydrogen in the α - phase. When the hydrogen content is increased to the edge of the miscibility gap, the system has only one degree of freedom (temperature), which fixes the
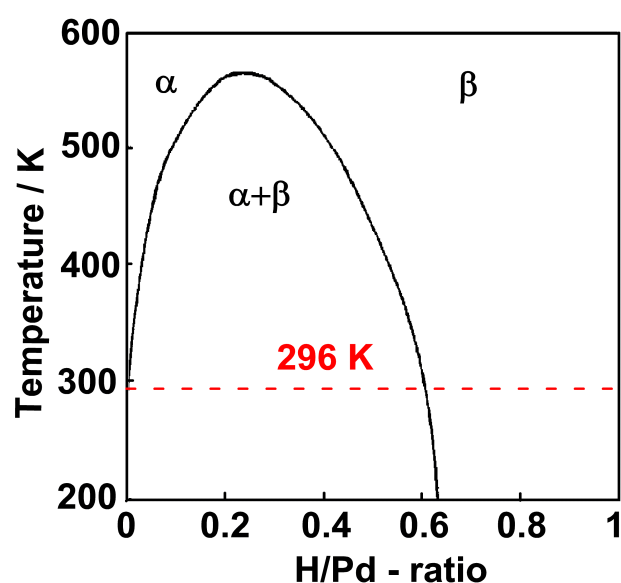

Fig.2.7: Phase diagram of Pd/H showing the miscibility gap $\alpha + \beta$ [54, 55].

hydrogen content and therefore the hydrogen activity of the α - phase. In the two-phase region, equilibrium dictates that the activity of hydrogen in the α - phase must be equal to the activity of hydrogen in the β - phase. Thus, the activity of hydrogen remains constant within this two-phase region of hydrogen content (at a constant temperature). This constant hydrogen activity in the metal provides a wide-range and stable hydrogen activity against the hydrogen ion activity in solution can be reliably measured. Therefore, the potential remains constant over the entire two-phase $(\alpha + \beta)$ region, and is a function of composition in the pure α - and β - regions. For a gaseous hydrogen fugacity of unity (analogous to a pressure of 1 atm), the pH response can be calculated from the Nernst equation and for partial pressure of hydrogen, p_{H_2}, equal to 1 atm [54]:

$$U = U^\theta - 2.3 \frac{RT}{nF} pH \qquad\qquad (2.1)$$

where U is the potential of the electrode, U^θ is the standard potential of the electrode, T is the temperature, R is the gas constant, n is the number of electrons in the reaction, and F is the Faraday constant.

The primary advantage of a palladium/hydrogen electrode is the same pH response comparable to a palladium/hydrogen electrode with the advantage that it can be used in solutions free of gaseous hydrogen [56]. Palladium provides its own source of molecular hydrogen adsorbed in monatomic form up to 900 times of its own volume at room temperature and pressure [57].

2.6.2 The pH micro - sensor

The pH-response of the Pd/H electrode was investigated with a Pd disk microelectrode with 25 μm diameter. The electrode was prepared from a Pd wire ($\varnothing = 25$μm, 99.9 %, MaTecK GmbH) sealed in a glass capillary, which was melted with butane burner. After sealing, the electrode was finely polished in order to achieve a flat surface. Fig.2.8 shows a schematic picture of the used electrode. The cleaning procedure of the electrode was as follows: first the electrode was cleaned with methanol and after that cooked in ultrapure water several times. Further cleaning, after immersing the sample into the solution, was performed with hydrogen evolution reaction. The cleanness was checked with the stability

of the recorded cyclic voltammograms. Fig.2.9 shows the first two cyclic voltammograms of the Pd microelectrode in 0.01 M H_2SO_4 + 1 M Na_2SO_4 solution. The potential scans were executed with 50 mV/s. The observed peaks are the same as for Pd polycrystalline electrodes with larger electro-active electrode area [58]. The reduced height of the oxidation - reduction peaks (couple) is probably be due to the increased electro-active area during the place exchange processes. After characterizing the surface with the CVs, the Pd microelectrode was enriched with hydrogen in order to achieve $\alpha + \beta$ Pd/H phase composition. The hydrogen enrichment procedure consists of hydrogen evolution reaction at the Pd electrode. One part of the produced hydrogen at the electrode surface diffuses in the bulk of the metal. The rest of the molecular hydrogen forms bubbles and leaves the surface. The loading parameters were following: duration time 20 minutes and applied current density to the electrode 100 $\mu A/cm^2$. After 20 minutes loading with hydrogen the electrode was left at open cell potential for another 10 minutes in order to stabilize the potential. It remains stable for at least 10 hours. The measured open cell potential (OCP) in 0.1 M H_2SO_4 + 1 M Na_2SO_4 solution was − 10 mV. Fig.2.10 shows the OCP of the Pd/H microelectrode as a function of the proton concentration. The quantity of 1 M Na_2SO_4 was added to the solution to keep the ionic strength near a constant value during the stepwise
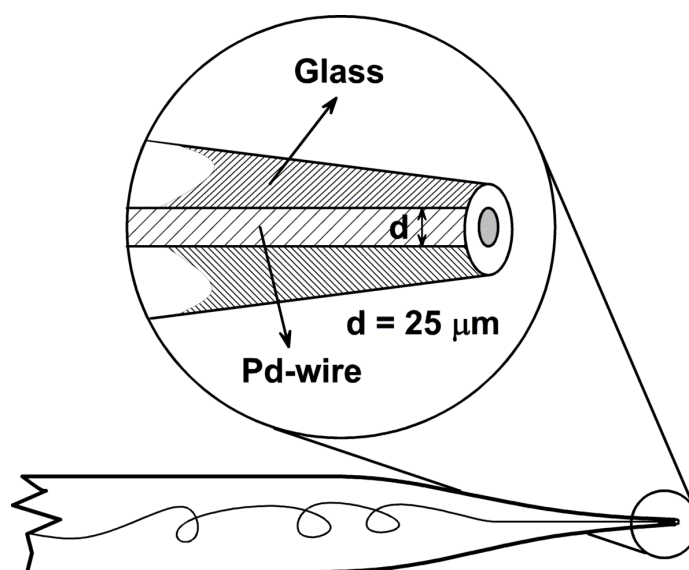
Fig.2.8: Schematic picture of the pH micro sensor. The Pd wire with 25μm diameter is sealed in glass capillary.

incensement of the H_2SO_4 concentration. The enhancement of the proton concentration causes an incensement of the open cell potential. This fact is in good agreement with the literature [54-56, 58-66]. One-decade increase of the proton concentration induces about 60 mV rise of the potential. The last fact can be explained by the Nernst equation (eq.2.1). The performed experiments show that the Pd microelectrode loaded with hydrogen can act as a pH-sensor with a 60mV/pH response.

Pd-poly $\phi = 25\mu m$ **0.01M H$_2$SO$_4$ + 1M Na$_2$SO$_4$, 50 mV/s**
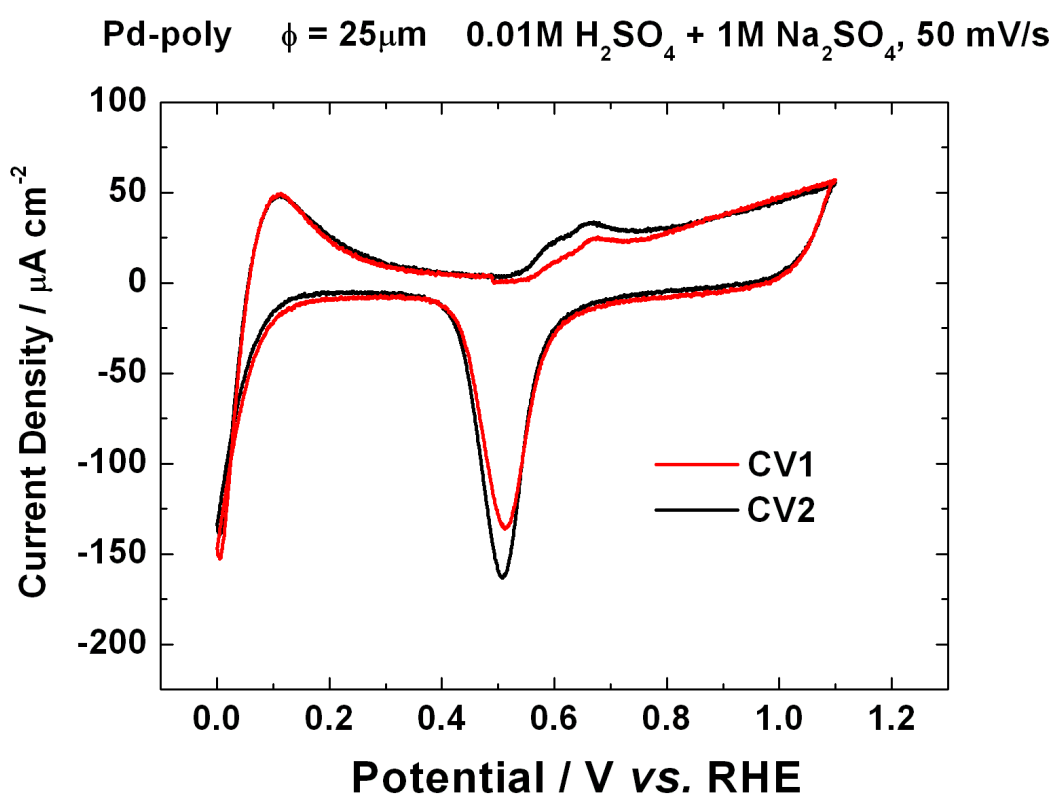
Fig.2.9: The first two cyclic voltammograms of Pd polycrystalline microelectrode ($\varnothing$ 25 μm) in 0.01 M H_2SO_4 + 1 M Na_2SO_4. The sweep rate 50 mV/s. The current density is calculated according to the geometrical electrode area.
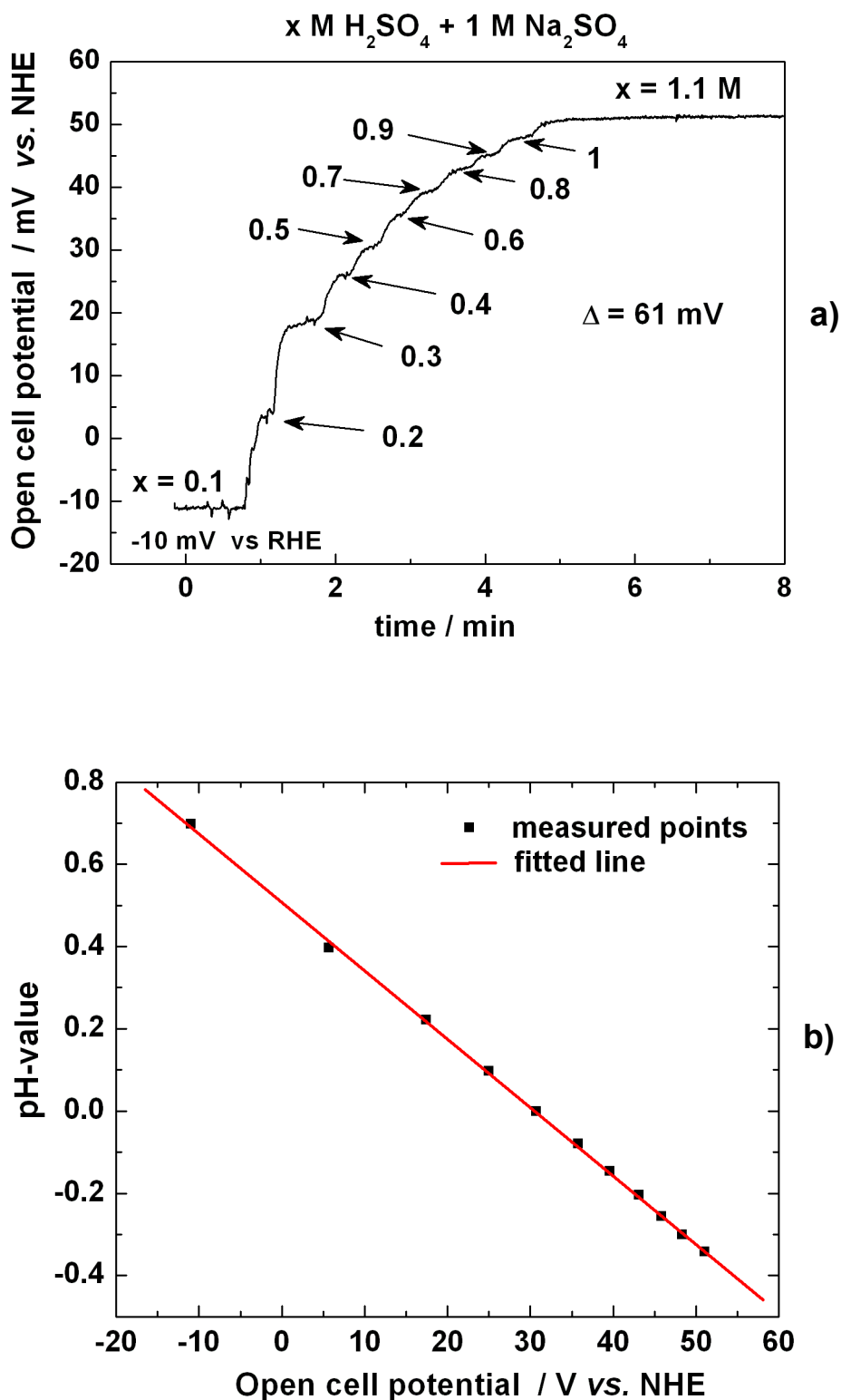
Fig.2.10: (a) Open cell potential as a function of the time during changes of the proton concentration. The used solution was x M H_2SO_4 + 1 M Na_2SO_4, where x = 0.1; 0.2; 0.3; 0.4; 0.5; 0.6; 0.7; 0.8; 0.9; 1; 1.1. (b) Open cell potential as a function of the pH-value.

2.6.3 Palladium STM-tip as pH sensor

As was shown in the previous section the Pd microelectrode acts as a pH-sensor. In this section the same experiment was repeated with Pd STM-tip. The Pd-tip was etched in the same way as the Pt/Ir tip, but with a different solution. The used solution was 30 % hydrochloric acid (Merk, Suprapur). After etching and before insulation, the tip was cleaned in hot ultrapure water for several times. The characterization of the STM-tips were performed with CVs. Fig.2.11 shows the cyclic voltammograms before and after hydrogen loading in 0.1 M H_2SO_4 + 1 M Na_2SO_4 solution at 50 mV/s. The current in the second CV is 60 % higher compared to the first CV. The reason is the enlargement of the non-insulated part of the STM-tip due to the hydrogen evolution reaction. Due to this fact, the loading of the STM-tip with hydrogen should be realized by a current as low as possible. Thus, the loading time increases to an enormously long value. By the use of a stable tip insulation, which is resistant to the higher hydrogen evolution, the loading current can be increased. Fig.2.12 shows the open cell potential of a hydrogen loaded Pd STM-tip as a function of time. The black and the red curves represent the OCP time dependence after hydrogen loading for 20 and 40 min, respectively. Considering the above mentioned
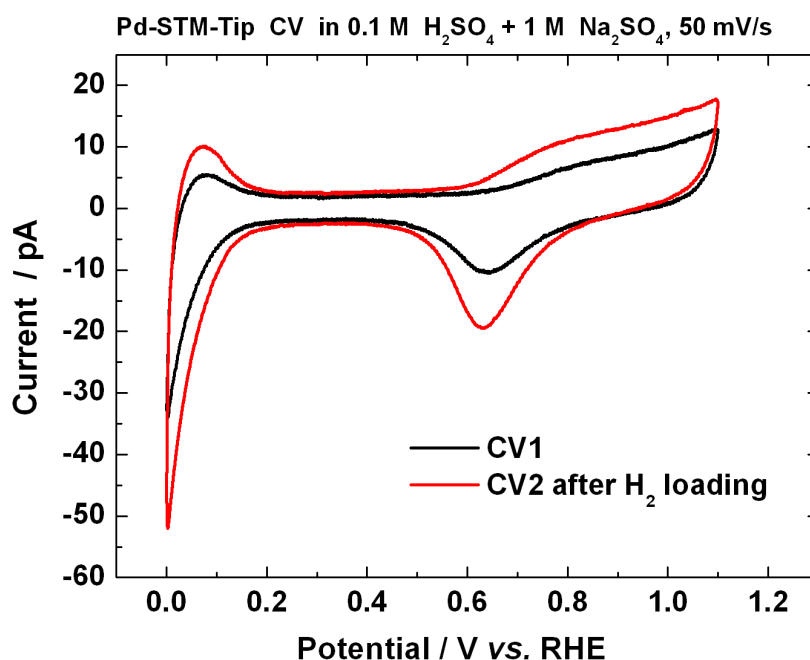
Fig.2.11: Cyclic voltammograms of Pd STM-tip in 0.1 M H_2SO_4 + 1 M Na_2SO_4. Sweep rate 50 mV/s. The black and the red curve represent the CV before and after hydrogen loading, respectively.

conclusions, the chosen loading current was 14 nA. Immediately after hydrogen loading the open cell was stabilized at 15 mV for a defined time. Afterwards the OCP arises continuously to more positive potential values. In the case of 20 min hydrogen loading time the OCP was stabilized for a period of about 3 min and in case of 40 min loading time the OCP was stabilized for a period of about 6 min. The last fact can be explained with the quantity of the loaded hydrogen in the Pd STM-tip. Longer hydrogen loading times cause higher diffused hydrogen quantities in the bulk. Thus, the bulk hydrogen concentration stay significant longer time after the end of the loading process. The STM-tip potential was kept stable only when the hydrogen concentration in the bulk metal was high enough so that the $\alpha + \beta$ Pd/H phase coexists. This experiment shows that the Pd STM-tip, which is loaded with hydrogen, can be used as a pH-sensor if the hydrogen in the Pd-bulk is high enough to stabilize the OCP for longer time. This can be reached with glass insulation of the STM-tip and higher loading currents and times.
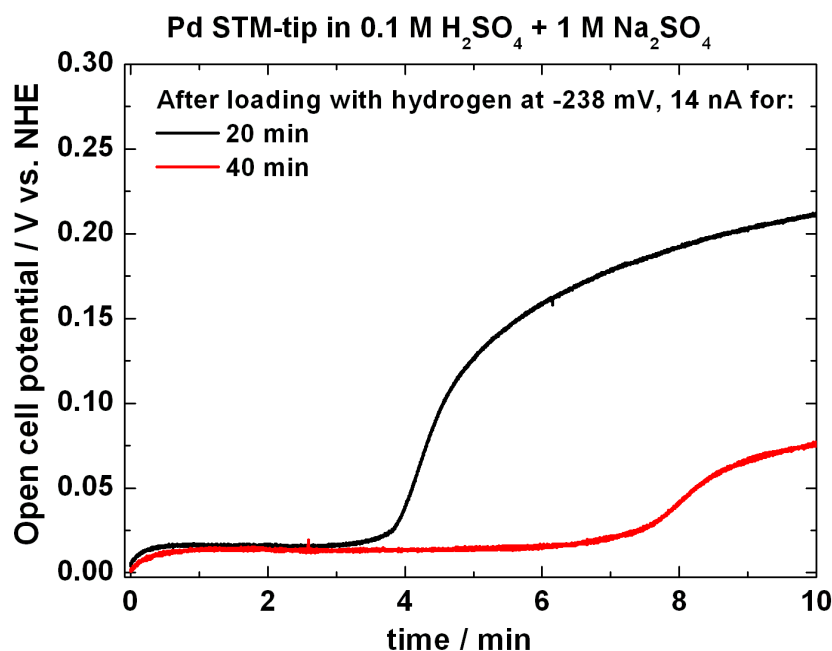
Fig.2.12: Open cell potential (OCP) of hydrogen loaded Pd STM-tip as a function of time. The black and the red curves represent the OCP time dependence after 20 and 40 min, respectively.

Chapter 3

Palladium deposition on Au(111)

In the following chapter some results of Pd deposition onto Au(111) from 0.1 M HClO$_4$ + 0.5 mM Pd(NO$_3$)$_2$ solution will be shown. The investigation of the deposition process is performed by cyclic voltammograms and *in-situ* STM images. In the first part the deposition of completed Pd layers by cyclic voltammograms and stepwise decreasing of the electrode potential will be described. The second part will present Pd sub-monolayers deposition by constant small overpotentials and by potentiostatic pulses.

3.1 Cyclic voltammetry

According to the author's knowledge, this is the first study of Pd deposition on Au(111) electrode from perchloric acid and palladium nitrate solution. The exact composition of the solution was 0.5 mM Pd(NO$_3$)$_2$ + 0.1 M HClO$_4$. The reason for using this solution was the absence of ions like sulfate and chlorate, which are strongly adsorbed on the gold surface and can contaminate the deposited palladium films. As was mentioned in the beginning of this work, the final aim is to study the reactivity regarding hydrogen evolution on palladium films on Au(111). Therefore, the deposited Pd layers should be as close as possible to the ideal surface and without impurities and defects.

The cyclic voltammetry was chosen as the first electrochemical technique applied to investigate the unknown deposition mechanism. The advantage of the cyclic voltammetry

is the fast measurement of the reduction potentials ranges and some initial information of the growth process. So, the investigated palladium reduction reaction is given by:

$$Pd^{2+} + 2e^- \xrightarrow{\ U^\theta = 0.915\ V\ } Pd(s) \tag{3.1}$$

where Pd^{2+} are the palladium ions in the solution, $Pd(s)$ is the deposited Pd and $U^\theta = 0.915$ V *vs.* NHE is the standard potential of the reaction. Using equation (1.8) and knowing the concentration of Pd^{2+} ions in the solution one can calculate the Nernst potential of the Pd reduction reaction to **0.817 V** *vs.* NHE. The correction for H^+ concentration can be also calculated and, thus the Nernst potential regarding reverse hydrogen electrode (RHE) is **0.787 V** *vs.* RHE. Therefore, at potentials more negative from the Nernst potential one can expect bulk deposition of the palladium onto Au(111) electrode from the investigated solution.

The first two cycles of a typical cyclic voltammogram (CVs) for Au(111) electrode in 0.5 mM $Pd(NO_3)_2$ + 0.1 M $HClO_4$ solution are shown in Fig. 3.1. The gold electrode was immersed into the depositing solution at 0.825 V potential, where the electrochemical behavior of Au(111) is not influenced by the presence of Pd^{2+} ions. First the potential was swept in negative direction until – 0.02 V with a scan rate of 50 mV/s. A cathodic current started to flow at approximately 0.8 V and a well defined cathodic peak was observed at 0.68 V. The deposition starts at potentials more negative than the measured equilibrium potential of Pd/Pd^{2+}. Therefore, the Pd deposition in this solution occurs only at the OPD regime. Furthermore, at potentials more negative from 0.4 V the cathodic current increases revealing a shoulder at approximately 0.2 V. During the positive "goings weep" at potentials negative from 0.6 V the net current was cathodic with a broad peak at 0.08 V. In the continuous potential sweep at potentials more positive than 0.6 V an anodic current was observed in the microampere range. The second cyclic voltammogram was performed in the same potential limits like the first one. In the negative direction potential scan only the cathodic current shoulder at a potential around 0.2 V was observed. The cathodic currents in this potential range were larger compared to the cathodic currents from the first cyclic voltammogram. Also, the currents in the positive sweep direction repeat the same behavior, excluding the position of the current peak, which is at 0.2 V.

The calculated charge density of the cathodic peak at 0.68 V from the first cyclic voltammogram is 420 $\mu C\ cm^{-2}$, corresponding almost perfectly to the deposition charge of a full Pd monolayer on Au(111) (1 ML = 423 $\mu C\ cm^{-2}$). Later the formation of the first layer will be proven by *in-situ* STM mages. The cathodic current shoulders at a potential around 0.2 V can be attributed to the hydrogen adsorption on the deposited palladium superposed with further Pd bulk deposition. Also, at the negative potential values hydrogen evolution reaction appears in addition to the Pd deposition. In the second cycle the peak can be resolved better due to the larger amount of deposited Pd. The peaks in the positive potential sweep are related to desorption of the adsorbed hydrogen from the palladium surface. The peaks in both CVs are at negative currents because of the superposition with the bulk Pd deposition.

The kinetics of deposition of the first Pd monolayer is much faster compared to the deposition process of Pd on Au(111) from sulfate solution. In the case of the sulfate solution the Au(111) surface is covered with adsorbed sulfate [33]. The adsorbed sulfate layer on the Au(111) surface impedes the deposition of the first palladium monolayer. Kolb and coworkers show that in sulfuric acid solution the sweep rate should be 1 mV/s to achieve a two dimensional growth mode for the first monolayer UPD deposited Pd on Au(111). Furthermore, Uosaki and coworkers [31, 67] report that the deposition of Pd onto Au(111) from 0.1 M H_2SO_4 solution containing K_2PdCl_4 starts at UPD region and needs a slow sweep rate of 1 mV/s to resolve the formation of the first UPD palladium monolayer. They show that the Au(111) surface is covered from adsorbed well ordered $PdCl_4^{2-}$ adlayer, which enhances the two dimensional growth for the first several Pd layers. Deposition of sub-monolayer from this solution is difficult because of the adsorbed $PdCl_4^{2-}$ complex on the electrode surface. Therefore, one should use a sulfate and chlorate free solution in order to solve the problem with the adsorbed sulfate or chlorate complexes on the electrode surface. In Fig.3.1 the peak at 0.68 V is well pronounced without shoulders and shows an almost perfect symmetry. Consequently, one cannot obtain more information about the initial stages of the deposition of the first monolayer palladium. More information for the growing mode is achievable by decreasing the sweep rate to values as small as possible. Thus, one can see a peak shoulder at more positive potentials, if the palladium deposition starts first at the gold monoatomic step edges. In addition, a cyclic voltammogram with a

sweep rate 2 mV/s was measured (Fig.3.2) to prove that suggestion. First the potential was swept in negative direction. Two cathodic peaks were observed, like in the CVs at 50 mV/s sweep rate. The peaks were attributed to the same processes explained in the case of a higher sweep rate. In the positive direction of the potential sweep no obvious peaks were recorded. The shape and the calculated charge of the deposition peak for the first monolayer at + 0.70 V was not changed compared to that one at higher sweep rates. In addition, the peak position was shifted 20 mV in the positive direction, which is expected due to the lower sweep rate (longer deposition time per potential unit). The shape of the peak was symmetric without an additional shoulder. One can interpret that the deposition process for the first monolayer starts spontaneously over the whole Au(111) surface without preference for the surface features as steps or terraces. Kolb and coworkers [33] report that for surfaces with higher defect density (Au(111) with 3° miscut) in sulfuric acid solution the deposition of the first monolayer yielded an additional peak located at a 20 mV higher potential, which for the high-quality electrode surface is discernable as a small shoulder. They attributed this peak to the Pd deposition at the surface defects like monoatomic high steps. The existence of preferred deposition on the monoatomic step
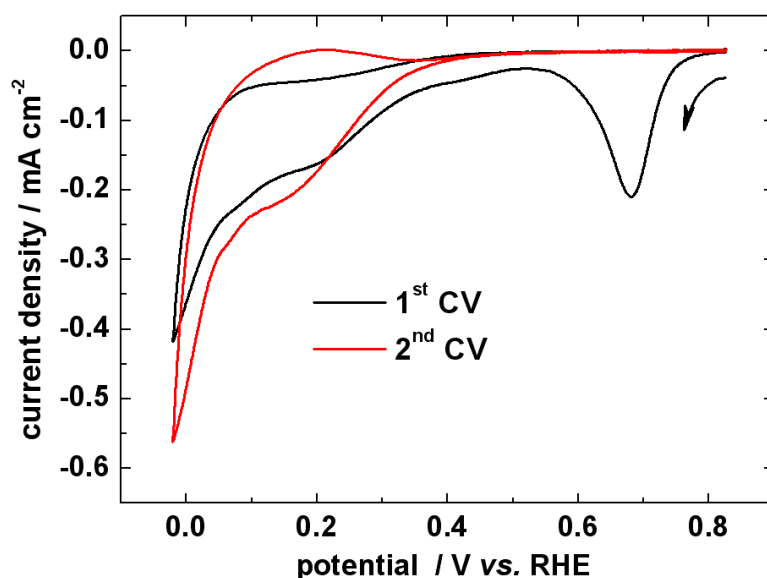

Fig.3.1: Cyclic voltammograms for Au(111) in 0.1 M HClO$_4$ with 0.5 mM Pd(NO$_3$)$_2$ solution. Initial potential 0.825 V *vs.* RHE. Sweep rate 50 mV/s. The measured equilibrium potential for Pd/Pd^{2+} in that solution is 0.8 V.

edges can be explained by the adsorbed sulfate layer. The flat gold terraces are covered with a well-ordered sulfate layer. Only the step edges have disordered sulfate coverage full of vacancies. At 0.68 V should be expected some adsorbed oxygen at the step edges, which can induce additional defects in the sulfate adlayer [50, 51]. The Pd deposition starts at the places where the adsorbed sulfate layer is weaker, namely at the monoatomic high steps. Thus, in sulfuric acid solution the size of the additional peak is characteristic of the quality of the surface. In the case of perchloric acid solution the gold surface is free from strongly adsorbed anions and the deposition process starts simultaneously at the monoatomic high steps and at the atomically flat terraces. Therefore, the deposition peak is symmetrical without shoulders. Further pronounced deposition peak for the second monoatomic layer Pd was not observed, like in sulfuric acid solution for Au(111) electrode with high defect density [33]. Hence, from the CVs in the Fig.3.1 and Fig.3.2 one can conclude that the deposition of the first monolayer Pd is OPD with 2D growth mode and the deposition of the next layers is with 3D growth mode (Stranski-Krastanov growth mode). In the next sections the two dimensional deposition of the second layer using a very low overpotential and longer deposition times will be   shown. In order to investigate the system behaviors in more detail, the cyclic voltammetric measurements were performed over a wide range of
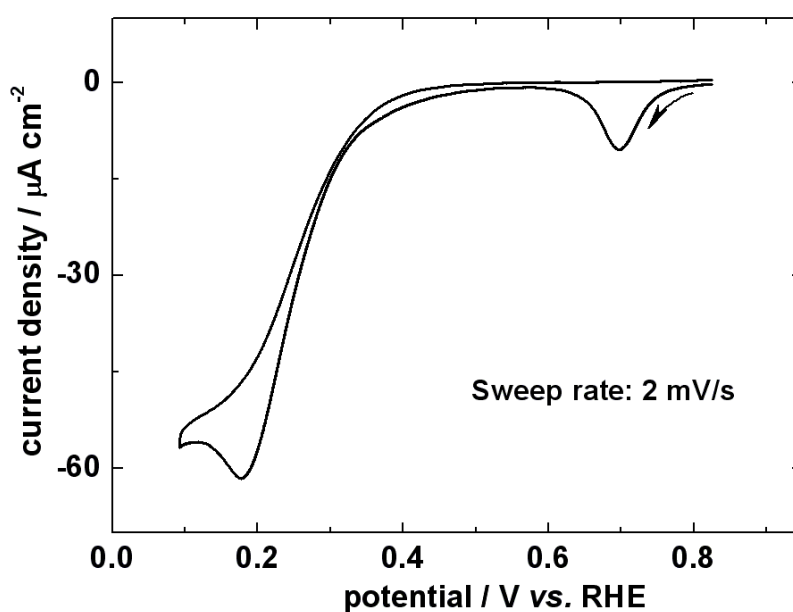

Fig.3.2: Cyclic voltammogram for Au(111) in 0.1 M HClO$_4$ with 0.5 mM Pd(NO$_3$)$_2$ solution. Initial potential 0.825 V *vs.* RHE. Sweep rate 2 mV/s.

sweep rates. The results are shown in Fig.3.3. The sweep rate was varied from 10 mV/s to 800 mV/s. As can be seen, the magnitude of the current increases with an increase of the scan rate. This can be explained with the modified Randles-Sevcik equation for the current peak height of irreversible and quasi-reversible reaction [68, 69]:

$$i_p = (2.99 \times 10^5) n (\alpha n_a)^{1/2} ACD^{1/2} v^{1/2} \tag{3.2}$$

where n is the number of electrons, A the electrode area (in cm^2), C the concentration of the reactant in the solution (in mol/cm^3), D the diffusion coefficient (in cm^2/s), v the sweep rate (in V/s), n_a is the number of electrons involved in the charge-transfer step and α is the transfer coefficient. It is obvious from equation 3.2 that with increasing of the sweep rate the current peak increases. In table 3.1 the peak height, peak position, end potential of the peak and the charge density of the peak as a function of the sweep rate are shown. As an end potential is termed the potential of the cathodic current minimum (where the current for the deposition of the first monolayer is finished). The peak position shifts to more negative values when the sweep rate is increased. This behavior can be explained by the irreversibility of the reaction. In the same manner, the end potentials shift to more negative
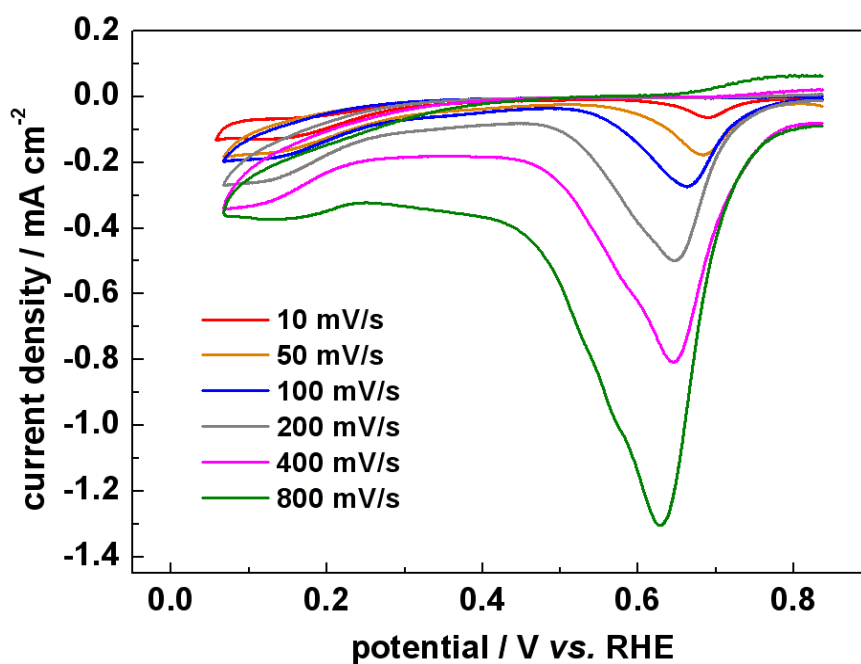

Fig.3.3: Cyclic voltammograms of Au (111) in 0.1 M HClO₄ with 0.5 mM Pd(NO₃)₂ taken at different scan rates.

values with increasing sweep rate (Table.3.1), can be explained with the shorter deposition time per potential range. The deposition of the first monolayer needs a defined time jump because of the surface diffusion of the adsorbed atoms (every atom should find a free space on top of the Au(111) surface). The calculated charges from the cathodic peaks at approximately 0.68 V from Fig.5.3 are in the range of the charge for one ML palladium on Au(111), namely 420 $\mu C\ cm^{-2}$ (Table.3.1). The measured deviations are due to the different electrochemical active area compared to the geometrical area. In the evaluations the geometrical area was used. At the highest sweep rate (800 mV/s) the charge is 10 % less than the needed charge for a completed monolayer. The fact of an uncompleted layer might be explained with the shorter deposition time.

Fig.3.4 illustrate the dependence of the peak height on the square root of the sweep rate. Herein two linear parts of the curve are shown with a cross point of 100 mV/s. This provides an evidence of the existence of different deposition kinetics, working below and over the value of 100 mV/s. At lower sweep rates the deposition kinetic is probably defined by the charge transfer. However, at higher sweep rates dominates the mass transfer or diffusion controlled deposition. The evaluated slope of the linear part below 100 mV/s sweep rate is 0.03 $mA\ cm^{-2}s^{0.5}mV^{-0.5}$ and over 100 mV/s is 0.055 $mA\ cm^{-2}s^{0.5}mV^{-0.5}$, respectively.

According to equation 3.2 two times of the slope difference gives four times the transfer

Table.3.1 The peak height, peak position, end potential of the peak and the charge density of the peak as a function of the sweep rate

Sweep rate mVs^{-1}	Peak height $mA\ cm^{-2}$	Peak position V	End potential V	Charge $\mu C\ cm^{-2}$
2	0.010	0.693	0.56	426
10	0.063	0.690	0.55	440
50	0.176	0.680	0.51	436
100	0.270	0.662	0.49	410
200	0.500	0.646	0.45	408
400	0.810	0.644	0.36	402
800	1.3	0.628	0.28	380

coefficient difference. So, if the transfer coefficient for the second part at higher sweep rate is substituted by the value of 2, than the calculated value at lower sweep rates should be equal to 0.5. It is in a good agreement with the well known values of transfer coefficients for diffusion-controlled and charge transfer reactions [42, 43]. This results support the deposition kinetics based on Fig. 3.4. In order to investigate the Pd deposition of partial monolayers (sub-MLs) onto Au(111) from 0.5 mM $Pd(NO_3)_2$ + 0.1 M $HClO_4$ solution, the cyclic voltammetric measurements were performed over a wide range of lower potential limits. The measured CVs are shown in Fig.3.5. The cyclic voltammograms were swept from an initial potential 0.842 V. The lower potential limits were varied as follows: 0.58 V, 0.63 V, 0.65 V, 0.67 V and 0.7 V. Each cyclic voltammogram was recorded with a freshly prepared Au(111) electrode. Once deposited on the Au(111) electrode, the palladium layers cannot be dissolved. It seems that the curve shape during the negative potential sweep and the cathodic current maximum are absolutely the same for each CV. Thus, one can assigned that the deposition process did not depend on the electrode structure, because each CV is measured on a different Au(111) electrode with more and less different surface properties. One other interesting finding from the Fig.3.5 is that the deposition of the first layer is realizable over a wide potential range after passing over the cathodic peak
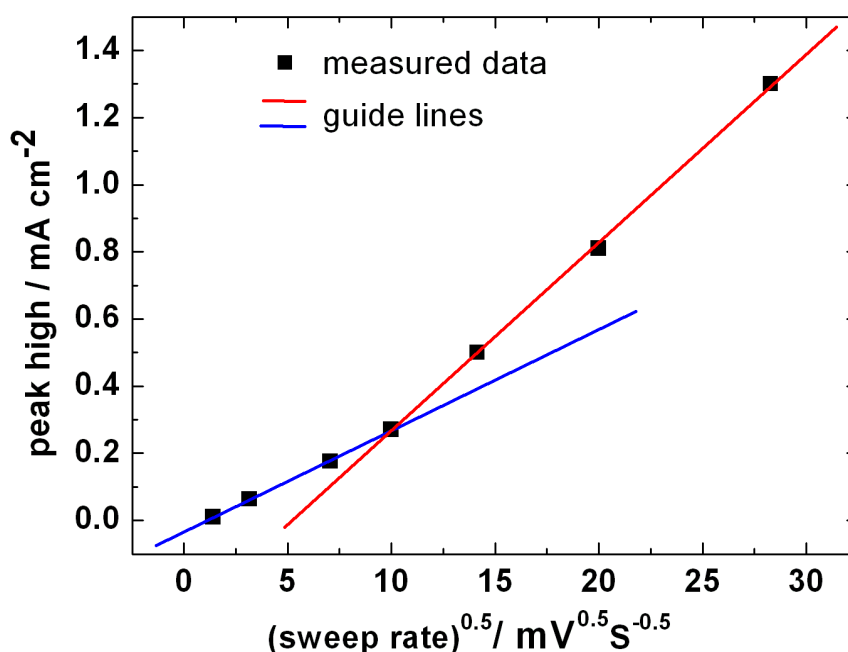
Fig.3.4: The peak height from Fig.3.3 as a function of square root of sweep rate. The bulk squares are the measured data and the solid lines are guide for the eye.

maximum at approximately 0.68 V. The surface coverage calculated from the charge densities for all potential limits were: 1 ML, 0.93 ML, 0.91 ML, 0.82 ML and 0.53 ML. Calculated charge tending to one monolayer response to the CVs presented on Fig. 3.5 with lower potential limit more negative than the potential of the cathodic current maximum. The deposition of sub-monolayers with palladium coverage below 0.5 ML should be performed by CVs with lower potential limit larger than 0.7 V. The cyclic voltammogram with lower potential limit 0.7 V measured before the cathodic current maximum demonstrate the same current shape in the both potential sweep directions.

According to the author's knowledge, this is the first study showing such kind of deposition process behavior. The additional section of the study will be presented where the deposition of the sub-monolayers by the proposed technique will be investigated with electrochemical scanning tunneling microscope.

Fig.3.5: Cyclic voltammograms of Au (111) in 0.1 M HClO$_4$ with 0.5 mM Pd(NO$_3$)$_2$ at different lower potential limits.

3.2 Electrochemical STM study

In this section *in-situ* EC-STM investigation of the Pd electrochemical deposition process onto Au(111) from 0.5 mM Pd(NO$_3$)$_2$ + 0.1 M HClO$_4$ solution will be presented. In the first part the deposition of the first OPD monolayer palladium using the potential swe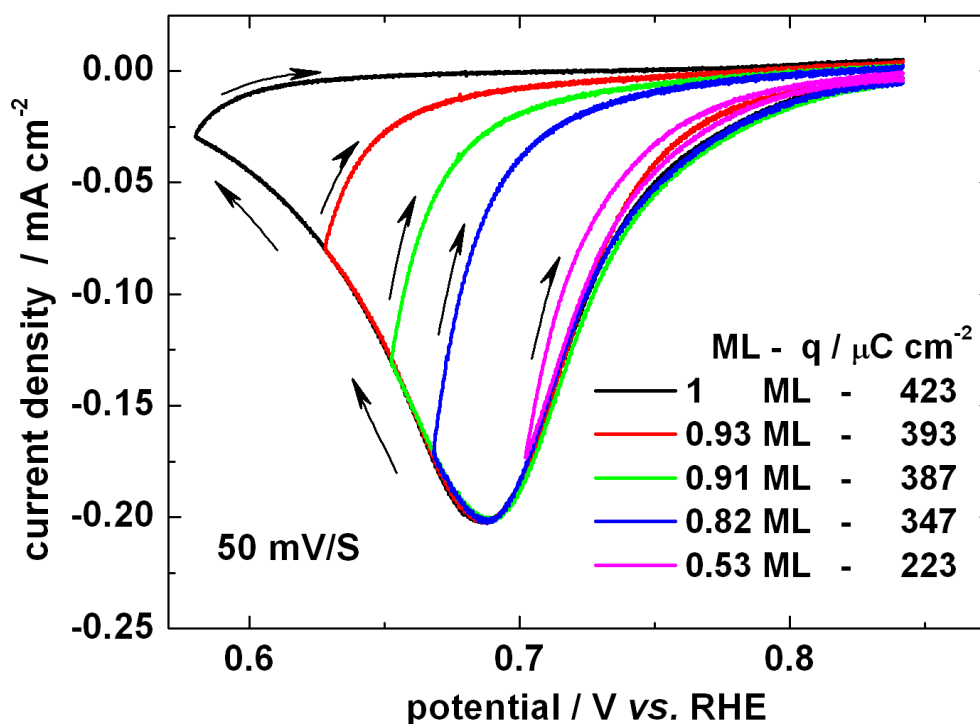ep method is explained. The second part will illustrate the formation of two complete layers using stepwise increasing of the overpotential. The third part will characterize the deposition of Pd monoatomic nano-islands by potentiostatic pulse technique.

3.2.1 Palladium deposition by potential sweep method - formation of the first monolayer

Based on the previous section, the deposition of the first palladium monolayer onto A(111) is defined by the cathodic peak in the CVs over a wide range of sweep rates. The calculated charge density of the peak corresponds well with the charge of one monolayer palladium on Au(111). For more details, the deposition process was performed parallel with *in-situ* EC-STM measurements.

In Fig.3.6 and Fig.3.7 the deposition of the first monolayer palladium by potential sweeps are shown. The CVs of deposition of the first Pd ML on Au(111) are shown in Fig. 3.7c. Here in the first CV the potential was swept down to 0.67 V from 0.84 V initially in the negative direction by 20 mV/s. The calculated charge corresponding to the first CV was 354 μC cm^{-2}, which is equivalent to 0.84 ML Pd deposited onto the Au(111) surface. In the second and in the third CV the calculated charge was 57 μC cm^{-2} and 18 μC cm^{-2}, respectively. Therefore, the Pd coverage after the second CV was 0.96 ML and after the third CV one monolayer was completed. Fig.3.6 and Fig.3.7 show the STM images of the electrode surface before, during and after the deposition CVs. The arrows in the images indicate the area where the CV was performed. In order to get a better understanding a z - profile of the marked parts from the images are shown underneath. Fig.3.6a shows the STM image of the initial electrode surface of bare Au(111) consisting of monoatomic terraces and several monoatomic high islands, at an initial potential 0.84 V. The spontaneous lifting of the thermally induced reconstruction leaves a surface with monoatomic high gold island [70]. Based on the z - profile of the image (a)
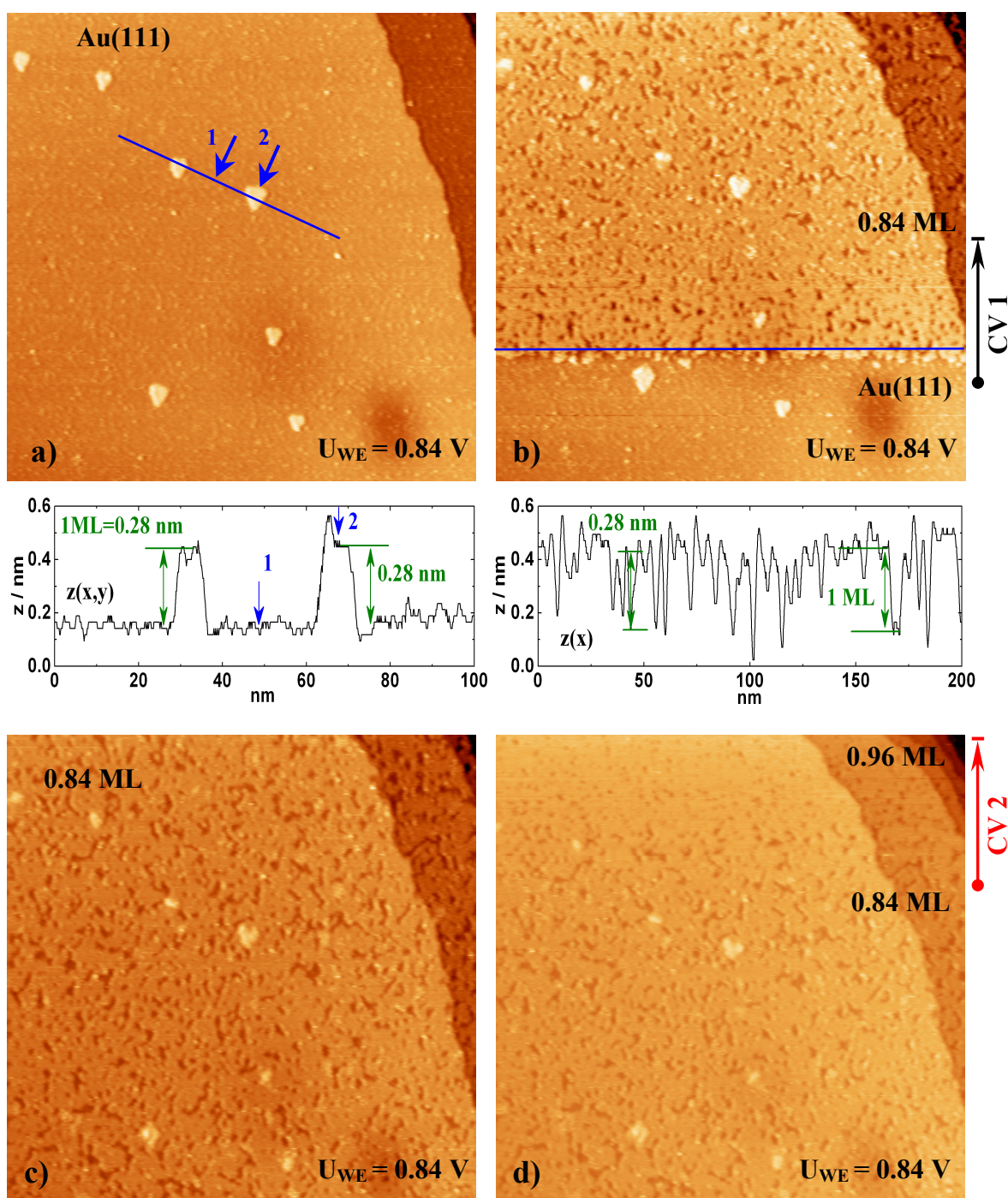
Fig.3.6: Sequence of STM images, showing the initial of Pd deposition onto Au(111) using CVs in 0.5 mM Pd(NO$_3$)$_2$ + 0.1 M HClO$_4$. STM images: (a) before CV1, (b) during CV1, (c) after CV1 and (d) during CV2 from Fig.3.6c, (next page). For all STM images: I$_{tip}$ = 1 nA, U$_{WE}$ = 0.84 V, U$_{tip}$ = 0.93 V. With the arrows the scan direction and the part of the images where the CVs are performed, are shown. Additionally, z – profiles of the marked image positions are shown below the corresponding images. All images are 200 x 200 nm with a scan rate 1300 nm/s
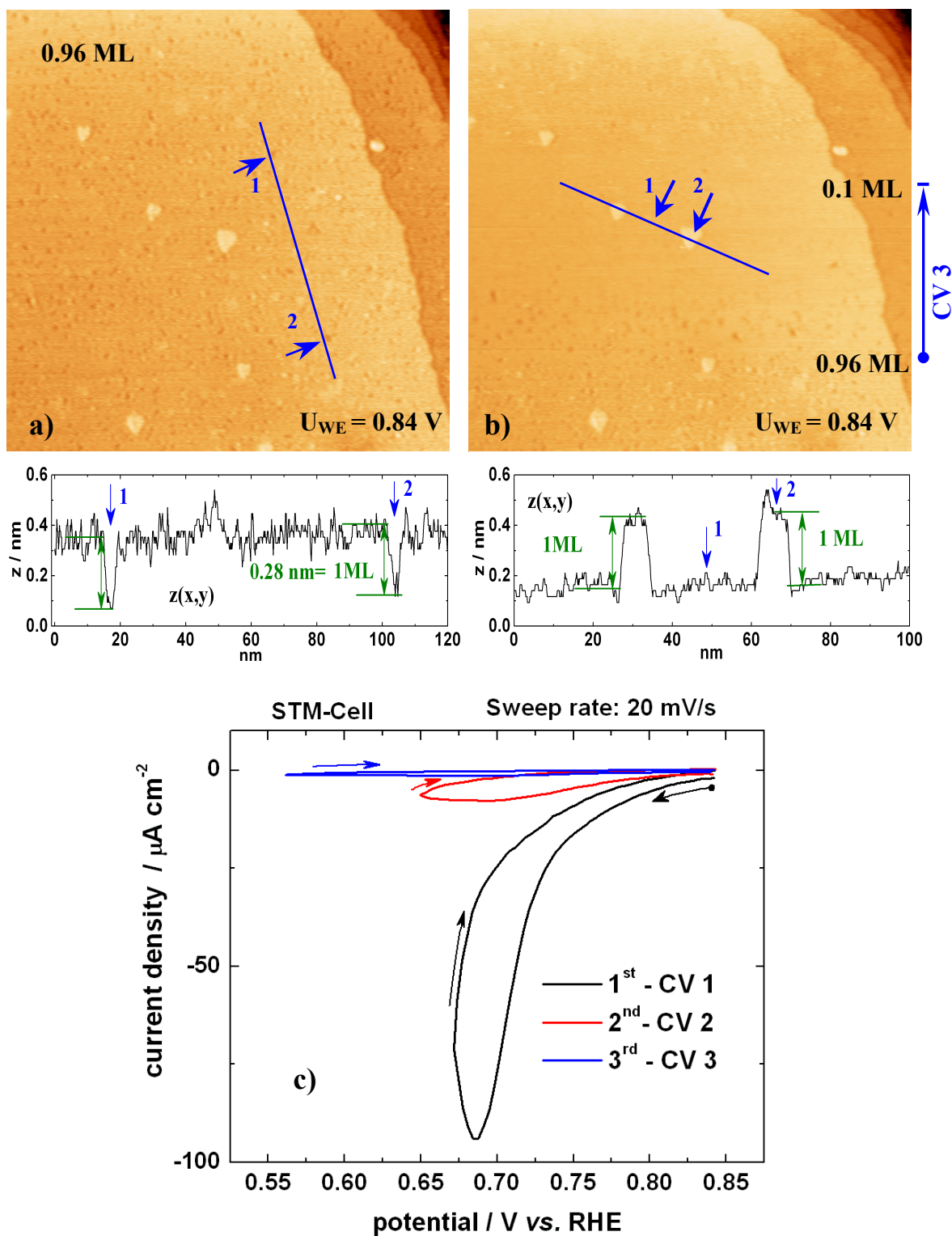
Fig.3.7: Corresponding to Fig.3.6 (a) after CV2 and (b) during CV3 from (c), respectively. (c) The first three cyclic voltammograms of Pd deposition onto Au(111). The Pd coverage corresponds to the charge density after CV1, CV2 and CV3 is 0.84 ML, 0.96 ML and 1 ML, respectively

it becomes obvious that the islands on the surface are monoatomically high, respectively 0.28 nm high. Prior the first CV of the substrate surface was free from Pd nuclei. The changes of the morphology of the Au(111) electrode surface during the first CV are illustrated in Fig.3.6b. It seems that immediately after the execution of the first CV (CV1) the Pd deposition starts and the Au(111) surface is quickly covered with one uncompleted Pd monolayer. At the place of the image pointed with a blue line z - cross-section analyze is performed. From the z - profile it can be easily seen that the surface is dotted with huge number of monoatomic deep holes. The image (c) from Fig.3.6 presents the electrode surface at a potential of 0.84V after the first CV. The calculated Pd coverage based on the charge from the first CV is 0.84 ML. The amount is in good agreement with the information estimated from the image. The surface after the CV1 reproduce the morphology of the Au(111) substrate excluding the numerous monoatomic deep holes due to the uncompleted first Pd monolayer. The second CV (CV2) is performed during the image (d) from Fig.3.6. Here the monoatomic deep holes are reduced during the CV2. After CV2 the number of the holes and the averaged area of one individual hole decreased. This fact of free Au(111) (the monoatomic deep holes) surface reduction fit to the evaluated charge from CV2 and also correspond to the further deposition of 0.14 ML Pd. Fig.3.7a shows the electrode surface after CV2. The z - profile of the image illustrates that the vacancies in the terraces are still monoatomic deep. The following image (b) from Fig.3.7 illustrates the electrode surface during the execution of the third CV (CV3). The monoatomic deep holes disappear after CV3 and the surface is covered with one completed monolayer of Pd. The z - profile of the marked line from the image shows that on the surface monoatomic high islands positioned exact to the islands from the Au(111) substrate exist (Fig.3.6a). Therefore, the surface morphology of the gold is not altered from the deposition of one monolayer Pd. Kolb and coworkers [33] pointed out that the overpotential for Pd nucleation on Au(111) in sulfuric acid solution is markedly higher on terraces than at steps. In the case of perchloric acid solution no difference in the overpotential for Pd nucleation on terraces and steps was observed. From this point of view, it seems that the presented fact is due to the sulfate adlayer on top of the Au(111) terraces, which is able to hinder the formation of the Pd nuclei.

As a conclusion of the above mentioned results it seems that using CVs with a sweep rate 20 mV/s, one Pd monolayer can be deposited. The experiments performed at a sweep rate

of 50 mV/s and 100 mV/s result in an equal performance, namely one complete Pd monolayer on the Au(111) surface. It will be discussed in one of the next sections that 2D growth of the first Pd monolayer can be achieved by potential step also.

3.2.2 Deposition by stepwise increase of the overpotential

Using a stepwise increase of the overpotential more information can be obtained for the growth mode for any deposition processes. The first Pd layer was grown two dimensionally on Au(111) electrode. The information for the growth mode of the next Pd layers is obtained in the following experiment.

The sample was adjusted in the STM-cell according to the assembling procedure described in the experimental part. The initial potential was 1 V, where no reactions of gold oxidation or Pd deposition takes place. The resulted series of 9 STM images of Pd deposition onto Au(111) from 0.1 M $HClO_4$ + 0.5 mM $Pd(NO_3)_2$ are shown in Fig.3.8. The initial surface of the Au(111) electrode (Fig.3.8a) consists of monoatomic high terraces. First the potential was lowered to 0.78 V for 9 minutes. The electrodeposition of Pd started simultaneously at the monoatomically high steps and terraces (Fig.3.8b). In the next step the potential was further decreased to 0.73 V for a period of 3 minutes. The monoatomic high Pd islands progressively grow two dimensionally and cover gradually the whole Au(111) surface with an uniform monolayer (Fig.3.8c-d). The first monolayer Pd was completed in 12 minutes. Afterwards to decrease further the electrode potential two steps were used. In the first one the potential was reduced to 0.66 V for 33 minutes and in the second the potential was drop down to 0.64 V for 25 minutes. The growth of the second Pd monolayer follows the same behavior like the first one (Fig.3.8e). Small Pd islands were formed simultaneously on top of the whole surface revealing a relatively round shape. These islands gradually merge and form an almost complete second monolayer (Fig.3.8f), which still reproduces the Au(111) substrate morphology like the first Pd monolayer. A three-dimensional (3D) growth is observed after potential step at 0.4 V (Fig.3.8q-i). In the beginning the 3D-islands are characterized showing smaller size and higher density. After 9 minutes deposition at 0.4 V (5 ML deposited Pd) the 3D islands gradually merge and form 3D flat plateaus. Subsequently, the plateaus are transformed into 3D spirals (Fig.3.8i). This spiral type of growth arise from the crystallographic misfit between the

j)	time / **min**	0 - 9	10 - 12	13 - 45	46 - 70	71 - 130
	potential / **V**	0.78	0.73	0.66	0.64	0.4
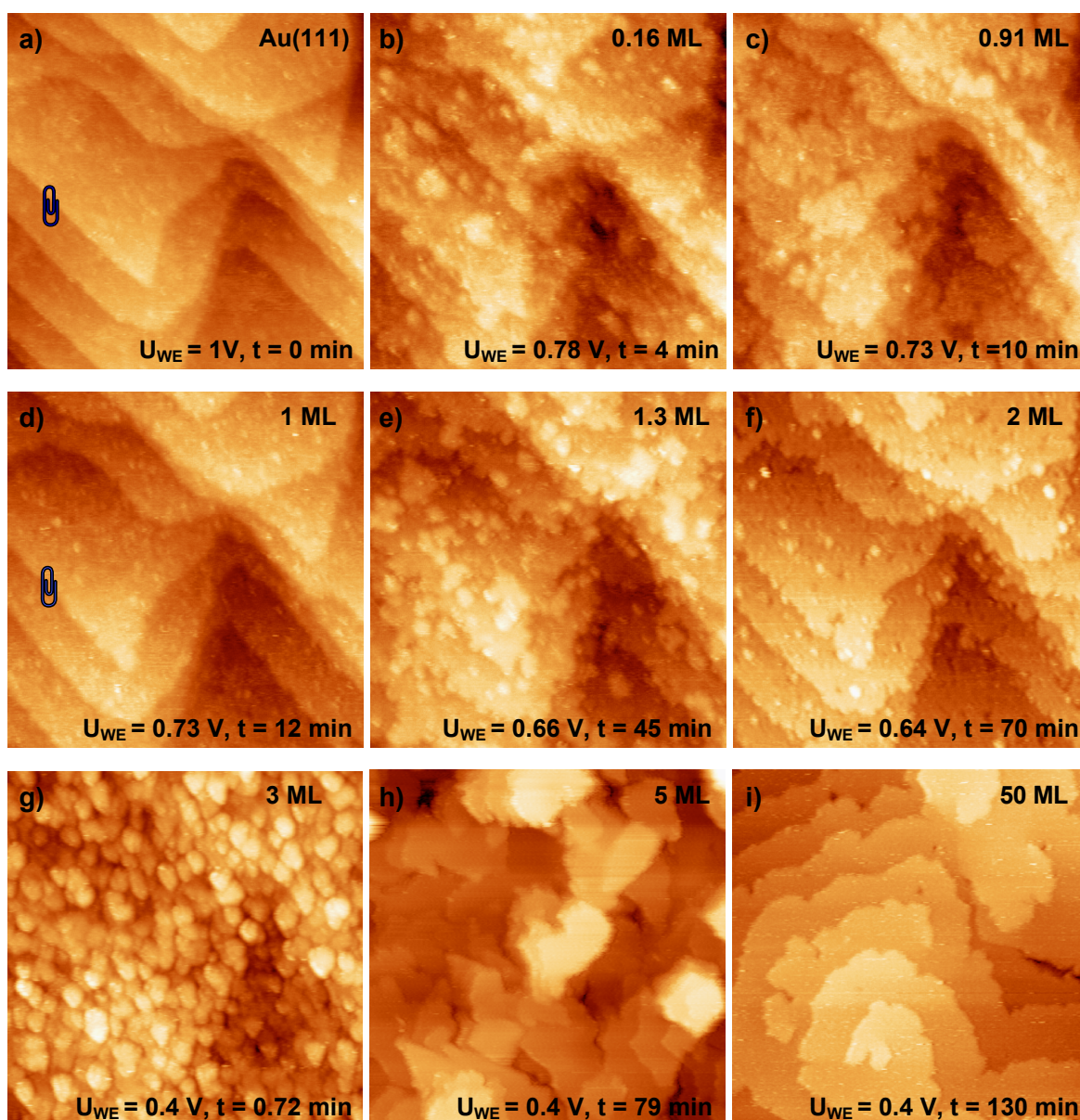
Fig.3.8: Sequence of STM images, showing Pd deposition onto Au(111) in 0.5 mM Pd(NO$_3$)$_2$ + 0.1 M HClO$_4$ by stepwise increasing of the overpotential. Image size is 100x100nm, scan speed 140 nm/s, I$_{tun}$ = 1.1 nA and U$_{tun}$ = U$_{WE}$ - U$_{tip}$ = - 200 mV.

The calculated Pd coverage from the cathodic current, electrode potential and the time at which the images were taken: (a) 0 ML - Au(111), 1 V(double layer); (b) 0.16 ML, 0.78 V after 4 min.; (c) 0.91 ML, 0.73 V after 10 min; (d) 1 ML, 0.73 V after 12 min.; (e) 1.3 ML, 0.66V after 45 min.; (f) 2 ML, 0.64 V after 70 min.; (g) 3 ML , 0.4 V after 72 min.; (h) 5 ML, 0.4 V after 79 min.; (i) 50 ML, 0.4 V after 130 min.

(j) Sequence of the electrode potential changes.

Au(111) substrate and Pd 3D bulk deposits. The deposition times for the first monolayer and for the second monolayer were 12 and 58 minutes, respectively. The slower deposition kinetics for the second monolayer can be explained with the NO adsorbed layer on top of the first Pd monolayer in 0.1 M HClO$_4$ + 0.5 mM Pd(NO$_3$)$_2$ solution. The NO is adsorbed weakly on the Au(111), but very strongly on the Pd surface. A similar observation is found for CO adsorption. Therefore, the diffusion of Pd atoms on an Au surface is faster compared to the Pd surface. The definite evidence of the presence of NO adsorbate layer on top of the deposited Pd layers will be presented in the next chapter.

Thus, the last experiment shows that the first two Pd monolayers can be deposited 2D layer-by-layer using low overpotentials and longer deposition times. That technique will be used for the preparation of Pd deposits on Au(111) up to several layers.

The growth mode for Pd deposition onto Au(111) from 0.1 M HClO$_4$ + 0.5 mM Pd(NO$_3$)$_2$ solution is similar to the growth mode in sulfuric acid solution [33]. J. Tang *et al.* reported that the deposition of the first two Pd layers onto Au(111) from sulfuric acid solution is layer-by-layer and the deposition of the next layers is revealing a three-dimensional growth. The deposition time for the first and for the second Pd monolayers in sulfuric acid solution is approximately the same. A possible explanation of this result is that the sulfate anions are strongly adsorbed on Au(111) as well as on Pd.

3.2.3 Deposition of sub-monolayers by small constant overpotentials

The objective of the following experiments is the investigation of the initial stages of deposition of sub-monolayers. The motivation behind using a small constant overpotential deposition is based on the possibility of varying the islands diameter. A further advantage of the technique is that the control of the size (diameter) of the deposited islands provides also control of the ratio of the edge atoms/terrace atoms. Thus, the influence of the edge atoms on the reactivity can be investigated.

In the following experiment the main attention is focused on the Pd deposition with lower number density and bigger island sizes. Thus, the overpotential was kept at lower values for longer time until the Pd deposits reach the desired size. Fig.3.9 show a series of STM images for such kind of experiment. In the beginning at 1 V electrode potential the
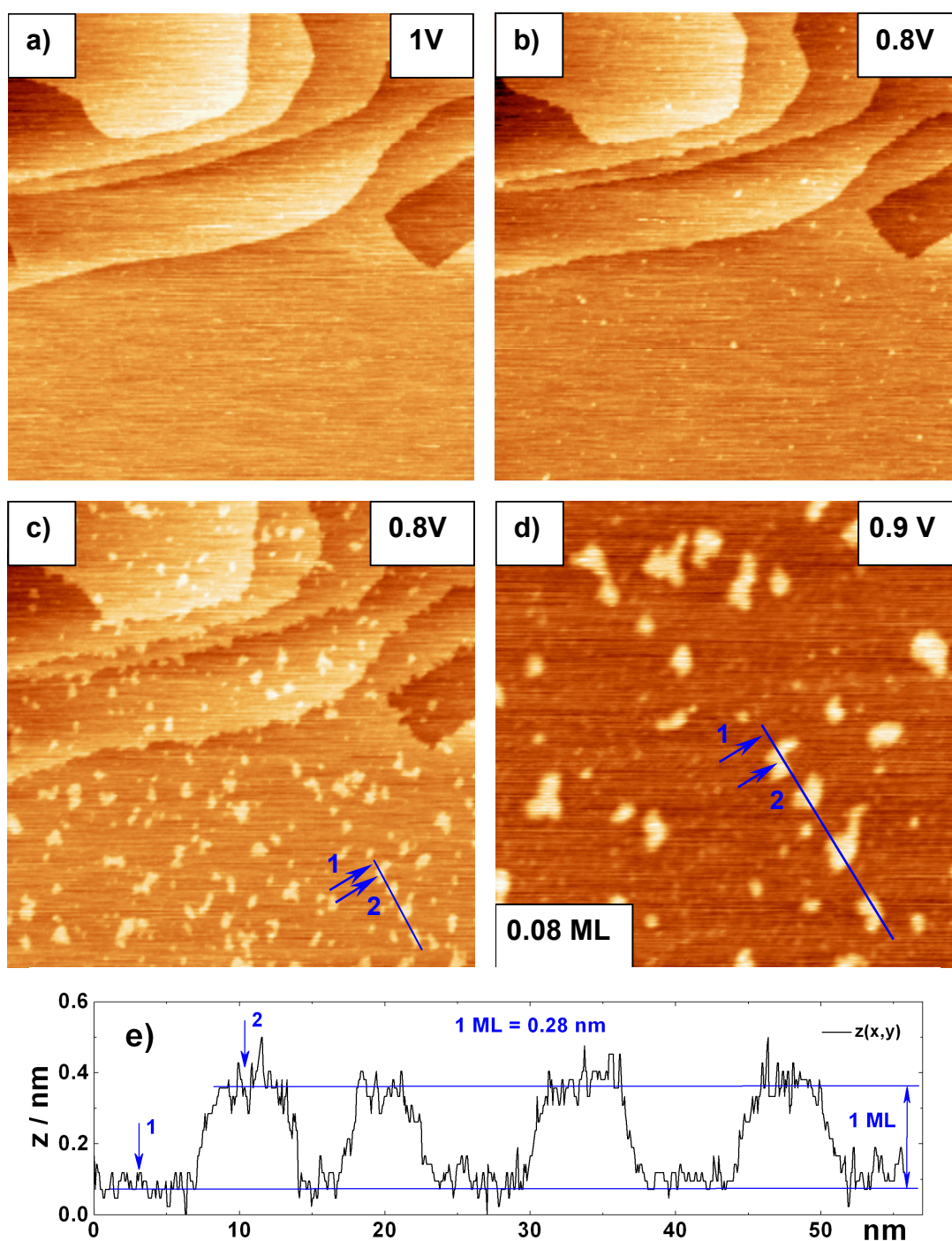
Fig.3.9: Series of STM images, showing potentiostatic deposition of sub-ML Pd onto Au(111) in 0.5 mM $Pd(NO_3)_2$ + 0.1 M $HClO_4$. At all images: I_{tip}= 1 nA; U_{tip}= 0.9 V; scan speed 900 nm/s. The initial potential was 1 V image (a), then the potential was dropped down to 0.8 V images (b) and (c) for 13 minutes. The electrode potential of image (d) was 0.9 V. The size of the images is: (a)-(c) 200 x 200 nm and (d) 100 x 100 nm. The z-profile (e) from the marked part from image (d) is shown below the images.

Au(111) surface was free of Pd nuclei (Fig.3.9a). The potential was dropped down to 0.8 V where Pd electrodeposition starts spontaneously on the whole Au(111) surface (Fig.3.9b). Consequently, the nuclei are transformed into small Pd islands with round shape and progressively increase their size with time. After 13 minutes the average size of the islands is about 8 nm (Fig.3.9c). Afterwards the potential was increased back to 0.9 V in order to stop further Pd deposition shown in Fig.3.9d. The Au(111) surface was covered with monoatomic high Pd nano-islands with different size and shape. Some of the islands merge during the growth process to form a large one. The evaluated diameter distribution of the Pd islands was pretty wide (range from 1 nm up to 13 nm). The last finding can be explained with the progressive Pd nucleation on the Au(111) surface. The large defects number into Au(111) samples make them able to act as an additional nuclei. In the next section will be shown that the number of Pd nuclei can vary in some borders by the height of the potential pulse.

3.2.4 Deposition of sub-monolayers by potential pulse technique

In the previous section the deposition of sub-monolayers Pd on Au(111) with small overpotentials and longer deposition times, resulting in a wide size distribution of the deposited Pd monoatomically high nano-islands was discussed. Investigation of the reactivity dependence on the island size needs a deposition technique such as the potential pulse, which is able to deposit Pd with a narrow island size distribution. On one hand varying the potential height of the pulse U_f, the number of Pd nuclei on the Au(111) surface can also vary. At high overpotentials the number of the formed nuclei is higher compared to the ones formed at lower overpotentials. On the other hand, varying the duration of the pulse the island size can be controlled. The longer potential pulse duration results in a larger island size. Hence, by modifying two of these parameters different surface morphology structures can be deposited for the same coverage Pd on Au(111).

The sample was adjusted in the STM-cell according to the assembling procedure described in the experimental part of this thesis. The working electrode area, which is in contact with the solution, was 0.13 cm^2. Due to the lower deposited coverage and the smaller working electrode contact area the deposition current transients were expected to be few microamperes. Thus, the measured deposition current transients expect to be in the range of the currents, which arise due to the rest oxygen reduction in the solution. In order to

estimate the magnitude of the current induced by the rest oxygen in the deposition transients the following experiments were performed: current transients with the same potential pulse parameters like the deposition transients but in Pd free solution were recorded. The cells were purged with nitrogen for one hour prior each experiment in order to get equal amounts of the rest oxygen. The evaluated charges from the current transients measured in Pd free solution gives the charges resulting from the reduction of the rest oxygen in the solution. This charge is subtracted from the charges evaluated from the transients in Pd containing solution. Thus, the real deposition charges were calculated and the deposited amount of Pd can be evaluated properly.

Fig.3.10 shows the applied potential pulse to the working electrode and the recorded current transient for the Pd deposition experiment. The initial potential for each potential pulse deposition experiments is 0.95 V. The applied potential pulse for one of the performed experiments is shown in Fig.3.10a. The switching time of the potential to the new value was shorter than 100 microseconds (Fig.3.10c), fast enough for our purpose. The duration of the potential pulse was 1 s. Fig.3.10b illustrates the recorded current transient response of the applied potential pulse. At time t_0, when the potential pulse is executed, the current arise very fast due to discharge of the double layer of the system (the first 100-200 μs Fig.3.10e). Afterwards the recorded current transient originates from Pd^{2+} ion discharge and represents pure deposition current (Fig3.10d). At time t_f, when the potential was switched back to the initial potential, the recorded current switches to positive currents originated only from the charging of the double layer. The measured current transient between t_0 and t_f represents the current amplitude due to double layer discharge, Pd deposition and oxygen reduction of the rest oxygen in the solution. The charge due to oxygen reduction was calculated from the performed measurements in Pd free solution with the same experimental parameters. However, for the calculation of the double layer discharge current the second part of the measured transient in the Pd containing solution for times larger than 1 s ($t > t_f = 1$ s) is used. The Pd deposition charge is received by subtraction of the sum of the charges induced from rest oxygen and double layer discharge. The deposited amount of Pd onto Au(111) was easily determined using the final Pd charge. Furthermore, the deposited Pd was controlled by the STM images obtained after the deposition pulse (Fig.3.11). STM images were taken before and after the potential pulse.
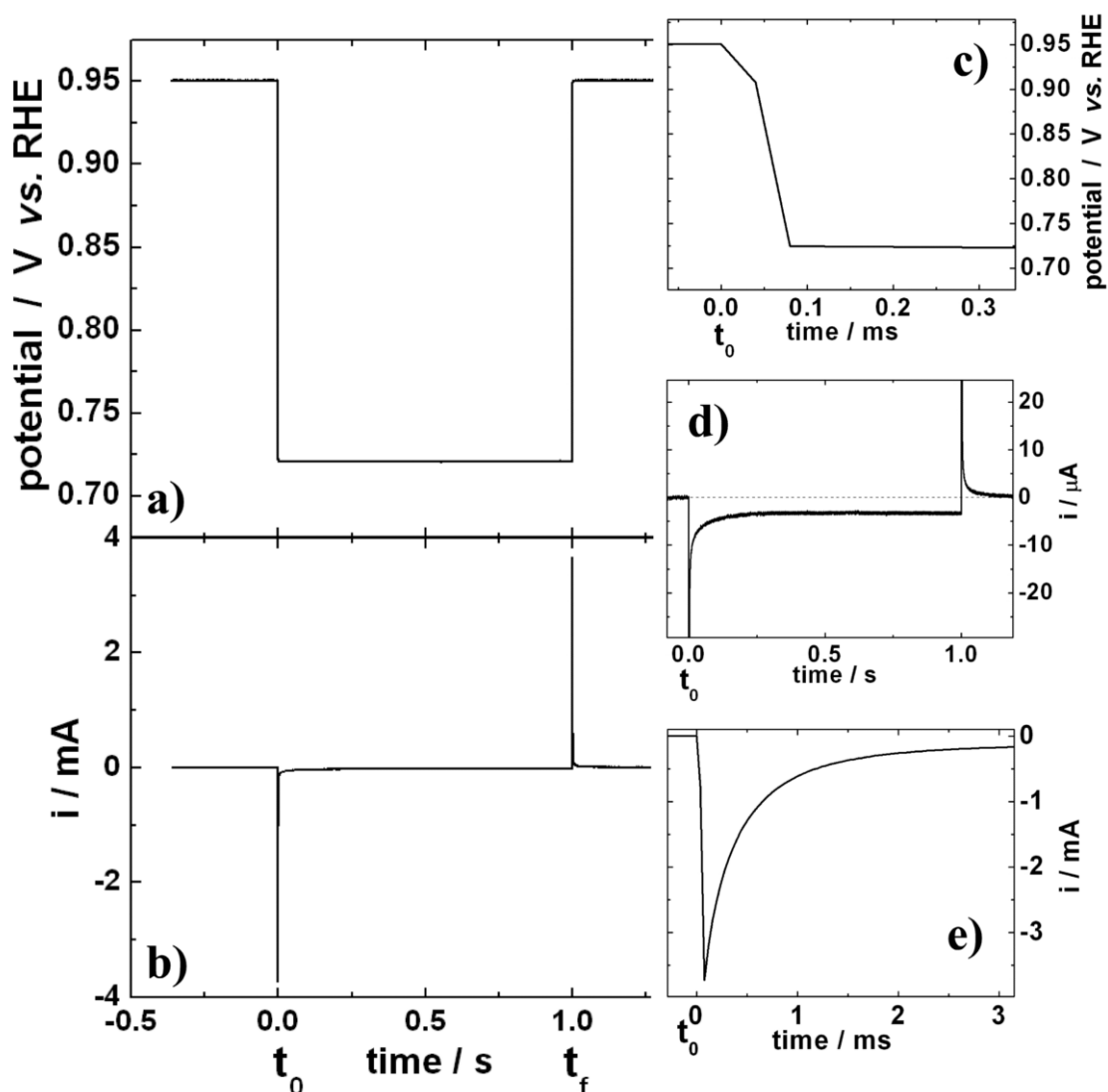
Fig.3.10: Example for potential pulse deposition experiment of Pd onto Au(111) in 0.1 M HClO$_4$ + 0.5 mM Pd(NO$_3$)$_2$ solution: (a) the applied potential pulse from 0.95 V down to 0.72 V; (b) the recorded deposition current transient; (c) the potential pulse from (a) at higher time resolution; (d) the current transient from (b) at higher current resolution and (e) the current transient from (b) at higher time resolution. The calculated deposited amount of Pd was 0.035 ML.

The images before the pulse were obtained in order to check the state of the surface after the long purging of the solution (1 hour) with argon or nitrogen. The procedure of the evaluation of the coverage from the STM images is explained in the next chapter.

In Fig.3.11 STM images of sub-monolayers Pd deposited onto Au(111) by potential pulse technique are shows. The distribution of the islands perimeter for the imaged areas are also presented in Fig. 3.11. The evaluation of the distribution of the island perimeter will be

explained in the next chapter. The images are obtained at an electrode potential of 0.95 V, tip potential of 0.85 V and tunneling current of 1 nA. The scan rate was 500 nm/s. The first image shows 0.035 ML Pd on Au(111) deposited applying a potential jump to 0.72 V for 1 s (Fig.3.11a). From the island perimeter distribution it can be clear that the islands are monoatomically high with a perimeter around 4 nm or diameter range of 1.3 nm. The total number of the islands on the image was counted to 284. The second image shows
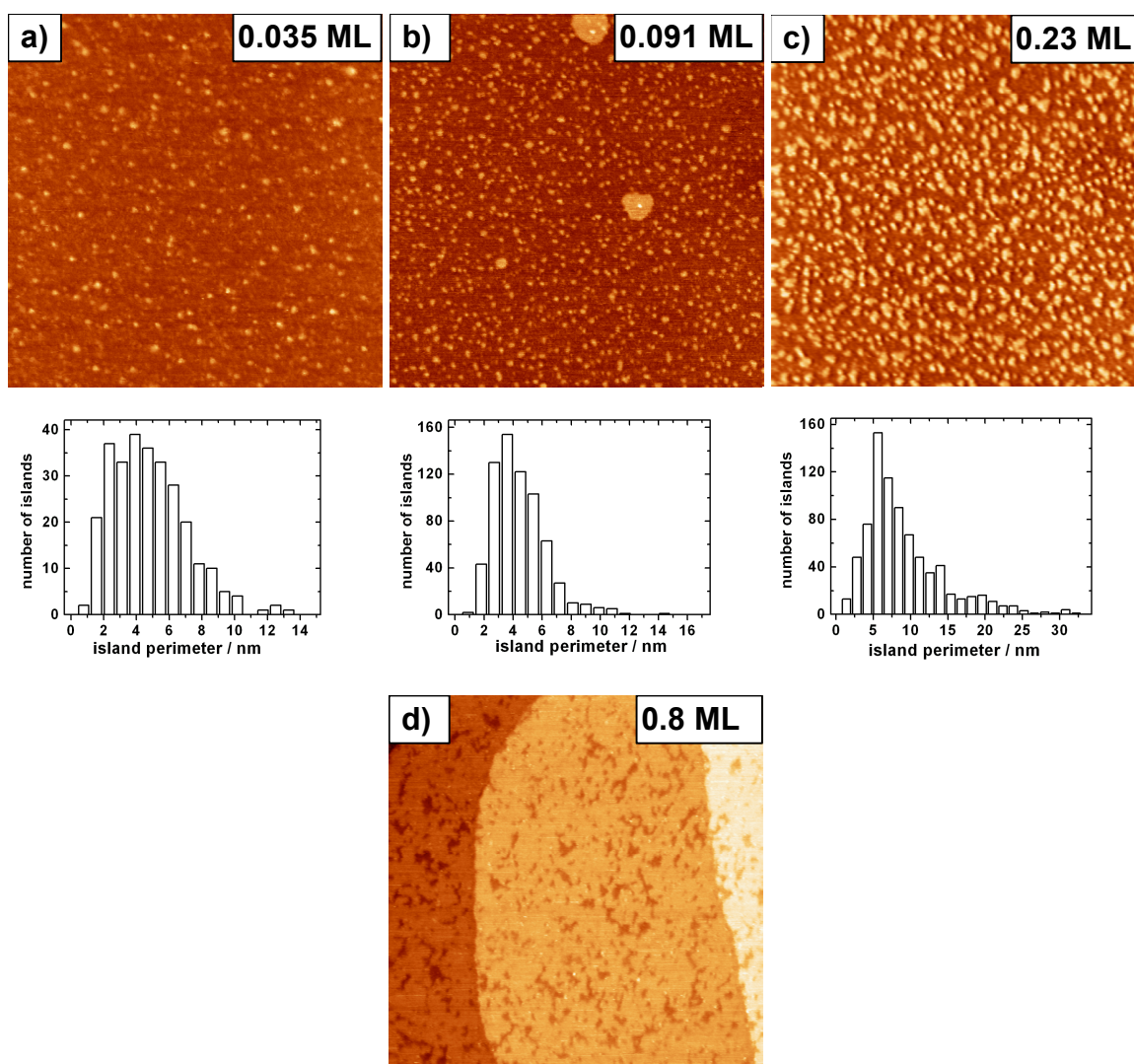
Fig.3.11: STM images of potentiostatic pulse deposited sub-MLs Pd onto Au(111) in 0.5 mM Pd(NO$_3$)$_2$ + 0.1 M HClO$_4$. For all images U$_{WE}$ = 0.95 V, U$_{tip}$ = 0.85 V, I$_{tip}$ = 1 nA and 150 x 150 nm size. The potential pulse height and the duration of the pulse were as follows: (a) -230 mV, 1 s; (b) -300 mV, 0.5 s; (c) -250 mV, 2 s and (d) -250 mV, 5 s. Below the first three images histograms of the islands perimeter distributions are shown. The Pd coverage deposited after the potential pulses is: (a) 0.035 ML; (b) 0.091 ML; (c) 0.23 ML and (d) 0.8 ML.

0.091 ML Pd on Au(111) deposited with a potential jump to 0.65 V for 0.5 s (Fig.3.11b). The island perimeter distribution was approximately the same like the first one, but the islands with perimeter about 4 nm were approximately by factor of 4 more. The total number of the islands on the image was 803. The third image shows 0.23 ML Pd on Au(111) deposited with a potential jump to 0.7 V for 2 s (Fig.3.11c). The maximum of the island perimeter distribution is around 5 nm, but the dispersion is approximately two times larger compared to the first two experiments. Due to the fact that the deposition time in the third case was longer (2 s) some of the islands merge and form larger islands, which increase the dispersion. The total number of the islands on third image was 789. The fourth image shows 0.8 ML Pd on Au(111) deposited with a potential jump to 0.7 V for 5 s (Fig.3.11d). Here the surface morphology is different from the previous three images. The surface is free of islands due to the long deposition time. The monoatomic islands grow progressively and gradually cover the whole Au(111) surface with almost a completed uniform Pd monolayer. About 20 percent from the surface is not covered with Pd. This results in monoatomically deep holes with different shape.

The experimental results confirms the theoretical expectations. When the applied potential pulse was large (values at larger overpotentials) the number of the deposited islands per unit area was larger as well. Such examples are the first and second image showed in Fig.3.11. Prolongation of the deposition time cause increase of the size of the islands, which merge and cover the surface with almost complete one monolayer (Fig.3.11d). By the use of the potential pulse technique the density of the islands per image area (150 x 150 nm) cannot reach numbers below 200. The lowest island density in the order of 100 islands per image area was reached by potentiostatic deposition at lower overpotentials. The nucleation by lower overpotentials is induced due to the surface defects and represents the lowest possible number of islands per surface area. By using potential pulses at higher overpotentials the island density per surface area can be increased up to one order of magnitude compared to the deposited islands by smaller overpotentials. Hence, by potential pulse technique sub-monolayers Pd on Au(111) with narrow size distribution and different island density per surface area can be deposited.

Chapter 4

Characterization of the Pd/Au(111) systems

In this chapter some results, which lead to the characterization of the deposited Pd monolayers and partial layers on Au(111) will be presented. The cyclic voltammetry of the samples in perchloric acid solution will be shown in the first section. In the second section the measurements performed with FTIR will argue the existence of adsorbed NO layers onto the deposited Pd layers. The last part will reveal the evaluation procedure and results obtained from the *in-situ* STM images of Pd sub-monolayers on Au(111).

4.1 Cyclic voltammetry measurements

4.1.1 Pd/Au(111) in 0.1 M HClO$_4$

Prior the reactivity measurements of Pd/Au(111) regarding hydrogen evolution reaction of the samples were characterized by cyclic voltammograms in order to achieve more structural information. The Pd multilayers, monolayers and fractions of monolayers were deposited in 0.1 M HClO$_4$ + 0.5 mM Pd(NO$_3$)$_2$ solution by potential sweeps.

Fig. 4.1 illustrates cyclic voltammograms of the Pd monolayers and sub-monolayers deposited onto Au(111) substrate with thickness of (a) 0; (b) 0.2; (c) 0.4; (d) 1; (e) 1.6;

(f) 2.4 and (g) 5 ML in 0.1 M HClO$_4$ solution. The current densities of sub-monolayers were calculated per Pd surface area and in case of coverage higher than one monolayer the geometrical areas were used. The potential was swept between 0.08 V and 1.18 V from 0.48 V initially in the negative direction by 50 mV/s. The cyclic voltammograms changed completely from the one of the bare Au(111) electrode when only 0.2 ML of the Pd was deposited on the Au(111) substrate. A cathodic current started to flow from ca. 0.35 V and a cathodic peak was observed at 0.2 V in the negative-going sweep. An oxidation peak was detected in the positive-going sweep at 0.22 V for coverage up to 1 ML. For a higher coverage the peak was shifted to more positive potentials. The redox peaks in this region were relatively broad. These redox peaks were not observed at Au(111) (Fig. 4.1(a)) and can be assigned to the hydrogen adsorption and desorption processes at the Pd monolayers and sub-monolayers deposited on the Au(111) substrate. Naohara *et al.* [31, 67] observe the same result for Pd monolayers and sub-monolayers in 0.1 M HClO$_4$, deposited by potential sweep from solution containing 1 mM PdCl$_4^{2-}$. Baldauf and Kolb [1] point out that the cathodic peaks because of hydrogen adsorption and absorption on the Pd thin layers were completely separated. This is possible due to a significant overpotential for hydrogen absorption on the Pd thin layers [1]. Subsequently, when the potential was swept to a more positive potential region, the anodic current started to flow from approximately 0.6 V with a peak at 1.06 V. This was not observed at the Au(111) electrode in the same potential region. The anodic current can be attributed to the oxide formation on the Pd surface. When the potential sweep was reversed to the negative direction, a cathodic current was observed with a peak at 0.73 V for a coverage up to two monolayers. In case of a coverage higher than two monolayers the position of the peak was at approximately 0.66 V. For a coverage between 1 ML and 2 ML both peaks were observed. Those cathodic currents can be assigned to the reduction of surface oxide on the Pd layer. The cathodic peak at 0.73 V can be attributed to the reduction of the Pd oxide from the first monolayer Pd on Au(111). As long as the first layer was not totally covered from the next Pd layers the cathodic peak at 0.73 V was observable. The oxide reduction peak was broader with an additional shoulder at more positive potentials for a coverage of 0.2 ML Pd/Au(111). The difference between 0.2 ML and 1 ML in the palladium oxide reduction peak can be explained by the different surface structure. With decreasing of the sub-monolayer coverage the ratio of Pd edge atoms increases with respect to Pd "bulk surface"

atoms. Quite possible is that the edge Pd atoms have different behavior regarding Pd oxide reduction compared to "bulk surface" atoms. The positions of the palladium oxide reduction peak indicate how strong the palladium oxide is formed on the surface. A decrease of the palladium coverage on Au(111) causes easier reduction of the surface oxide.
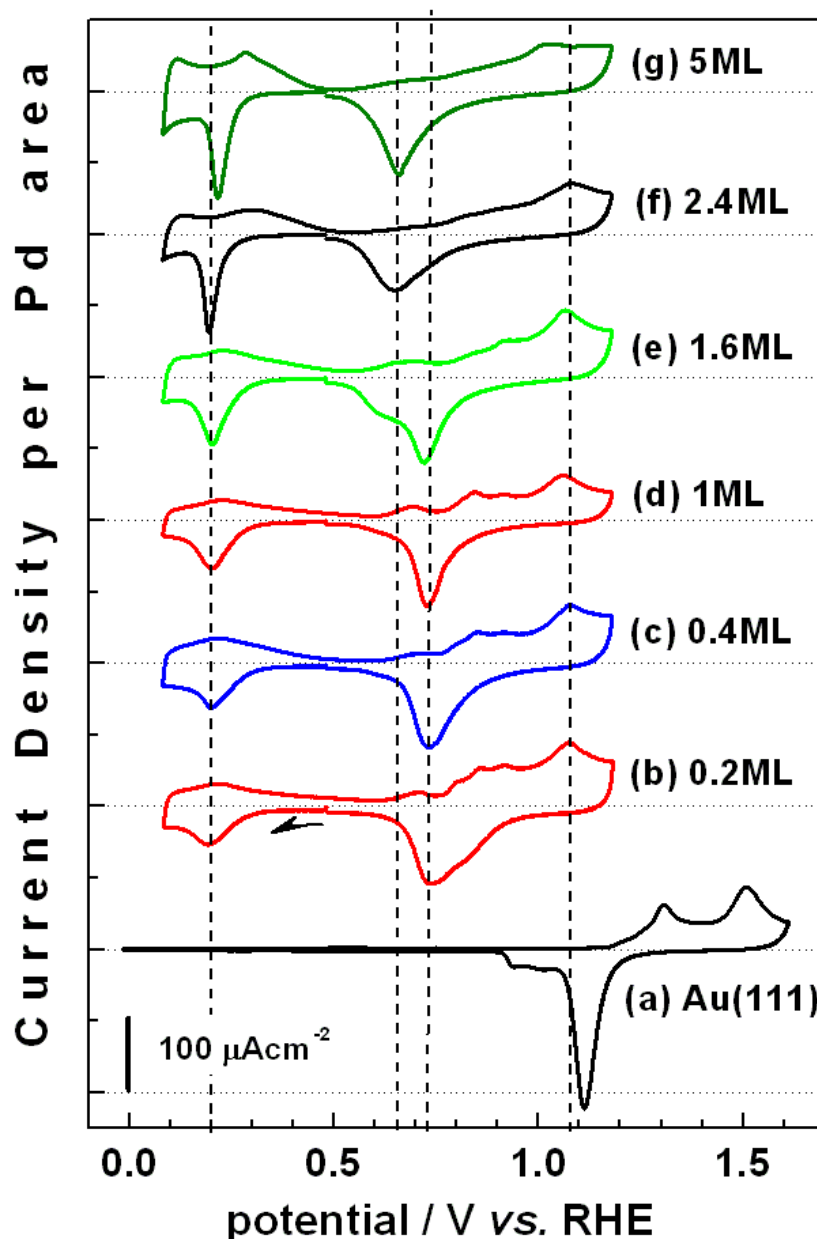

Fig.4.1: Cyclic voltammograms of Pd submonolayers and monolayers on an Au(111) substrate with a thickness of (a) 0; (b) 0.2; (c) 0.4; (d) 1; (e) 1.6; (f) 2.4 and (g) 5 ML, in 0.1 M HClO$_4$ solution. The potential was swept from 0.48 V to a negative potential by 50 mV/s. The layers are deposited by potential sweeps from 0.1 M HClO$_4$ + 0.5 mM Pd(NO$_3$)$_2$ solution.

In Table 4.1 the peak potentials, charges for hydrogen adsorption-desorption, and oxide formation-reduction of the CVs in Fig.4.1 are summarized. All the charges were calculated per Pd area. The charges for hydrogen adsorption on the surface of palladium monolayers and sub-monolayers were in the range of 0.21 mC cm^{-2}, as expected for the monolayer hydrogen adsorption on Pd(111) surface [1, 33]. In all measurements, the Pd oxide reduction charges were approximately the same and reached about 70-85 % of the charge (0.48 mC cm^2) corresponding to the monolayer oxide on Pd(111). This independence of the hydrogen adsorption charges from the palladium coverage proves that the growth mode was layer by layer. As the number of the Pd monolayers increased, the peak potential for hydrogen adsorption was shifted slightly to the positive region. Compared to the CVs of the Pd layers onto Au(111) in 0.1 M H$_2$SO$_4$ solution reported by Baldauf and Kolb [1], the peaks of the hydrogen adsorption–desorption in HClO$_4$ solution found in the present work were broader. As pointed out by Naohara *et al.* [8] the broader shape for the hydrogen desorption peak in HClO$_4$ solution compared to H$_2$SO$_4$ solution can be attributed to the weaker co-adsorption of the perchlorate anion as compared to the sulfate anion at the Pd thin layer surface.

The CVs of the Pd/Au(111) electrode can be used to determine the exact palladium coverage. As can been seen from Table 4.1 the charge for adsorption of monolayer hydrogen on Pd varied around 0.19 mC cm^{-2} and is connected to the Pd coverage. Therefore, this quantity may be used as a measure for monolayer Pd on Au(111). The usage of the hydrogen adsorption charge provided an easy determination of the sub-monolayers coverage.

Table 4.1 Peak potentials and charges of Pd /Au(111) in 0.1 M HClO4 solution. The charges per palladium area were indicated.

θ/ML	Hydrogen adsorption - desorption			Oxide formation - reduction		
	U(H$_{ads}$) V	U(H$_{des}$) V	Q(H$_{ads}$) mC cm^{-2}	U(O$_{ox}$) V	U(O$_{red}$) V	Q(O$_{red}$) mC cm^{-2}
0.2	0.19	0.22	0.18	1.074	0.73, 0.80	0.34
0.4	0.20	0.22	0.19	1.075	0.73	0.37
1	0.20	0.23	0.18	1.060	0.73	0.32
1.6	0.20	0.23	0.20	1.065	0.65, 0.72	0.41
2.4	0.19	0.30	0.21	1.080	0.65	0.31
5	0.21	0.28	0.23	1.100	0.66	0.36

4.1.2 Electrochemical behavior of the first and the second Pd monolayers

Fig.4.2 shows the CVs of 2.6 ML and 2.4 ML Pd on Au(111) in 0.1 M HClO$_4$ solution, deposited with potential jump and potential sweep, respectively. As was shown in the previous chapters the deposition of the second Pd layer needs a longer time compared to the first one. The deposition technique is very important for the morphology of the deposited Pd layers. The "slower" techniques give smoother surfaces [28]. The samples shown in Fig.4.2 should have approximately the same shape of the cyclic voltammograms. Nevertheless, the difference between both CVs is obvious. The sample deposited with the potential step technique show two Pd oxidation and two Pd reduction peaks. The Pd oxidation peak at 0.84 V is attributed to the formation of the oxide at the Pd step edges. Furthermore, the Pd oxide reduction peak at 0.73 V was observed at samples where the first monolayer was not completely covered from the next layers (see previous section). Hence, the surface morphology is proposed to consist of deposited 2D one monolayer Pd and 3D Pd islands on top. The position of the hydrogen adsorption and hydrogen desorption peaks of both samples are different. In the case of the sample with Pd deposited by potential pulse technique the hydrogen adsorption peak is shifted by 20 mV to a more positive potentials. A similar shift of the peak potential was observed for the sample with
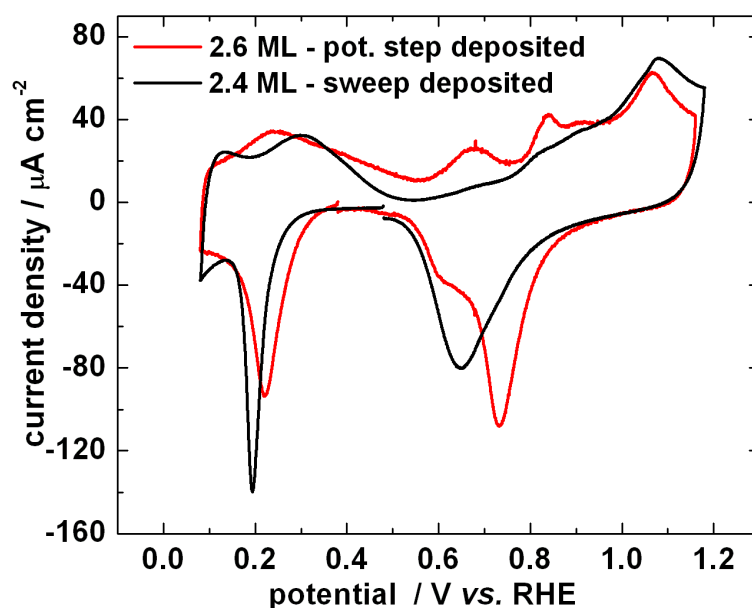

Fig.4.2: Cyclic voltammograms of 2.6 ML and 2.4 ML Pd on Au(111) in 0.1 M HClO$_4$ solution, deposited with potential jump and potential sweep, respectively. Sweep rate 50 mV/s.

5 ML Pd in the previous section. The hydrogen desorption peak of the sample with Pd deposited by the potential pulse technique was observed at 0.24 V. The same position of the peak was measured at samples with one monolayer Pd coverage. The electrochemical behavior of "potential pulse" deposited 2.6 ML Pd is a mixture between the behavior of one ML Pd and multilayers Pd on Au(111).

The sample with Pd deposited by a potential sweep reveals only one oxidation-reduction couple peak, which is assigned to the smoother surface and the completely covered first monolayer. Hence, the positions of the Pd oxidation-reduction peaks appear to be a good measure for the morphology of the first two layers. The existence of a shoulder or a peak for the Pd oxide reduction at 0.73 V reveals the existence of an uncovered first Pd monolayer. The anodic current peak at 0.84 V shows the quantity of the Pd step edges. The larger the peak is the amount of the edge atoms increase. For the reactivity measurements smoother samples were used with CV characteristics comparable to the sample with Pd deposited by a potential sweep.

4.1.3 Stability of the Pd deposits in perchloric acid solution

Cyclic voltammograms were taken before and after reactivity measurements in order to control the stability of the palladium monolayers and sub-monolayers during the measurements. The kinetics of the Pd dissolution in perchloric acid solution is remarkably slow, since Pd forms a quite stable oxide around already 0.9 V. In spite of that, repeated oxidation-reduction cycles lead to a gradual dissolution of palladium, as illustrated in Fig.4.2. The sample from Fig.4.3 was deposited in 0.1 M $HClO_4$ solution containing 0.5 mM $Pd(NO_3)_2$ by potential sweep from 0.84 V to 0.65 V with 50 mV/s sweep rate. In order to avoid further Pd deposition, the electrode was rinsed with ultrapure water and transferred to another electrochemical cell filled with 0.1 M $HClO_4$. At potentials more negative than 0.5 V, where no surface oxidation takes place, the cyclic voltammograms are quite stable. On the other hand, by increasing of the potential up to 1.28 V, the following oxide reduction leads to a slight decrease of the voltametric peaks. During each followed cycle the hydrogen adsorption peak and the oxide reduction peak decrease by several percent. After three cycles the charge density calculated from the hydrogen adsorption peak is 5 % less than the charge of the first cycle. The height and the shape of the anodic peak at 0.83 V remain constant during all three cycles. This anodic peak can be attributed

to the oxidation of the Pd edge atoms in the uncompleted (0.9 ML) monolayer Pd. Its stability can be explained by the higher initial surface roughness (for example see Fig.3.6), which cannot be changed considerably during the experiment. During every additional cycle the anodic peak at 1.06 V decreases. Furthermore, this oxidation peak can be assigned to the oxidation of the terrace Pd atoms. Therefore, after three oxidation-reduction cycles the number of Pd terrace atoms decreases. This is in good agreement with the oxidation-reduction experiments of one monolayer Pd on Au(111) in sulfuric acid solution pointed out by Kolb and coworkers [33]. The dissolution of Pd monolayer in sulfuric acid solution is faster compared to the one in perchloric acid solution. Kolb and coworkers reported [33], that after four oxidation-reduction cycles of 1 ML Pd in 0.1 M H_2SO_4, the Pd coverage dropped down from 1 ML to about 0.2 ML. They also pointed out, that the second Pd oxidation peak at higher potentials decreases with every followed cycle. On the other hand, they observed emerging of an additional Pd oxide peak at more negative potentials attributed to oxide formation at defects created by the cycling routine.
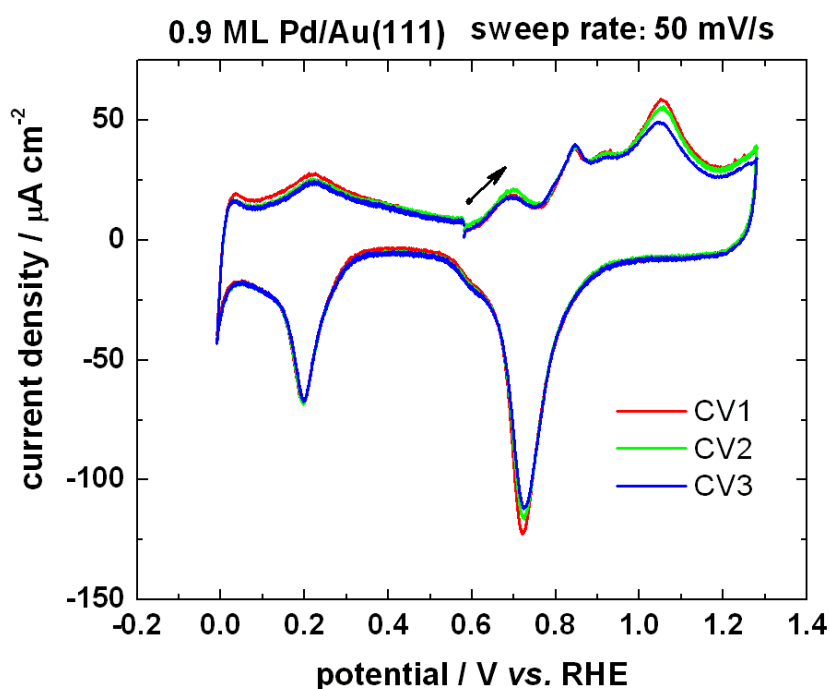

Fig.4.3: Cyclic voltammograms for Au(111) with 0.9 ML Pd in 0.1 M $HClO_4$ + 0.5 mM $Pd(NO_3)_2$. The changes from the first (red line) to second (green line) and third (blue line) Pd oxidation-reduction cycle represent the dissolution of Pd. Scan rate: 50 mV/s.

Furthermore, the stability of the deposited Pd layers or sub-monolayers was proved with CV in the potential range between 0.5 V and 0 V. Due to this set-up the dissolution of the deposited Pd was avoided. Such kind of CV was taken before and after each reactivity measurement in Chapter 5. If the measured currents in the CV differ from each other the reactivity measurement was not taken into account. However during most experiments, the CVs doesn't change. A potential difference could be a sign for poisoning of the surface by some contaminations. In such case the cell should be cleaned by using the entire cleaning procedure explained in the experimental part of this work.

4.1.4 Electrochemical reduction of the adsorbed NO on the Pd surface

Fig.4.4 shows the first 25 cyclic voltammograms of 1 ML Pd on Au(111) in 0.1 M $HClO_4$ solution. The potential was scanned between 0.58 V and − 0.01 V initially in the negative direction by 50 mV/s. As can be seen from the graph the first CV reveals no defined cathodic peak assigned to the hydrogen adsorption, as explained in the literature [1, 8, 33] . Only an increase of the cathodic current due to partial hydrogen adsorption plus hydrogen evolution was observed at potentials more negative than 0.15 V. An explanation is that the Pd surface is "passivated" from some adsorbed molecules, which hinder the hydrogen adsorption. The next section will show that those impurities were adsorbed NO molecules on the Pd layer, which originate from the deposition solution. In the second CV it is obvious that a shoulder emerged on top of the hydrogen evolution peak at approximately 0.05V. In each followed cycle the shoulder becomes more pronounced and shifts to more positive potentials. The increase of the cathodic charge in the second CV is around 7 % from the calculated cathodic charge in the first CV. Furthermore, in each followed cycle the increase of the cathodic charge decreases. So, at the final three CVs the hydrogen adsorption charge is already less than 1 %. The shape and the height of the hydrogen adsorption peak was stabilized after 25 cycles. The peak position was at approximately 0.18 V and the charge of the peak was calculated to 208 $\mu C \, cm^{-2}$. This is in good agreement with the charge for adsorption of 1 ML hydrogen on Pd (210 $\mu C \, cm^{-2}$ [33]). The cleaning of the surface became faster (smaller number of CVs before stabilizing the charge) when the lower limit of the CVs is shifted to more negative values. The above-

mentioned procedure was performed prior to every electrochemical measurement of the deposited Pd monolayers and submonolayers. The positive feature of the adsorbed NO is that the Pd surface is stabilized and protected from oxidation during the transfer from the cell filled with Pd containing solution to the cell filled with Pd free solution.
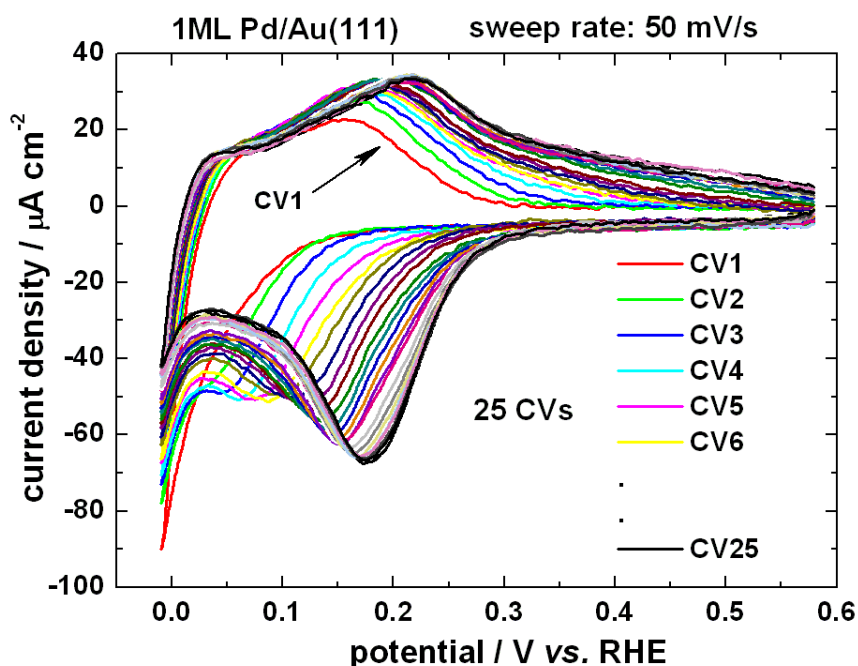
Fig.4.4: The first 25 cyclic voltammograms of 1 ML Pd on Au(111) in 0.1 M HClO$_4$ solution. The sweep rate: 50 mV/s. Prior to immersing the sample into Pd free solution the sample was rinsed in ultrapure water, in order to avoid further Pd deposition.

4.2. STM images of Pd sub-monolayers on Au(111) in perchloric acid solution

Fig.4.5 illustrates the sequence of STM images of 0.18 ML Pd on Au(111) in 0.1 M HClO$_4$ for an initial potential of 0.5 V. Fig 4.5a shows the observed surface after the transfer of the sample into the STM-cell. Well-defined monoatomic-high Pd islands are observed on the Au(111) surface. The Au(111) substrate surface was reconstructed. The blue lines in Fig.4.5 show the orientation of the observed reconstruction waves. The oxidation-reduction (OR) cycle was swept between 0.05 and 1.3 V from 0.5 V initially in the positive direction by 50 mV/s. Image (b) shows the surface after the oxidation-reduction cycle. One
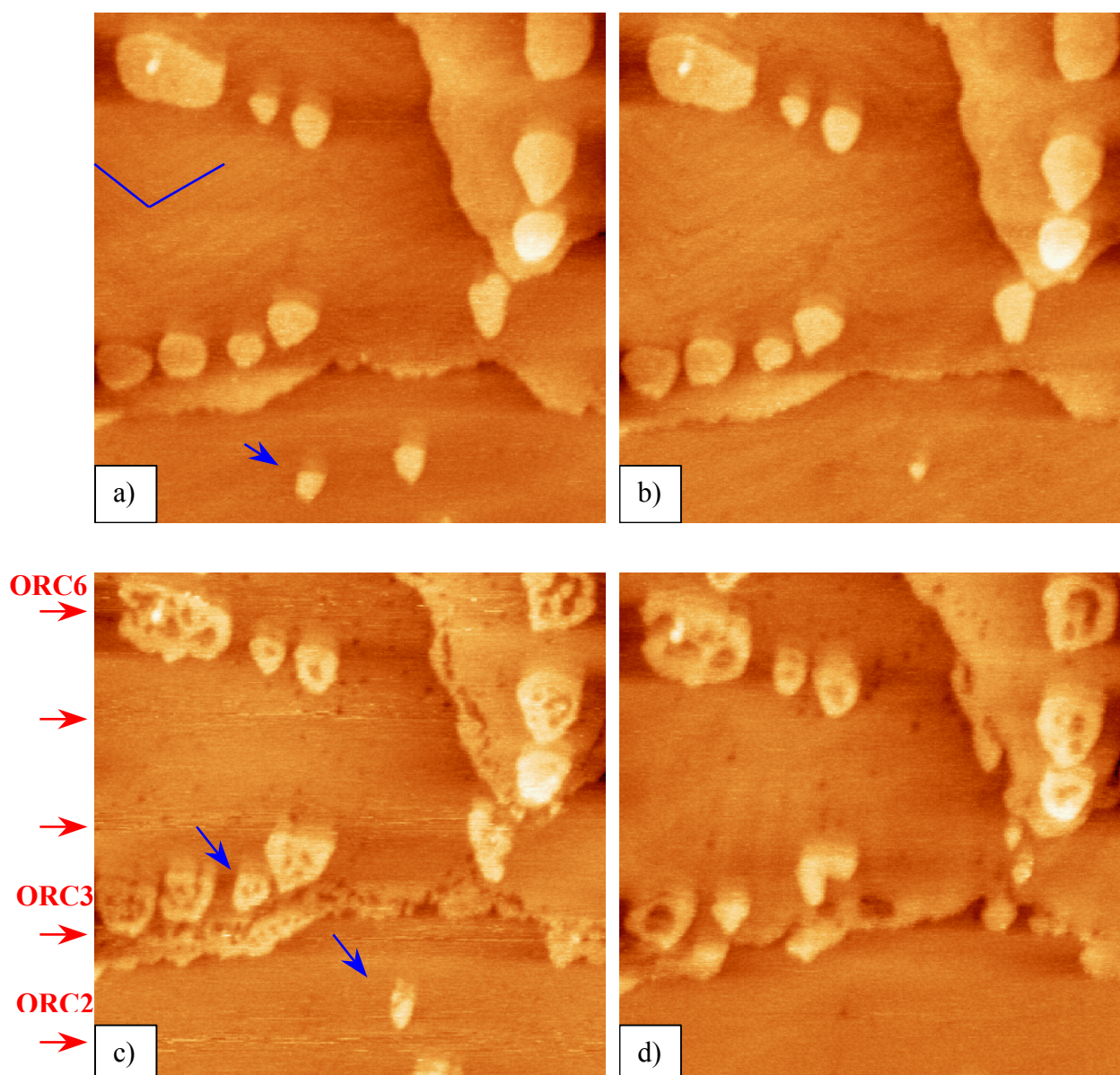
Fig.4.5: Sequence of STM images, showing 0.18 ML Pd in 0.1 M HClO$_4$. The imaging parameters were: U$_{WE}$ = 0.5 V; U$_{tip}$ = 0.4 V; I$_{tunel}$ = 1 nA; scan rate 650 nm/s and image size 150 x 150 nm. Image (a) is taken immediately after transferring the sample into the STM cell. The surface after one oxidation-reduction cycle (ORC) is shown in image (b). Image (c) shows the surface during the execution of other 5 ORC with the same parameters. Image (d) shows the surface after all 6 reduction oxidation cycles. The potential in ORC were scanned between 0.05 V and 1.3 V from 0.5 V initially in the positive direction by 50 mV/s. With blue arrows are shown some islands, which disappear in the next image. The red arrows show the position at which the potential reach its maximal value of 1.3 V. In image (a) the blue lines show the orientations of the reconstruction waves on the Au(111) substrate.

of the Pd islands was dissolved during the OR cycle. Fig.4.5c shows the electrode surface during further 5 OR cycles. The red arrows in the Fig.4.5 mark the area of the image where the potential reaches its maximal value of 1.3 V during the sweep. The monoatomic high Pd islands were covered with pits. The reason for this was a place exchange process during oxidation-reduction cycles. In addition, the monoatomic-high terrace steps were covered with pits as well. The upper potential limit was chosen so that only the Pd deposits were oxidized. Due to the selectivity of the method only the Pd surface was roughened. The surface after 6 OR cycles is shown in Fig.4.5d. The pits are already merged and form bigger regions. The Pd monoatomic islands are transformed into Pd monoatomic high "nano-rings". The reason for the formation of the Pd "nano-rings" is not quite clear. The properties of the edge atoms of the islands should have different electrochemical behavior compared to the inner terrace atoms of the islands. Possibly, the edge atoms have interatomic distance similar to the Pd bulk due to their weak interaction with the other atoms from the islands. The Pd atoms, which are in the inner part of the islands should have the lattice constant of the Au(111) substrate. The roughening of the Au(111) terrace step edges can be explained by the existence of additional Pd decoration of the steps, which may originate from the reconstruction of the Pd/Au(111) surface. Another explanation for the formation of the "nano-rings" is the possible bimetallic structure of the islands consisting of a Pd inner part and an Au outer part. The last one can be also formed after reconstruction of the surface.

4.3. FTIR spectroscopy

The "passivation" of the Pd surface was tediously attributed to the NO adsorption. Therefore, a proper measurement technique was required to verify this suggestion. A suitable technique is Fourier transformed infrared (FTIR) spectroscopy. After deposition of one Pd monolayer the sample was rinsed in ultrapure water and transferred in the FTIR electrochemical sell for further FTIR spectroscopy.

FTIR measurements were performed under external reflection conditions in a thin layer configuration. In order to obtain a single beam spectrum, 800 interferograms acquired at a spectral resolution of 4 cm^{-1} were added and then Fourier transformed. All spectra were

collected at 0.5 V to avoid an effect of the electrode potential on the NO stretching frequency (Stark effect). The "difference" IR adsorption spectra were calculated as a change of the reflectivity by using the equation [71]:

$$\frac{\Delta B}{B} \times 100\% = \frac{B_{n+1} - B_n}{B_n} \times 100\% \qquad (4.1)$$

Here B_n is the single beam spectrum acquired after the n-potential step and B_{n+1} is the single-beam spectrum acquired after the **n+1** step. This evaluation method seems similar to the one exploited in PDIR (potential difference infrared spectroscopy), their inherent difference being the fact that all spectra are collected at the same electrode potential (0.5 V). This evaluation method was used by Stimming and coworkers [71] by stepwise oxidation of CO on Pt nanoparticles.

Fig. 4.6 shows the difference spectra obtained after potential steps to defined electrode potentials. Spectrum 1 was evaluated after a prolonged step of 300 s at − 0.05 V. The ν N-O stretching frequency is expressed by a broad band at 1620 cm^{-1}. The positive sign of this band means that NO-groups were reduced in this potential step. No band was observed around 1460 cm^{-1}, typical for bridged-bonded NO. This means either that the NO coverage is very high (> 60 %) (Pt(111)-like) or that NO is bridged only linear to Pd (Pt(100)-like behavior). Rosca and Koper [71-73] reported that the NO saturation coverage on Pt(111) under electrochemical conditions is approximately 1 for experiments in perchloric acid. A negative-going band is seen at 1700cm^{-1}, which originates from the uncompensated water. To avoid this interference, measurements should be done in D_2O solution. Spectrum 2 was obtained again after a prolonged step of 300s at -0.05V. Obviously the major part of the NO was reduced in the first potential step. The red-shifted band in this spectrum, ν N-O = 1600 cm^{-1}, arises from a decrease in the dipole-dipole coupling due to the lower NO coverage. The final spectrum 3 after a step of 120s at 1 V obviously shows a re-oxidation of the former reduction products to NO. Because of the thin layer configuration of the cell the reduction products cannot easily leave the surface. Therefore they can be oxidized subsequently in the third potential step.

We note that the existence of the adsorbed NO on the Pd surface was proved with the FTIR experiment. The reduction of the NO can be realized by lowering the potential to slightly negative values, described in the previous section. The products of the NO reduction were

not characterized. Rosca and Koper suggest one possible mechanism of NO reduction on Pt with the overall reaction [71-73]:
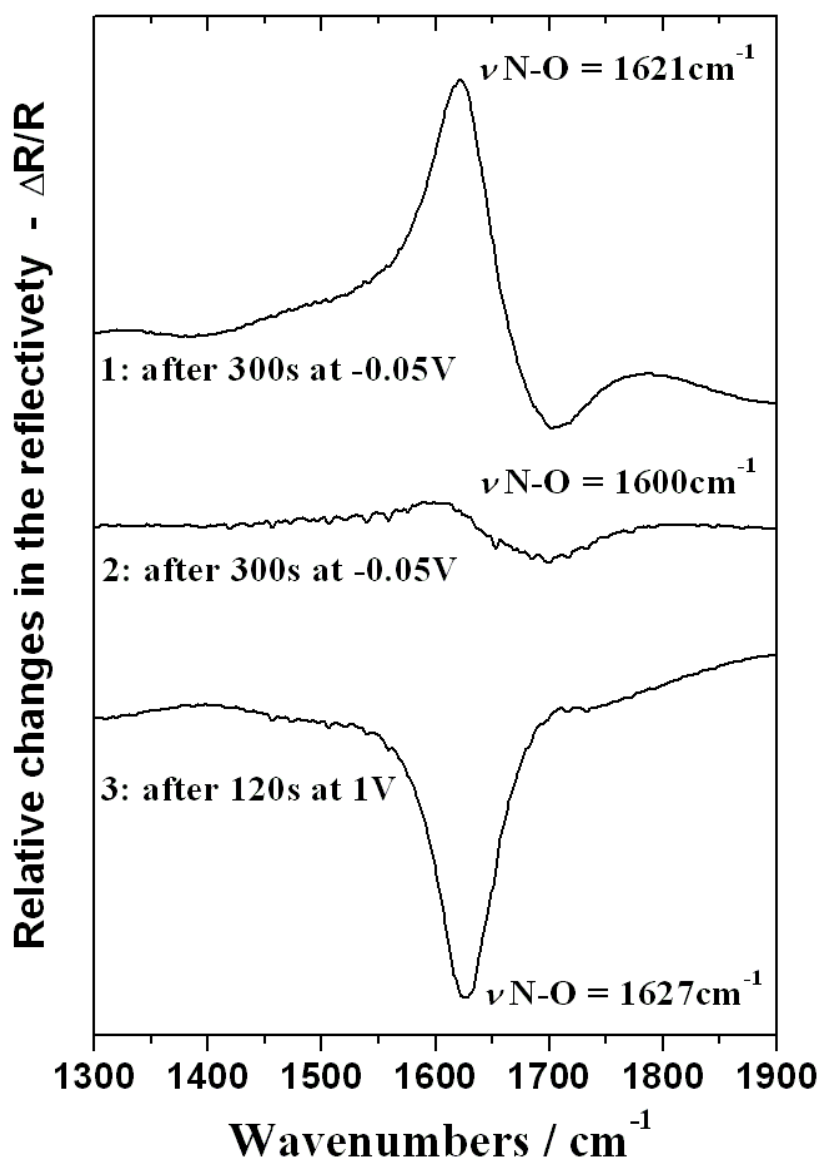
Fig.4.6: Difference spectra obtained under stepwise reduction and oxidation of NO. The spectra were evaluated by rationing the single beam FTIR spectrum acquired after n-potential step to the single-beam FTIR spectrum acquired after the n+1 step. The first and the second spectra were taken after a prolonged step of 300s at - 0.05V. The third spectrum was obtained after a prolonged step of 120s at 1V. All spectra were collected at 0.5 V vs RHE in 0.1 M $HClO_4$; T = 298 K.

$$NO_{ads} + 6H^+ + 5e^- + * \longrightarrow NH_4^+ + H_2O + 2 * \qquad (4.2)$$
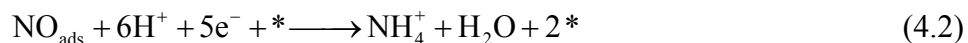
Furthermore, they deduced from the spectroscopic and electrochemical data, that ammonia is the main product of the reduction of adsorbed NO on Pt(111) and Pt(110). Van Veen and coworkers [74-77] pointed out that the transition metals show high selectivity of NO reduction toward NH_3 at low potentials. Moreover, they investigated that the NO adsorbate in the absence of NO in the solution is reduced to ammonia. Palladium has been reported as the best electrocatalyst for the above-presented reaction relative to all other transition metals.

4.4. STM images analysis

4.4.1 Evaluation of the morphology parameters

Herein the procedure for evaluation of the surface morphology parameters from the *in-situ* STM images of deposited Pd sub-monolayers on Au(111) is discussed. A very important point for the investigation of the reactivity of Pd sub-monolayers is the estimation of proper morphology parameters from the STM images. The evaluated parameters are; Pd coverage of Au(111), Pd island density per surface area, Pd island size (perimeter or diameter) distribution and the ratio Pd island edge atoms versus terrace atoms. The reactivity data can be characterized as a function of all these parameters. Thus, the influence of the edge atoms on the reactivity can be determined, which is an important task in electrocatalysis. The STM image consists of information concerning the height variations of the imaged area. Consequently, if the Au(111) surface with monoatomically high Pd islands should be characterized, then desired surface composition for the analysis will be the area of one monoatomically flat Au(111) terrace and Pd monoatomically high islands on the top of it. Therefore, images with only one monoatomically flat gold terrace were obtained for evaluation purposes.

Fig.4.7 represents the evaluation procedure for a STM image. Fig.4.7a illustrates an image containing only one Au(111) terrace with monoatomic high Pd islands, deposited with the potential pulse method (fore more details see Section 3.2.4 - Fig.3.11b). The Au(111) terrace is covered with monoatomic high Pd islands with diameter between 0.3 nm and
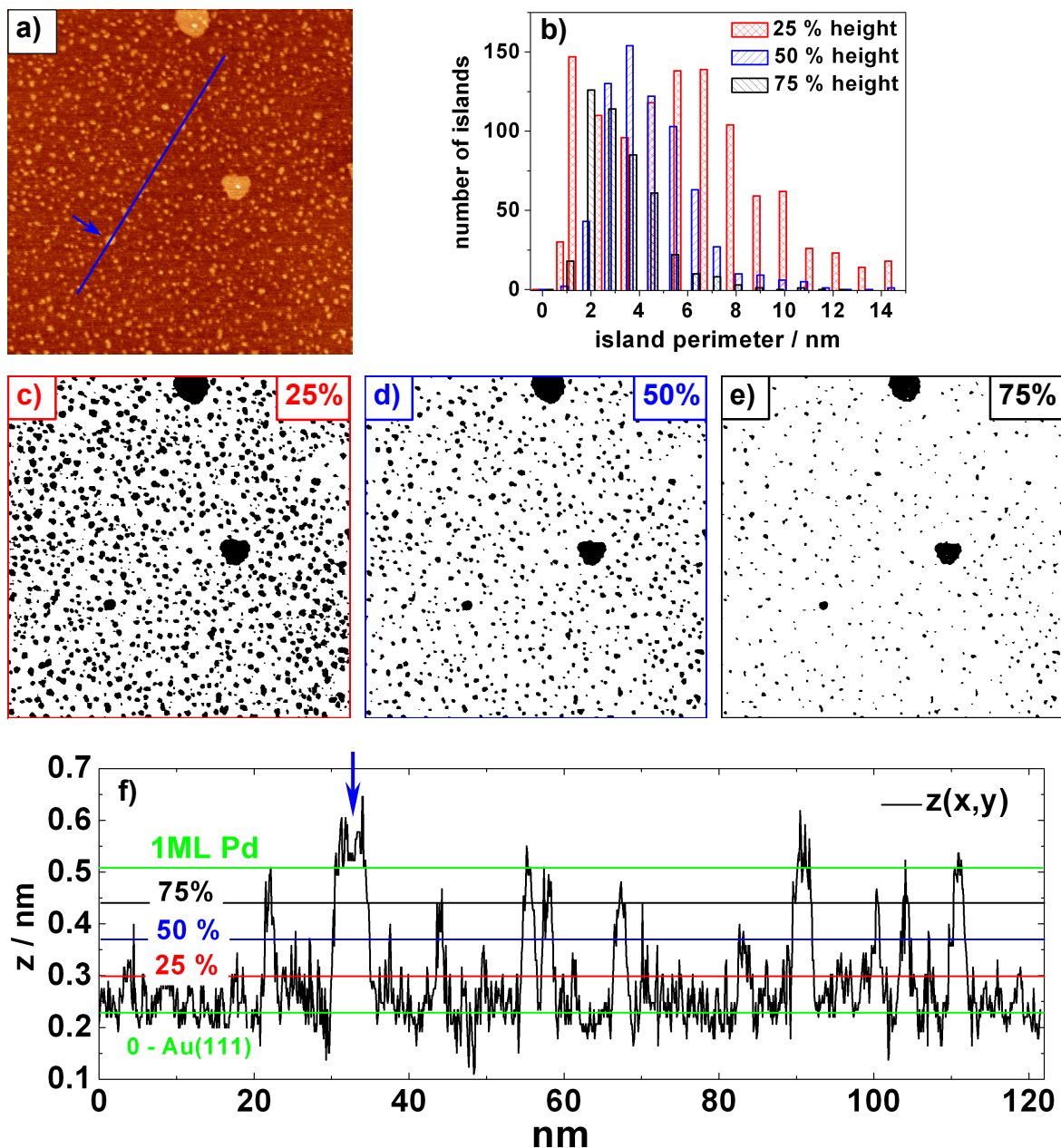
Fig.4.7: Analysis of the STM image 150x150nm. (a) STM image of potentiostatic pulse deposited 0.091 ML Pd on Au(111). (b) Island perimeter distribution as a function of the height (z-position) of the floating level. Floating level is the cross-section plane at defined height. The parts of the images below and over this level are colored with white and black, respectively. As an islands perimeter are taken the perimeters of every separate black "spot" on the images. (c), (d) and (e) resulting images with floating level 25 %, 50 % and 75 % from the height of 1 ML Pd on Au(111). (f) Z - cross-section profile of the marked part from (a). The arrow is for orientation. The additional plotted lines illustrate: the substrate Au(111) - zero level (green line), 0.25 ML (25 % - red line), 0.5 ML (50 % - blue line) , 0.75 ML (75 % - black line) and 1 ML height (green line).

5 nm. Due to the small size of the islands most of them were represented as a small gray point in the image. Like every real measurement the STM images were recorded with some level of noise. The last two facts were the reason to image Pd islands with height lower than one monoatomic height, which is in contradiction with the theory. The minimal height of each Pd deposit should be a monoatomic height. Furthermore, the image resolution can be improved by decreasing of the scan rate. However use of such way the mechanical drift of the surface will have significant influence on the imaging process. Thus, the shape of the island will appear to be distended compared to the real one. The best decision to avoid this is to find a proper scan rate where the influence of the mechanical drift and the image resolution are acceptable values. The z-profile of the image (Fig.4.7f) illustrates the above-mentioned facts. Obviously, some of the islands are below 1 ML height. Another parameter, which leads to a deviation of the imaged island morphology parameters from the real one, is the shape of the STM tip apex. As blunter the STM tip apex is as wider the imaged Pd island is compared to the real one. More information for the influence of the STM tip sharpness on the imaging of Pd islands is presented in [48]. Here the procedure used from the image evaluation software will be explained. So, the morphology parameters of the Pd covered area i.e. island perimeter distribution, total perimeter length and the total number of the islands per imaged area were evaluated by using the so-called "floating" level technique. The floating level is defined as a plane parallel to the lateral coordinates at a defined constant z- value. Thus, the STM image is divided into two parts, one with points below the floating height (colored with white) and one with points above the floating height (colored with black), respectively (Fig.4.7c-e). On this way, the resulting image consists of black spots on white background. The Pd area is calculated from the sum of all points above the floating level represented as area in nm^2. The rest area is attributed to the Au(111) substrate. The perimeter of each separate island is calculated as a sum of the distance between all island edge points. The distribution of all island perimeters is represented as a histogram. The total islands perimeter length is the sum of all single island perimeters. The total island number is the total number of all islands (black spots) in the resulting image.

Fig.4.7c, Fig.4.7f and Fig.4.7e show resulting images with different floating levels. The floating level is 25 %, 50 % and 75 % from 1 ML height for the first, second and third images, respectively. As zero point in the measurements comparable to the position of the

Table 4.2 The calculated morphology parameters from the image in Fig.4.7 at different floating levels.

Floating level ML height	Total perimeter μm	Coverage M ML	Total number of islands
25 %	7.18	0.179	976
50 %	4.29	0.091	803
75 %	2.12	0.042	502

floating level the surface of the Au(111) substrate is accepted. The calculated morphology parameters are presented in Table 4.2. As can be seen, a shift of the floating level close to the top of the islands cause decrease of all evaluated parameters. An explanation could be that some of the islands with lower height finds below the floating level and are not considered in the evaluation. Another reason is the measured shape of the Pd islands. The diameter measured close to the Au(111) substrate has a larger value compared to the diameter close to the top of the islands. The shape of the islands is conoidal like. The reason is the diameter of the STM tips apex and the ratio time of reaction of the z - piezo versus imaging scan speed.

4.4.2 The influence of the noise on the evaluated parameters

Fig. 4.8 shows the dependence of the calculated Pd area and total island perimeter as a function of the floating level. The morphology parameters were calculated from a row, one time smoothed and two times smoothed STM images. The smoothing filter makes the elimination of the high frequency components in the image possible. To do this, each point of the image is replaced with the average of its first neighboring point. Thus, every given matrix element f_{ij}, is replaced by a new value, d_{ij} given by:

$$\begin{pmatrix} f_{j+1,i+1} & f_{j+1,i} & f_{j+1,i-1} \\ f_{j,i+1} & f_{j,i} & f_{j,i-1} \\ f_{j-1,i+1} & f_{j-1,i} & f_{j-1,i-1} \end{pmatrix}, \qquad d_{ij} = \frac{1}{9}\left(\sum_{n=j-1}^{j+1} \sum_{m=i-1}^{i+1} f_{nm} \right) \qquad (4.3)$$

The image without any additional corrections is the co-called rough image. The calculated Pd coverage at different floating level heights is near the same for raw and smoothed images (Fig.4.8a). The dependence of the Pd coverage on the floating height is linear for
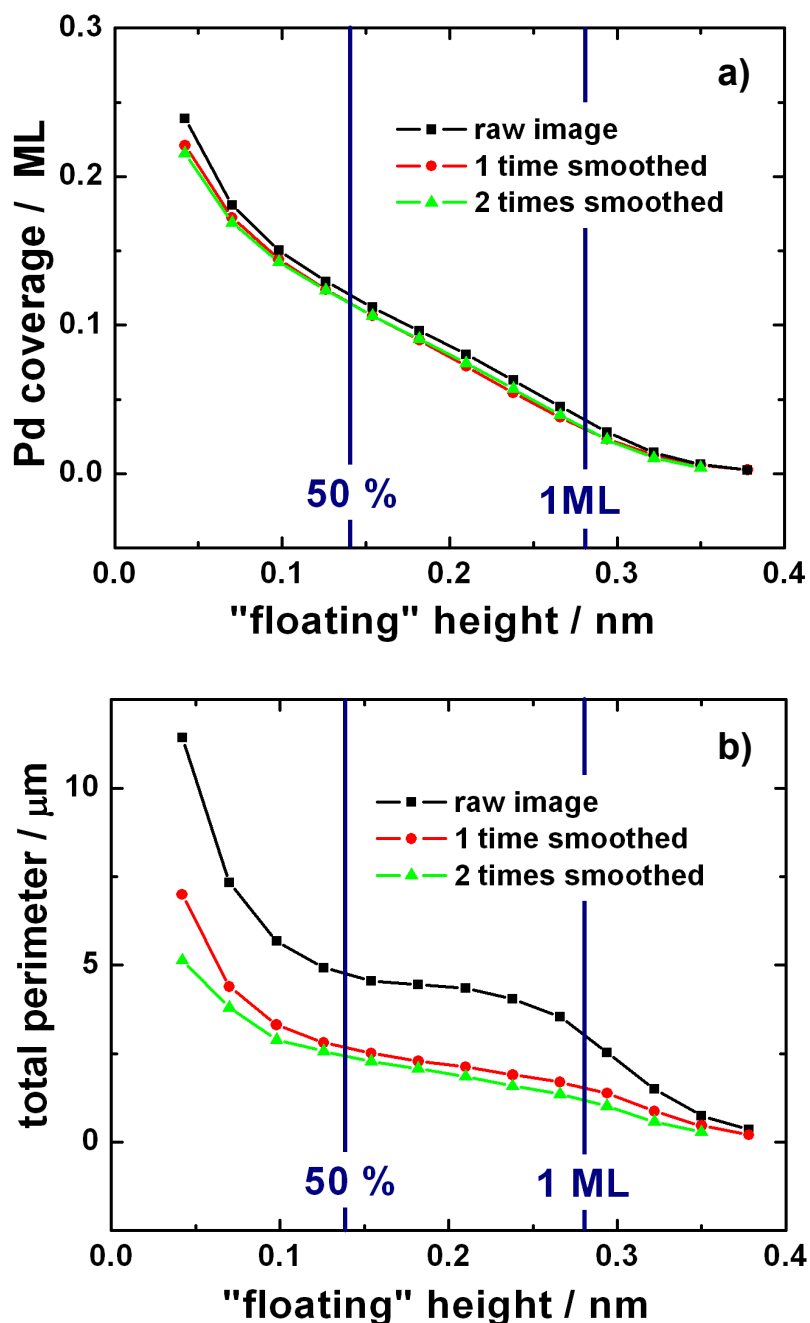

Fig.4.8: Morphology parameters evaluated from sub-monolayer Pd/Au(111) image as a function of the floating level height: (a) Pd coverage and (b) total Pd island perimeter. The raw image evaluations are presented with black color. The red and green color represents one and two times smoothed images, respectively.

heights between 0.4 ML and 1 ML. In the ideal case the coverage should be constant at all floating heights between 0 and 1 ML. The slope of the linear part of the plot is a measure of the STM tip sharpness. The smaller the slope the sharper is the STM tip. Below 0.1 nm height the coverage increases rapidly with decrease of the floating height. Because of the substrate surface at lower floating levels the "substrate" noise becomes significant and enhances the calculated Pd coverage. Further, the evaluated total islands perimeter lengths were different in the cases of smoothed and raw images. The total island perimeter length for raw image is around $2.5\,\mu m$ larger compared with the values for one and two times smoothed images (Fig.4.8b). The shape of the total island perimeter curve is similar to the shape of the Pd coverage curve.

The difference in the total island perimeter length between smoothed and raw image is due to the removed high frequency noise after smoothing. Fig.4.9 shows a sketch of the z-view of Pd island before and after smoothing, respectively. The raw image contains a high frequency noise originate from the acquisition electronics. This noise is removed after single smoothing process. Because of that the difference in the total perimeter length between raw and smoothed image is large (Fig4.8b). Further application of the smoothing process doesn't change the total perimeter length significantly. In case of evaluated Pd coverage from smoothed and raw image the difference was around one percent (Fig4.8a). The noise is recorded on the top of the real signal and it fluctuates around the true value.

The areas closed below the true value are approximately equal to the area closed over it (Fig.4.9). Thus in the evaluation procedure the both parts of the noise are neutralized and the calculated area represents the real one.

In the future evaluations of the morphology parameters only smoothed images should be taken in to account since their values are closer to the true ones.
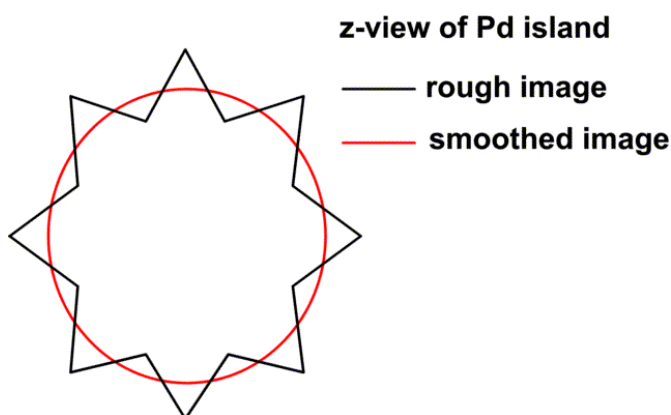

Fig.4.9: Z- view sketch of the shape of an island. The red and the black lines represent the smoothed island shape and the raw island shape, respectively.

4.4.3 Dependence of the ratio N_e/N_t on the mean island diameter

For the calculation of the number of edge and terrace atoms, the Pd coverage and the total island perimeter length were used. The number of Pd edge atoms in the investigated image was calculated from the total island perimeter length divided by the Pd interatomic distance of 0.27 nm. Analogously, the total number of Pd atoms in the image was estimated dividing the Pd coverage by the atom surface density (1.2×10^{15} atoms/cm^2). Consequently from the total number of Pd atoms the number of Pd edge atoms was subtracted, which gives the sum of all Pd terrace atoms. In Table 4.3 some of the morphology parameters evaluated for different samples are shown. The mean island diameter was calculated from the island perimeter distribution. Obviously with increase

Table 4.3 Morphology parameters of images with sub-monolayer Pd coverage.

Mean diameter nm	Floating level ML	Total perimeter μm	Coverage ML	Edge atoms N_e	Terrace atoms N_t	N_e/N_t
	0.25	7.24	0.16	19053	28539	0.67
1.84	0.50	4.72	0.10	12421	17324	0.72
	0.75	3.2	0.06	8474	8719	0.97
	0.25	9.9	0.38	26053	88168	0.30
2.87	0.50	7.8	0.23	20526	47887	0.43
	0.75	5.4	0.12	14211	21483	0.66
	0.25	6	0.27	15789	65712	0.24
4.3	0.50	4.4	0.18	11671	41870	0.28
	0.75	3.4	0.10	9068	20677	0.44
	0.25	4.3	0.17	11237	40519	0.27
4.6	0.50	2.7	0.11	7105	25614	0.28
	0.75	2.1	0.06	5526	12916	0.42
	0.25	2.8	0.11	7342	25377	0.29
5.8	0.50	1.9	0.08	4947	18849	0.26
	0.75	1.5	0.05	3921	10951	0.36
	0.25	6.3	0.45	16711	117141	0.14
7	0.50	5.6	0.34	14763	86965	0.17
	0.75	5.3	0.21	13842	48325	0.29

of the mean island diameter the ratio Pd edge/terrace decreases. Fig 4.10 shows the dependence of the ratio edge atoms/terrace atoms on the mean island diameter. For the calculation of the mean diameter a floating level with 50 % ML height was used. In addition, in the plot the ratios N_e/N_t calculated at 25 % and 75 % monolayer height of the floating level are shown, respectively. The data for the mean diameter are evaluated for different sample STM-tip couples. The difference between the values of the ratio N_e/N_t at 25 % and 75 % floating height is a measure for the sharpness of the STM tip. For the ideal or theoretical case the difference should be zero. Thus by controlling the island size diameter the ratio Pd edge atoms/terrace atoms can be regulated, which is an important parameter in the reactivity measurements.
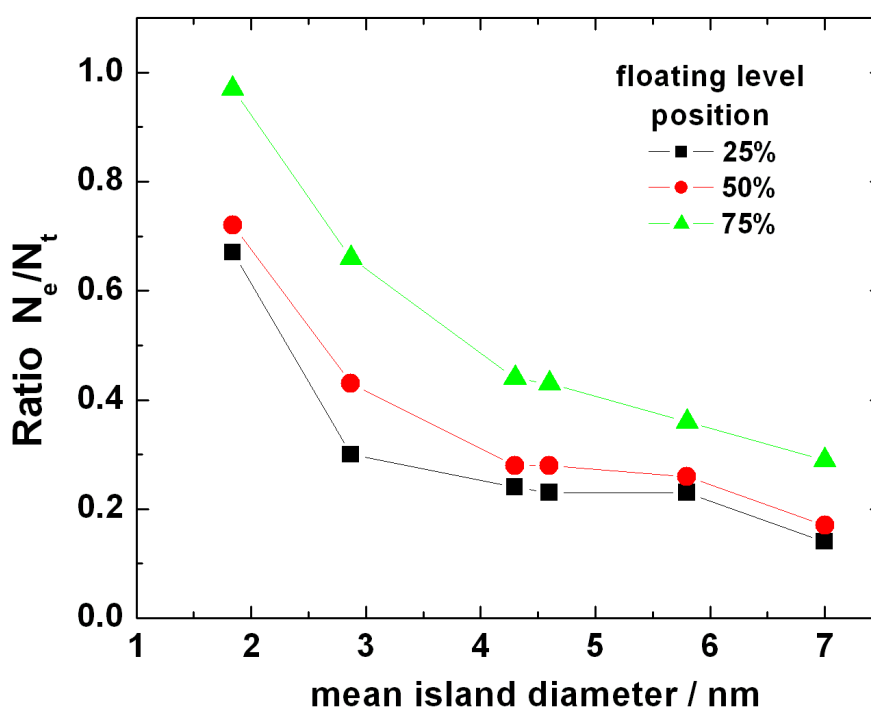

Fig.4.10: Ratio edge atoms/terrace atoms as a function of the mean island diameter calculated from the island perimeter distributions.

4.5 X-Ray Photoemission Spectroscopy investigations

Core-level spectroscopic characterization of Pd/Au(111) systems may give an insight into the extend of charge transfer and/or rehybridization that can occur in this system [17, 78,

79]. The XPS measurements were performed in a three-chamber set-up: electrochemical, exchange and analyzer chamber. In the electrochemical chamber on Au(111) signal crystals were deposited with various amounts of palladium from 0.25 to 20.5 ML. The amount of deposited palladium was determined by coulometric measurements. Fig.4.11 shows XPS core-level spectra of Pd(3d) and Au(4$d_{5/2}$) as a function of palladium coverage on Au(111). In all cases, the spectra were corrected for the secondary electron and the inelastic electron scattering background. At zero Pd coverage only Au(4$d_{5/2}$) core-level orbital was observed. The binding energy for this core-level is 334.73 eV and it is in agreement with the literature [80-88]. When the palladium coverage is increased, the palladium 3d doublet may alter the Au(111) binding energy spectra. The Palladium 3$d_{3/2}$ line emerges at a binding energy of 340.44 eV. The peak located around 335 eV in Fig.4.11 results from the overlap of Pd 3$d_{5/2}$ and Au 4$d_{5/2}$ lines. When the palladium coverage is increased the Pd 3d doublet intensity is also increased. The analysis of the XPS core-level spectra of 2.5 ML Pd/Au(111) is shown in Fig. 4.12. The fitting procedure uses
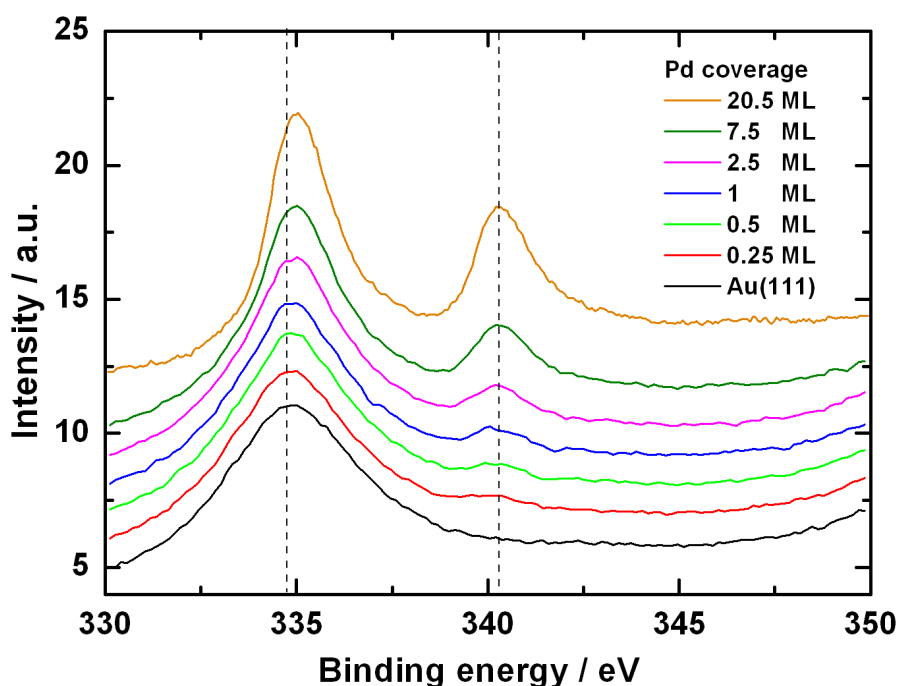

Fig.4.11: XPS spectra of Pd sub-monolayers and monolayers electrodeposited on Au(111) from 0.1 M HClO$_4$ + 0.5 mM Pd(NO$_3$)$_2$ solution. For bare gold only one peak attributed to Au 4d$_{5/2}$ line is observed. For higher Pd coverage additional peak Pd 3d$_{3/2}$ appears which increases with increasing coverage.

as constant parameters the binding energy of the Au $4d_{5/2}$ line, ΔE and the intensity ratio of the Pd-doublet. The difference between binding energies of both peaks in one doublet is defined as ΔE. Fitting parameters were the binding energy of the Pd doublet and the intensity of the Pd and Au d-lines. The reference XPS core-level spectrum of Pd(111) bulk was measured for comparison with the spectra of the Pd/Au(111) system. For bulk Au(111) and Pd(111) the measured d-lines were as follows:

Core-levels	-	Binding energy [eV]
Pd $3d_{5/2}$	-	**335.1**
Pd $3d_{3/2}$	-	**340.4**
Au $4d_{5/2}$	-	**334.7**

The XPS measurements show almost no shift (40 meV) of the d-lines of Pd monolayers on Au(111). The observed shift was in the range of the spatial resolution of the device.

In order to get better information of the surface structure the XPS spectra intensity ratio of
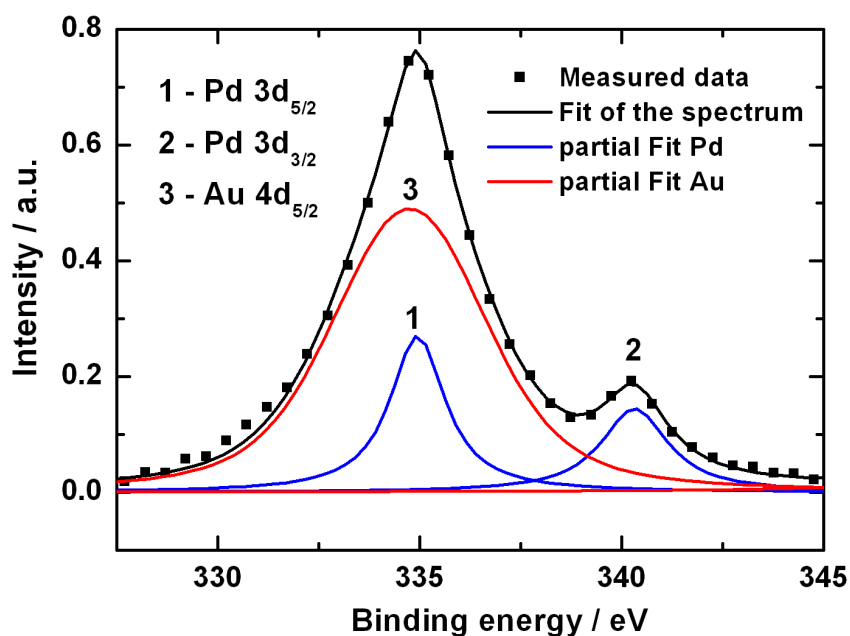
Fi.4.12: Fit of XPS spectrum for 2.5 ML Pd/Au(111). The blue lines are fitted Pd $3d$ core-levels and the red one is the fitted Au $4d$ core-level. Fitting parameters are E_b of Pd and intensity of Pd $3d$ and Au $4d$ core-levels. Constants are $\Delta E = E(Pd\ 3d_{3/2}) - E(Pd\ 3d_{5/2}) = 5.29$ eV, intensity ratio of Pd $3d$ duplet and the binding energy of Au $4d_{5/2}$.

Au *4d-* to Pd *3d-* lines versus number of palladium layers were investigated. Fig. 4.13 shows the experimental results for the intensity ratio of Au *4d-* to Pd *3d-* ($\Upsilon_{Au} / \Upsilon_{Pd}$) compared with calculated values from the semi-empirical equation for homogenous thickness of the layers.

$$\frac{\Upsilon_{Au}}{\Upsilon_{Pd}} = \frac{N_{Au}\lambda_{Au}}{N_{Pd}\lambda_{Pd}} \times \frac{\exp\left(-d/\lambda_{Pd}\right)}{1-\exp\left(-d/\lambda_{Pd}\right)} \quad , \text{ with } \lambda_{Au,Pd} = 0.054nm(eV)^{-\frac{1}{2}}\sqrt{E_{kin}} \qquad (4.4)$$

where $\Upsilon_{Au,Pd}$ is the XPS spectra intensity, $N_{Au,Pd}$ is the atom weight, $\lambda_{Au,Pd}$ is the free path length of the electrons, *d* is the thickness of the monolayers and E_{kin} is the kinetic energy of the electrons. The experimental results fit well with the calculated semi-empirical curve, except for coverage of 7.5 ML Pd/Au(111). This means that the Pd coverage is not homogeneous at larger numbers of deposited layers. The palladium deposition on Au(111)follows layer by layer growth for the first 2 layers. Therefore, the intensity ratio is in good agreement with the semi-empirical curve at lower Pd coverage.
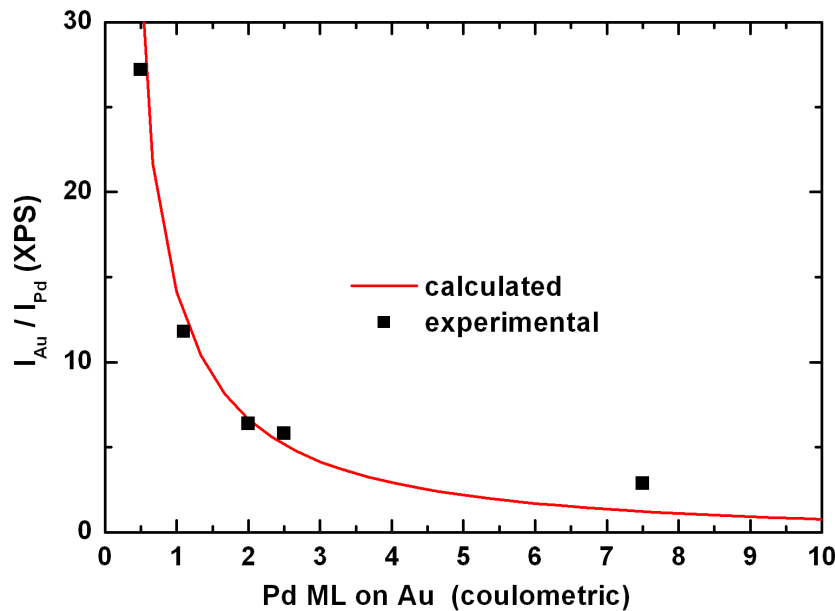

Fig.4.13: Intensity ratio I_{Au}/I_{Pd} (XPS) as a function of the number of the palladium layers on Au(111). The Pd coverage was determined from the coulometric measurements during the potential sweep deposition. The red line is calculated from the semi-empirical equation (4.4)

At higher palladium coverage the deviation from the semi-empirical curve is due to the rough surface formed from the three dimensional palladium growths. The above-mentioned conclusions for the morphology structure of the Pd deposits are the same as described in Chapter 3.

It is well known that the formation of a mixed-metal bond induces perturbations in the electronic properties of the bonded metals [89]. Theoretical calculations in the literature predict an up-shift of 0.35 eV for the d-band of 1 ML Pd deposited on Au(111) [17, 24, 25]. Several theoretical studies reveal that the variations in the center of gravity of the d-bands for metal overlayers are accompanied by similar variations in the surface core level shifts – at least towards the right in the transition metal series [90-92]. Scheffler and coworkers [92] show that the trends for the variations of the surface core level shifts for different overlayers are often given by the initial state shift. The initial state shift is defined by the changes in the electronic structure of the unperturbed surface. From this rule Hammer and Nørskov [17] concluded that the variation in the surface core level shift is a measure for the variation in the d-band center. This means that the surface core level shift represented an *in-situ* experimental measure for the position of the valence d-band center, which is important for the chemical properties of the metal surfaces. In this study a shift in the d-core levels of one monolayer Pd was not clearly seen in the range of the spatial resolution of the used XPS device. Surface alloys reveal a shift in the core level of $-0.2\,\mathrm{eV}$, which is in good agreement with the experiments results reported from Nascente *et al.* [82].

Chapter 5

Reactivity of Pd deposits on Au(111)

In this chapter the reactivity regarding hydrogen evolution reaction of Pd monolayers and monoatomic high nano-islands on Au(111) are discussed. In the first part the measurement technique is explained. The second part illustrates the reactivity measurements at the different Pd deposits. At the end of the chapter some physical model and possible explanation of the data are described.

5.1 Galvanostatic transient measurements

The reactivity measurements regarding hydrogen evolution reaction were performed using galvanostatic transients. Solutions of 0.1 M $HClO_4$ are used. Prior to the measurement the NO adlayer formed on top of the deposited Pd was reduced by cyclic voltammograms (see section 4.1.4). At the beginning of each set of experiments and afterwards, cyclic voltammograms were recorded in order to check the cleanliness of the solution and the electrode surface structure. The applied current was stepped down from zero to a defined value with a pulse duration of 60 ms. The pulse height was varied from -50 μA to -10 mA. Fig. 5.1 shows a sequence of applied current steps and the measured corresponding galvanostatic transients. Obviously, by increasing the current amplitude the corresponding potential measured after 60 ms decreases. The recorded galvanostatic transients show the same shape as presented in the literature [43, 45].
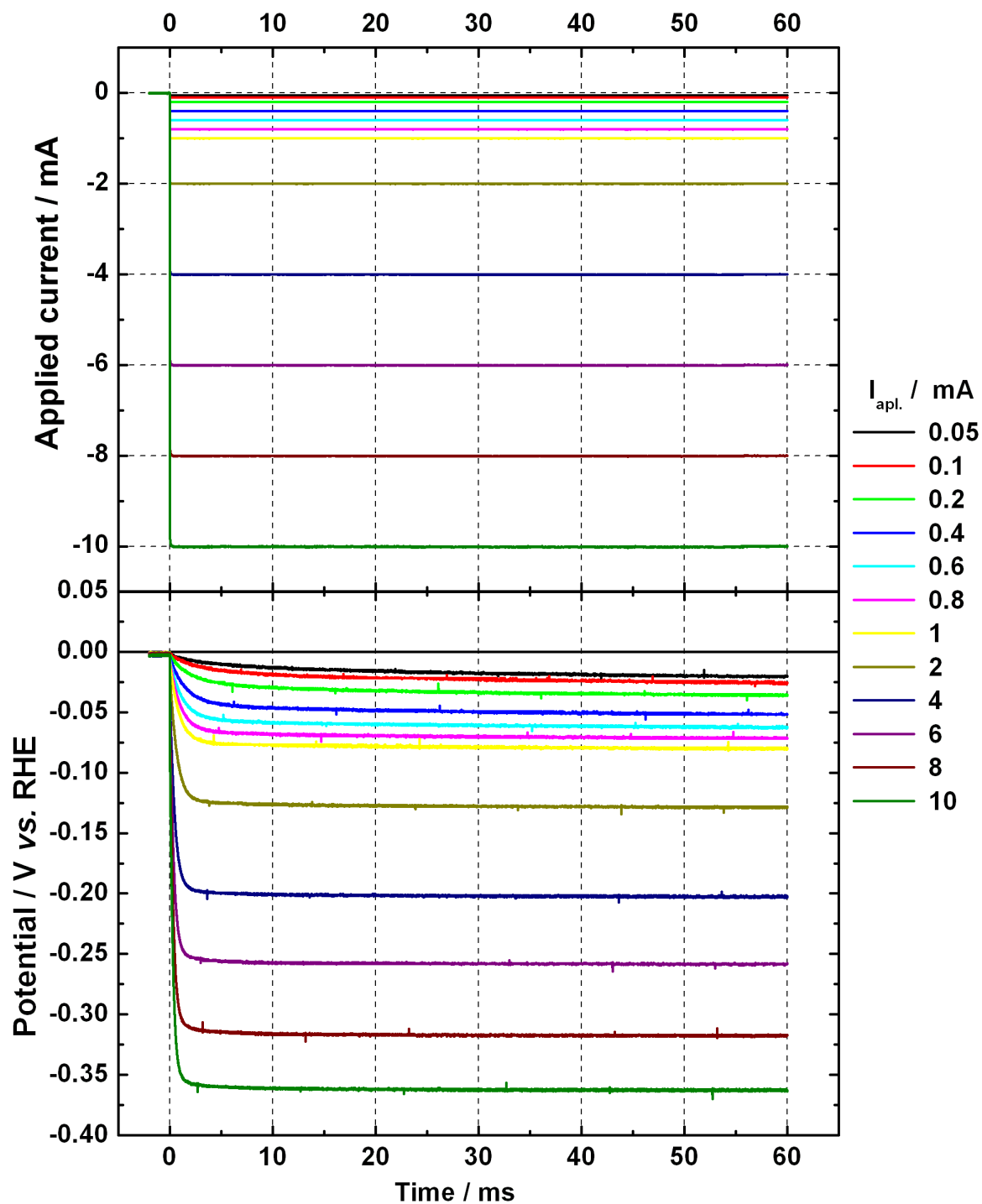
Fig.5.1: Sequence of applied current steps and the measured corresponding galvanostatic transients. The investigated sample corresponds to an evaluated Pd coverage 0.091 ML.

Immediately after the current jump the potential rapidly drops down, the drop (IR drop) originating from the electrolyte resistance (Fig.5.2). The decrease is subtracted from the measured potential after 60 ms. Fig.5.2 shows the applied current step and the measured potential transients on a shorter time scale. The current was stepped from 0 mA to − 8 mA. After the IR drop in the galvanostatic transient and before the steady state potential has established (Fig.5.1), two processes occur. The first one is the discharge of the double layer, which corresponds to the change in the potential. This process is dominant at the onset of the transient range. The second one is the electron passage across the double layer to ions on the solution side, dominant at later time of the mentioned range. The double layer discharging proceeds faster with an increase of the applied current amplitude (see Fig.5.1). The steady state potential of the transient is assumed as response of the applied current and used in the evaluations. Calculations verify that at the lowest applied current pulse the double layer is discharged after 20 ms, but the steady state potential is still not reached. Probably in this case the measured potential corresponds to different kinetics of the reaction. Thus, the Tafel plot at lower overpotentials can show a different slope than the evaluated one at higher overpotentials. This will be discussed in the next section.
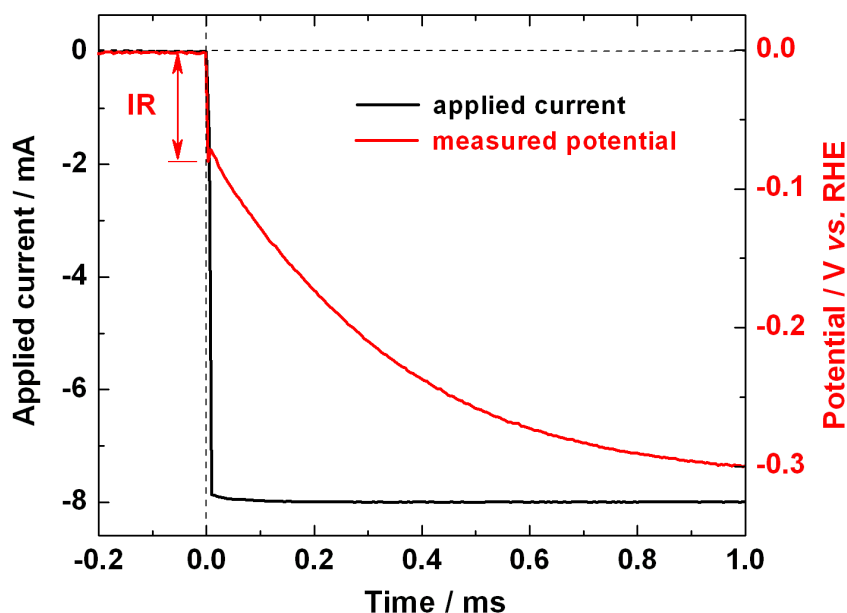

Fig.5.2: An applied current step of − 8 mA and the measured corresponding potential transient at 1 ms time scale. The evaluated Pd coverage of the sample is 0.091 ML.

5.2 Reactivity measurements on Pd layers and monoatomically high nano-islands in 0.1 M HClO₄ solution

The "final" steady state potential in the transient corresponds to the applied constant current. These values can be used for the evaluation of the Tafel plot. The exchange current density and the transfer coefficient (slope of the linear part of the plot) for the investigated electrochemical reaction can be easily determined by the Tafel plot. Fig.5.3 shows the Tafel plots of hydrogen reduction reaction for samples with different Pd coverage in 0.1 M HClO₄ solution. The upper and the lower graphs show the current density calculated per geometrical and palladium area, respectively. It is evident, that in both cases a decrease of the Pd coverage causes an increase of the current density. The slope of the linear parts of the Tafel plots for potentials lower than - 0.75 V is about 120 mV/dec and for higher potentials the value is between 40 mV/dec and 60 mV/dec. For lower potentials the slope is increased up to 180 mV/ dec. The various Tafel slopes at higher and lower potentials reveal different reaction kinetics. A possible explanation could be the different hydrogen coverage of the surface. The maximum possible hydrogen coverage can be calculated if one assumes that the complete applied current, except the current for the double layer charging, is consumed by the reaction. The calculated charge from the first four current pulses is below the charge needed for one monolayer (see Fig.5.1). Therefore, the change in the slope may be due to the different hydrogen coverage. The enhancement of the reactivity in case of monolayers is up to one order of magnitude. The increase of the reactivity for sub-monolayers is about four times higher compared to one monolayer Pd on Au(111). In addition, if the current density is calculated per Pd area the enhancement of the reactivity for sub-monolayers is stronger pronounced (Fig.5.3b). Thus, the revealed current density for sub-monolayers is about two orders of magnitude higher than for the completed Pd monolayer.

Fig. 5.4 shows the dependence of the current density per geometrical area (Fig.5.4a) and per Pd area (Fig.5.4b) as a function of the Pd coverage at potentials of -100 mV and -200 mV, respectively. Obviously the curve behavior can be separated into two parts for Pd coverage, below and above one monolayer. The enhancement of the reactivity in case of partial Pd coverage is stronger as compared to the reactivity of the multilayers. Reduction of the number of the Pd layers causes an increase of the current density. The

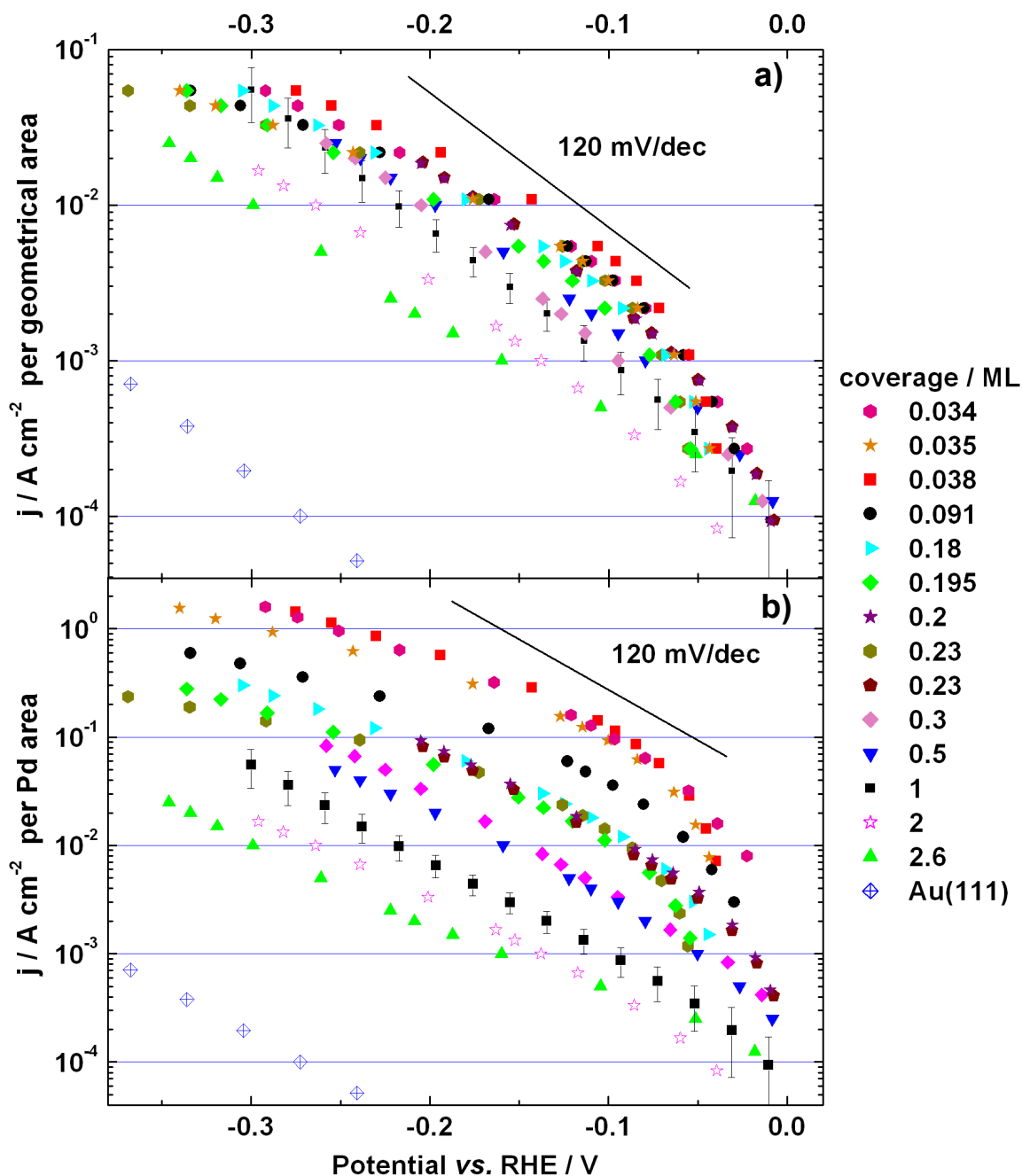**Fig.5.3:** Tafel plots of hydrogen reduction at sub-monolayers and monolayers Pd on Au(111). The data are measured in 0.1 M HClO$_4$ solutions by galvanostatic pulse measurements. The data for one monolayer palladium on Au(111) are the averaged data from five different samples. The current densities are calculated regarding: (a) geometrical area and (b) Pd area. The black lines are a guide for the eye with 120 mV/dec slope.

finding can be explained by the induced electronic effects of the strained lattice constants. The first deposited several Pd layers are characterized by an extended lattice constant. The first pseudomorphic monolayer Pd on Au(111) has a lattice constant extended by 4.8 % compared to the bulk Pd(111) surface. The last fact leads to a narrowing and upshift of the electrode d-band. This upshift of the Pd d-band becomes smaller increasing the number of Pd monolayers, tending towards the position of the d-band center of elemental Pd. In the d-band model, the upshift of the d-band center of metal surface atoms is proportional to the chemisorption strength [15-17]. If the rate determining step in hydrogen evolution reaction is hydrogen adsorption than the primary effect is the enhancement of the reactivity. The increased reactivity for sub-monolayers compared with one monolayer cannot be explained with the electronic effects because in both cases the Pd deposits display nearly the same lattice constant [22, 23, 93]. The influence of the partial coverage of Pd on the hydrogen evolution may be due to a catalytic effect of the edge-atoms at Pd-islands or due to a spillover-effect of intermediates onto the Au(111) surface. Thus, the parameters important for the electrocatalytical enhancement are still not clear. A possible parameter could be the Pd edge atoms/ terrace atoms ratio, which shows a reciprocal proportionality to the nano-island diameter. Other parameters could be the number of Pd edge atoms (N_e), terrace atoms (N_t) and the gold free area. The reactivity of the samples was investigated as a function of the respective morphology parameters. The partial Pd coverage was deposited in an electrochemical STM cell and characterized with *in-situ* images. Fig.5.5 shows the STM images of the Pd-islands on Au(111) in 0.5 mM Pd(NO$_3$)$_2$ + 0.1 M HClO$_4$. Histograms of the islands perimeter distributions are shown under each image. The evaluated Pd coverage and N_e/N_t ratio from the images are: (1) 0.035 ML, 0.55; (2) 0.091 ML, 0.72; (3) 0.18 ML, 0.28 and (4) 0.23 ML, 0.43, respectively. The used potential pulse deposition technique gives us the possibility to deposit samples with the same size distribution and different coverage (see Fig.5.5(1) and (2)). Therefore, the influence of the gold free surface can be investigated. Fig.5.6 shows the dependence of the current density as a function of N_e, N_t and ratio N_e/N_t at an overpotential of 200 mV. The left-hand side represents the current density per geometrical area (black points). On the right-hand side the current density per Pd area is indicated (red points). The calculated number of Pd edge atoms and terrace atoms belong to images with a size of 150 x 150 nm. No significant correlation between the current density and the ratio of edge atoms *vs.*
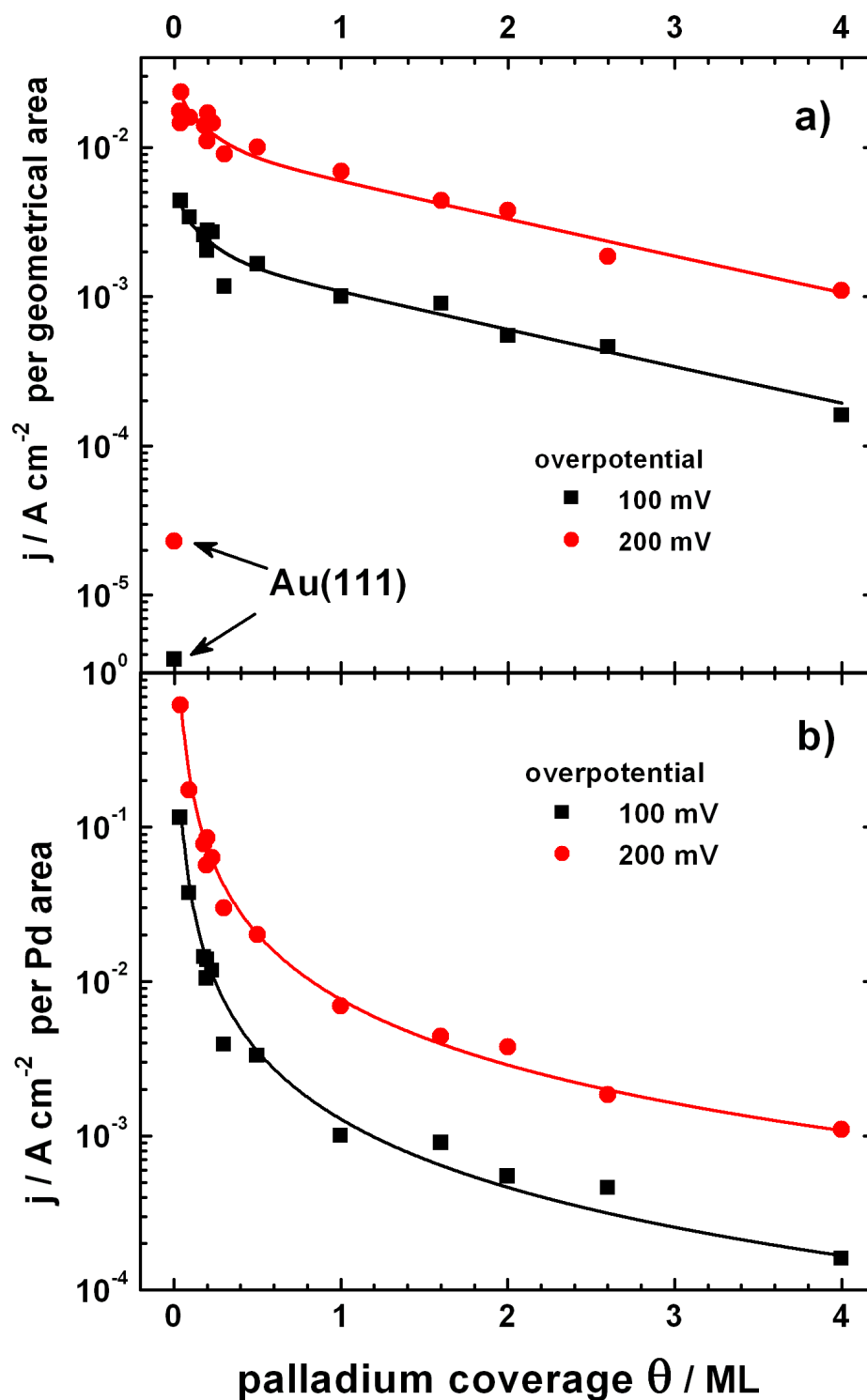
Fig.5.4: Current density of hydrogen reduction as a function of the Pd coverage at 100 mV and 200 mV overpotential, respectively. The current densities were calculated regarding: (a) geometrical area and (b) Pd area. The full symbols are the measured values and the solid curves are a guide for the eye.
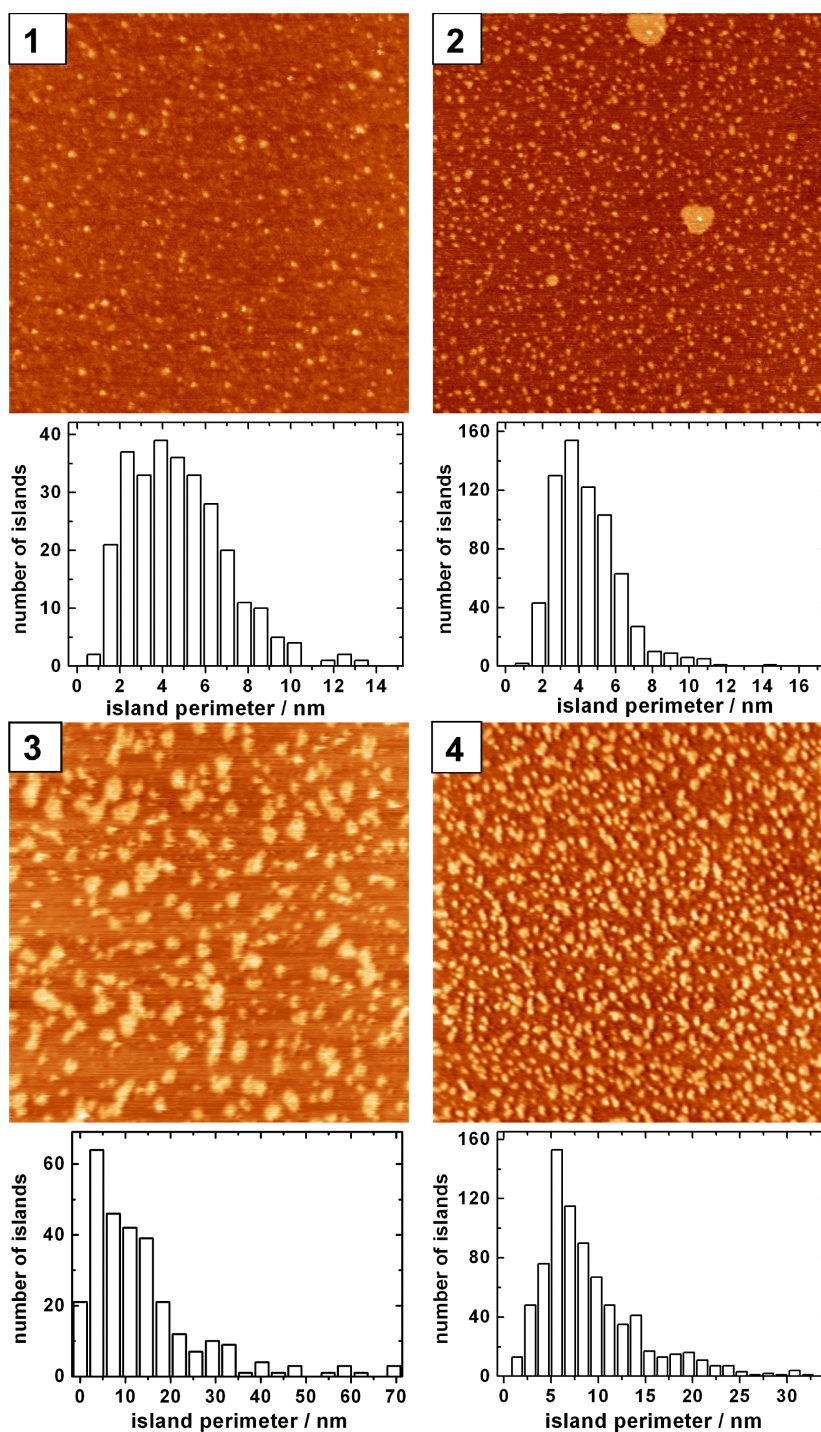
Fig.5.5: STM images of Pd islands onto Au(111) in 0.5 mM $Pd(NO_3)_2$ + 0.1 M $HClO_4$. For all images U_{WE} = 0.95 V, U_{tip} = 0.85 V, I_{tip} = 1 nA and 150x150 nm size. Below each image histograms of the islands perimeter distributions are shown. The evaluated Pd coverage and N_e/N_t ratio from the images are: (1) 0.035 ML, 0.55; (2) 0.091 ML, 0.72; (3) 0.18 ML, 0.28 and (4) 0.23 ML, 0.43.

terrace atoms seems to exist (Fig.5.6c). The same result was reported by Meyer *et al.* [47]. Furthermore, increasing the number of Pd edge atoms or the number of Pd terrace atoms the current density decreases in both cases (Fig.5.6a and b). The finding provide evidence that the catalytic effect of the Pd edge atoms is not particularly important for the hydrogen evolution reaction on Pd sub-monolayers on Au(111). Roudgar and Groß calculated the adsorption energy of hydrogen atoms with respect to the free H_2 and the corresponding *d*-band center positions of the supported Pd_3 and Pd_7 islands on Au(111) [93]. They found that on the Pd_3 islands the hydrogen adsorption energy is comparable or even stronger than on the Pd/Au(111) overlayer. On the other hand on the Pd_7 islands the hydrogen adsorption energy is significant smaller compared to the one on full Pd monolayer, but still larger
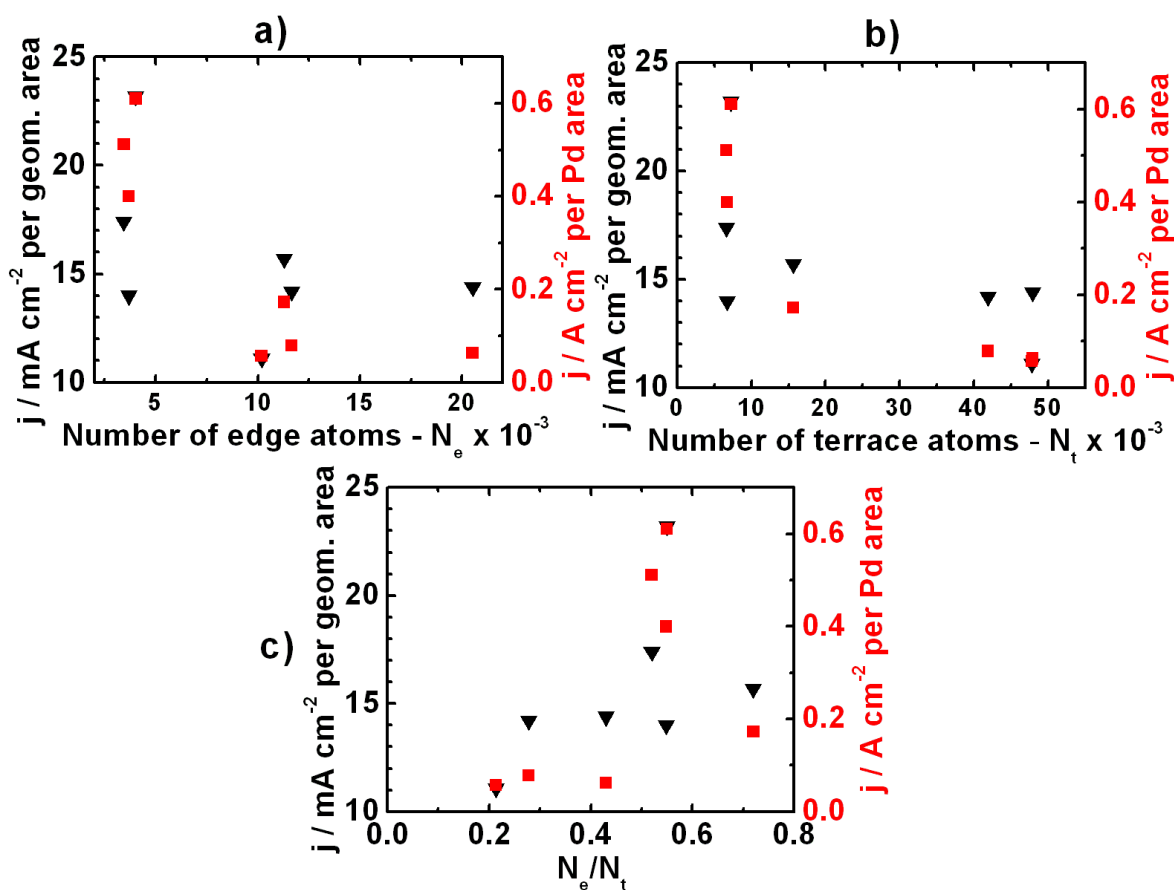
Fig.5.6: The dependence of the current density of hydrogen reduction at 200 mV overpotential on: (a) N_e – number of Pd edge atoms, (b) N_t – number of Pd terrace atoms and (c) ratio N_e/N_t, calculated from images with size 150 x 150 nm. The left and the right - hand sides indicate the current densities calculated per geometrical area (black points) and the current densities calculated per Pd area (red points), respectively.

than on the Pd(111) surface. The above mentioned facts show from an energetically point of view, that the reactivity of Pd nano-islands on Au(111) should reveal nearly the same reactivity per Pd surface like an extended Pd monolayer on Au(111). It is concluded that, the hydrogen adsorption energy is not the crucial parameter in the hydrogen evolution reaction kinetics on Pd nano-islands on Au(111).

Fig.5.7 shows the dependence of the current density at – 200 mV potential per geometrical area as a function of the free gold surface. Obviously an increase of the gold surface leads to an increase of the current density. The reaction rate of the hydrogen evolution reaction on Au(111) is about three orders of magnitude lower than that on a Pd(111) surface. Due to almost the same adsorption energy of hydrogen on Pd-islands and a single monolayer, the measured current density per Pd area should be equal. Thus, reducing the Pd sub-monolayer coverage will cause a decrease of the current density per total electrode area. The opposing findings suggest that the gold substrate could take part in the reaction path due to a spillover-effect of intermediates onto the Au(111) surface. The same phenomenon was considered in the kinetic model of Eikerling et al. [14] to explain the experimental results for the reactivity of single supported Pd nanoparticle on Au(111).

Fig.5.7: Current density of hydrogen evolution as a function of the free gold surface. The current density was calculated concerning the geometrical area in contact with the solution.

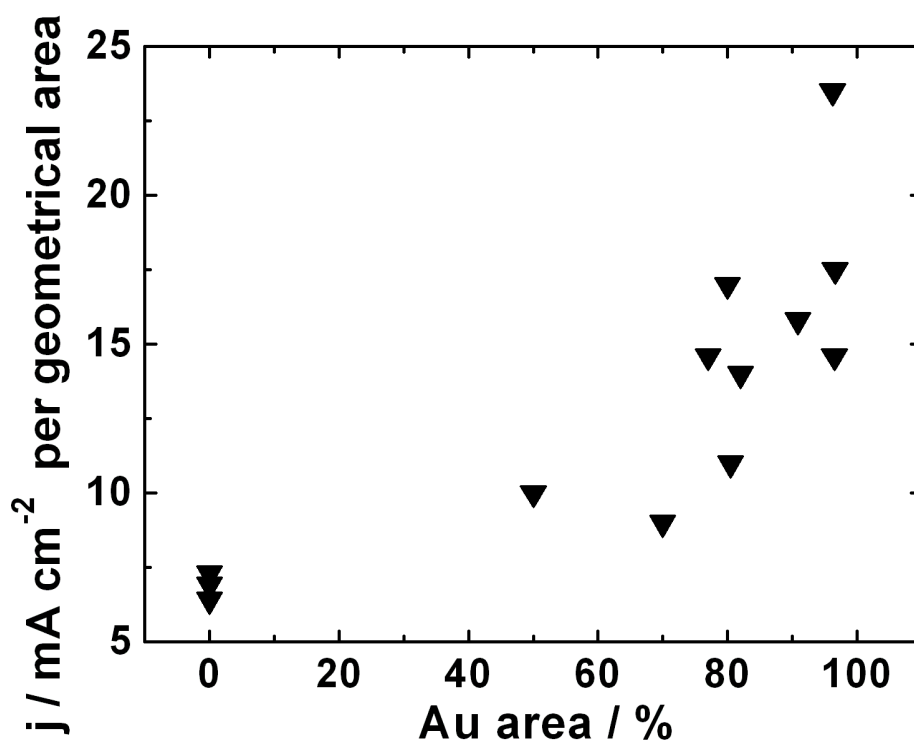The measured reactivity can be enhanced by different diffusion geometries in case of a full monolayer (planar diffusion) and in the case of Pd nano-islands on Au(111) (hemispherical diffusion). If the mean distance between two neighboring nano-islands is large enough the measured current can be expressed as the sum of the currents from all nano-islands represented as a single microelectrode with hemispherical diffusion [94-96]. Morf reported a theoretical treatment of the amperometric current response of multiple microelectrode arrays. It was shown that the total current output of multiple electrode configurations is lower than the response signal of macroelectrodes of the same total area [94-96]. Similar results were reported in numerous publications [97-102]. The measured current at Pd nano-islands on Au(111) should be smaller than that for one monolayer if only diffusion aspects are considered. Hydrogen solubility in aqueous solutions is typically $\sim 0.8 \times 10^{-3}$ mol dm^{-3} at 289 K and 1 atm of H_2 [100]. This saturated concentration is reached very fast after the beginning of the hydrogen evolution reaction, which means that it remains constant near the electrode surface during the measurements. Additional production of hydrogen molecules causes the generation of hydrogen bubbles. In both cases of hydrogen evolution at supported Pd nano-island on Au(111) and extended Pd surfaces the hydrogen diffusion from the surface will behave the same way due to the generated hydrogen bubbles. Because of the applied equal current pulses, the quantity of produced hydrogen bubbles at the surface is near the same for all experiments. Thus the diffusion current will be similar in all experiments.

5.3 Theoretical model of the Tafel plots

Due to the spillover effect the surface may be presented as an electrode where the hydrogen adsorption occurs only at the Pd nano-islands and the desorption is realized from the whole area. In this case the standard equations can be used. The hydrogen evolution reaction in acid solution follows two paths as follows: a primary discharge step (Volmer reaction)

$$M + H_3O^+ + e^- \underset{k_{-1}}{\overset{k_1}{\rightleftharpoons}} MH_{ads} + H_2O \qquad (5.1)$$
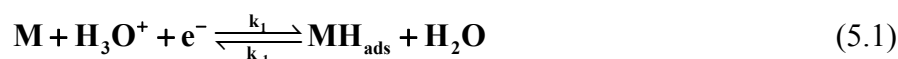
couples either with the electrochemical-desorption step (Heyrowsky reaction)

$$MH_{ads} + H_3O^+ + e^- \underset{k_{-2}}{\overset{k_2}{\rightleftharpoons}} M + H_2O + H_2 \qquad (5.2)$$
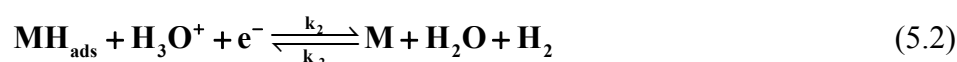
or the recombination step (Tafel reaction)

$$\mathbf{MH}_{ads} + \mathbf{MH}_{ads} \underset{k_{-3}}{\overset{k_3}{\rightleftharpoons}} 2\mathbf{M} + \mathbf{H}_2 \tag{5.3}$$

Here $\mathbf{M}$ is metal surface site. The overall reaction mechanism can be a combination of two [45] or all three [103, 104] steps. The steady-state condition for the material balance of the adsorbed intermediates for the reaction scheme described by Equations 1 to 3 is [46]:

$$\sigma \frac{d\theta}{dt} = 0 = V_1 - V_2 - 2V_3 \implies V_1 = V_2 + 2V_3 \tag{5.4}$$

where $\boldsymbol{\theta}$ is the surface coverage with $\mathbf{H}_{ads}$, $\boldsymbol{\sigma} = q_{max} / F$, q_{max} is the saturation charge and

$$V_1 = k_1 c_{H^+}(1-\theta)e^{\beta_1 f\eta}e^{-\beta_1 g\theta} - k_{-1}\theta e^{-(1-\beta_1)f\eta}e^{(1-\beta_1)g\theta} \tag{5.5}$$

$$V_2 = k_2 c_{H^+}\theta e^{\beta_2 f\eta}e^{\beta_2 g\theta} - k_{-2}(1-\theta)e^{-(1-\beta_2)f\eta}e^{-(1-\beta_2)g\theta} \tag{5.6}$$

$$V_3 = k_3\theta^2 e^{2g\theta} - k_{-3}(1-\theta)^2 e^{-2g\theta} \tag{5.7}$$

where $f = F / RT$ and c_{H^+} is the concentration of H^+ ions in the solution. In equations 5 to 7, V_i denotes to the reaction rates of equations 1 to 3, k_i represents to the rate constants for the steps noted above ($k_i = k_i^0 e^{\beta_i f\eta}$), $\boldsymbol{\eta}$ is the overpotential and $\boldsymbol{\beta}_1$ and $\boldsymbol{\beta}_2$ are the symmetry factors for the forward step of reactions (1) and (2), respectively. The parameter g in equations (5) to (7) refers to $\mathbf{RT}$ units, and indicates the change of the free energy of adsorption with coverage under Temkin conditions of adsorption [46, 105, 106]. The total faradaic current density, j, under steady-state conditions, based on material and charge balance conditions, can be expressed as [46]:

$$\frac{j}{F} = V_1 + V_2 = 2(V_2 + V_3) \tag{5.8}$$

It is suggested that the recombination (Tafel) and the electrochemical-desorption (Heyrowsky) steps are involved in parallel paths with the recombination step giving the greater contribution to the reaction rate at low surface coverage, while the electrochemical-desorption step becomes dominant at higher surface coverage. The total current density is expressed as:

$$\frac{j}{2F} = k_2 c_{H^+}\theta e^{\beta_2 f\eta}e^{\beta_2 g\theta} + k_3\theta^2 e^{2g\theta} \tag{5.9}$$

Assuming that the discharge step is in quasi-equilibrium, the surface coverage can be described as:

$$\frac{\theta}{1-\theta} = \frac{k_1}{k_{-1}} c_{H^+} e^{f\eta} e^{-g\theta} \tag{5.10}$$

where g is the repulsion parameter of a Temkin-type isotherm. Using these equations the experimental data of Tafel plots can be fitted. Fig.5.8a shows an example. The Tafel plot for 0.034 ML Pd on Au(111) in 0.1 M HClO$_4$ solution is shown (black points) and the corresponding fit based on the equation 5.9 (red curve). The hydrogen coverage θ, which were used in Eq.5.9 are shown in Fig 5.8b. Additionally, the maximum hydrogen coverage was calculated from the galvanostatic transients. The assumption that during the measure-
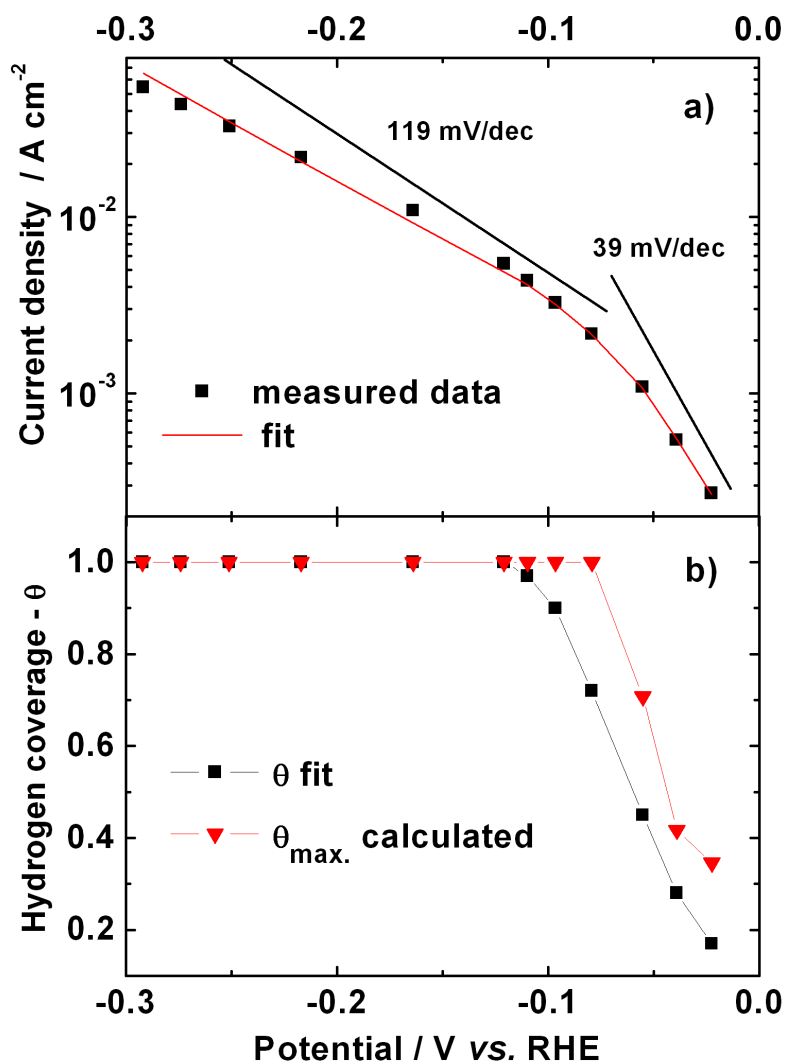
Fig.5.8: (a) Tafel plot of 0.034 ML Pd on Au(111) in 0.1 M HClO$_4$ solution and the corresponding fit based (red curve) on equation 5.9. The black lines are a guide for the eye. (b) The corresponding hydrogen coverage as a function of the potential. The black squares are the data used in the fit and the red triangles are the calculated data from the galvanostatic transients.

ment all adsorbed hydrogen remains at the surface was used in the calculation. Obviously the evaluated hydrogen coverage is higher than the used in the fit procedure. The reason is that some of the adsorbed hydrogen recombined and leave free surface sites. The used fit parameters are shown in Table 5.1. The extracted symmetry factor is 0.4, which corresponds to the Tafel slope of 150 mV/dec. Low values of β can be associated with the so-called activationless process [43, 107]. With a sufficiently negative shift in the potential, obtainable for fast electrode reactions, where diminution in β existed, and in the limiting case the activation energy is reduced to zero. After this state has been reached, no further increase in the reaction rate can be achieved by raising the cathodic potential. In such a situation a limiting current arises. This activation controlled limiting current must be distinguished by experiment from the normal one due to mass transport. The activationless state needs very high current densities and measurements times shorter than the transition times.

Table 5.1 Parameters extracted from the fit of the Tafel plot of Fig.5.8 using Eq.5.9

Parameter	β_2	k_2 (mol cm^{-2}s^{-1})	k_3 (mol cm^{-2}s^{-1})	g (-)
Value	0.4	5.2×10^{-5}	1×10^{-8}	2.3

Discussion

The significance of the spillover effect for the reaction kinetics of nanometer supported particles was discussed in [108]. Generally this effect in the heterogeneous catalysis is discussed in many reports in the literature [108-113]. The influence of hydrogen spillover on the conductivity of polycrystalline platinum-containing (in comparison to platinum-free) titanium samples was investigated by Roland *et al.* [111]. The increase of the conductivity was explained by the spillover of hydrogen from Pt to TiO_2. It was found that spillover and surface diffusion exhibit a considerable effect on the apparent reactivity of supported Pt particles. Vayssilov et. al. [113] report, that according to the model calculations, reverse spillover of hydrogen onto the zeolite-supported metal clusters is energetically favored for all investigated metals from groups 8 to 11 of the chemical periodic table.

As was shown in the present work the reactivity of sub-monolayers Pd on Au(111) is enhanced compared to one completed Pd monolayer. The measured current at sub-monolayers is about three times higher. In section 5.2 it was shown that the Pd edge atoms and the diffusion geometry do not enhance the reactivity. Now some arguments about the spillover of hydrogen from Pd to the Au(111) substrate will be discussed. First it was accepted that the hydrogen adsorption energy on nano-islands and Pd monolayer is nearly the same. For this reason the hydrogen adsorption and desorption rates per Pd area for nano-islands and monolayer should be similar. The reactivity measurements are always performed with the same sequence of current pulses. Therefore, the current density flowing thought the Pd nano-islands would be higher compared to that for one monolayer. It was assumed that the main current pass through the Pd area and the negligible rest current passes through the gold area. Consequently the Pd nano-islands should reveal for the same current pulse a higher hydrogen coverage compared to a Pd monolayer. This means that the measured potential transients for nano-islands should reach the steady state at lower currents and shorter times. The last point suggests that the Tafel plot in the case of nano-islands should display only one slope characterized by a higher hydrogen coverage. Furthermore the recombination and desorption of the adsorbed hydrogen should determine the overall reaction rate (rate determining step). Instead of that, two slopes of the Tafel

slopes of Pd nano-islands are observed. The same behaviour of the Tafel plot is also found for a complete Pd monolayer. Hence one can conclude that the same quantity of hydrogen is needed to achieve equal hydrogen coverage at the Pd deposits in both cases for Pd nano-islands and Pd monolayer. The last fact brings to mind that the hydrogen from the nano-island can spillover onto the Au(111) surface and increase the free sites of the electrode surface. The hydrogen spillover explains quite well the enhancement of the reactivity of nano-islands compared to one monolayer of Pd. Furthermore this effect can explain the experimental results obtained from other groups. Kibler reported [5, 6] that the reactivity of the hydrogen evolution reaction of a Pd sub-monolayer on Au(111) in 0.1 M H_2SO_4 is higher compared to that of a monolayer of Pd. Due to the spillover the whole surface of the electrode will take part in the reaction path. The adsorption of the hydrogen will occur only at the Pd nano-islands and desorption at the whole electrode. Usually the desorption rates are typically $< 10^3$ s^{-1} [114]. The adsorption rates of hydrogen on Pd nanoparticle are three orders of magnitude higher [13, 14]. Su and Wu investigated the spillover of hydrogen from Nafion to Au at negative potentials [115]. They showed that the opd hydrogen atoms could diffuse quickly on the Au surface and the average value of their surface diffusion coefficient is about 1.47 x 10^{-3} cm s^{-1}. The last facts indicate that the diffusion front of the adsorbed hydrogen will spread rapidly on the Au(111) surface due to the spillover effect. Furthermore low Pd coverage can supply hydrogen for the whole surface. The best Pd/Au(111) electrode geometry will be about 0.1 percent Pd coverage.

Fig.D.1 illustrates the processes involved in the reduction of protons at monoatomically high nano-islands of Pd: (1) bulk diffusion of protons, (2) proton discharge due to electron transfer at Pd and formation of adsorbed hydrogen, $H^+ + e^- \rightarrow H_{ad}$, (3) surface diffusion of H_{ad} on Pd and spillover to the Au support, (4) recombination, $2H_{ad} \rightarrow H_{2,ad}$, and desorption of molecular hydrogen, $H_{2,ad} \rightarrow H_2$. The largest mean distance between two Pd nano-islands in the investigated samples was about 10 nm. It seems that the hydrogen will cover the whole surface after several nano seconds if there is enough supplied hydrogen at the Pd nano-islands. The calculated adsorption rate of hydrogen at single supported Pd nanoparticle on gold is three orders of magnitude higher than the desorption rate [14]. Therefore, enough hydrogen will be supplied at the Pd nano-islands for the spillover process. Another indicator of the hydrogen evolution kinetics of the investigated samples is

the value of the Tafel slopes. At overpotentials smaller than 80 mV the Tafel slope is about 50 mV/dec and for larger overpotentials it is about 120 mV/dec (see Fig.5.3). This result demonstrates that there are two different kinetic processes dominant over and below 80 mV overpotential, respectively. At lower over-potentials the adsorption rate is low but still larger than the desorption rate. The last one is reduced due to the lower hydrogen coverage on the electrode surface. The adsorption of hydrogen occurs only at the Pd nano-islands. Due to the limited Pd surface sites, the hydrogen coverage will increase rapidly occupying the whole surface of the Pd nano-island. Then the hydrogen will spillover from the Pd nano-island to the Au(111) surface and leave free Pd sites which will be immediately filled with a new adsorbed hydrogen. After a defined time the diffusion front will spread onto the whole Au(111) surface, due to the fast surface diffusion of the adsorbed hydrogen onto the Au [115] and the higher hydrogen adsorption rate on Pd [14]. Thus, as long as the Au surface remins not fully occupied, the rate-determining step (rds) will be the hydrogen adsorption on Pd nano-islands at higher coverage. Immediately after covering the whole Au(111) surface with hydrogen the rate determining step will be changed to the hydrogen desorption. The Tafel slopes corresponding to both rate determining steps are 39 mV/dec and 119 mV/dec [46, 106], respectively. The last fact is in a good agreement with the experimental results.
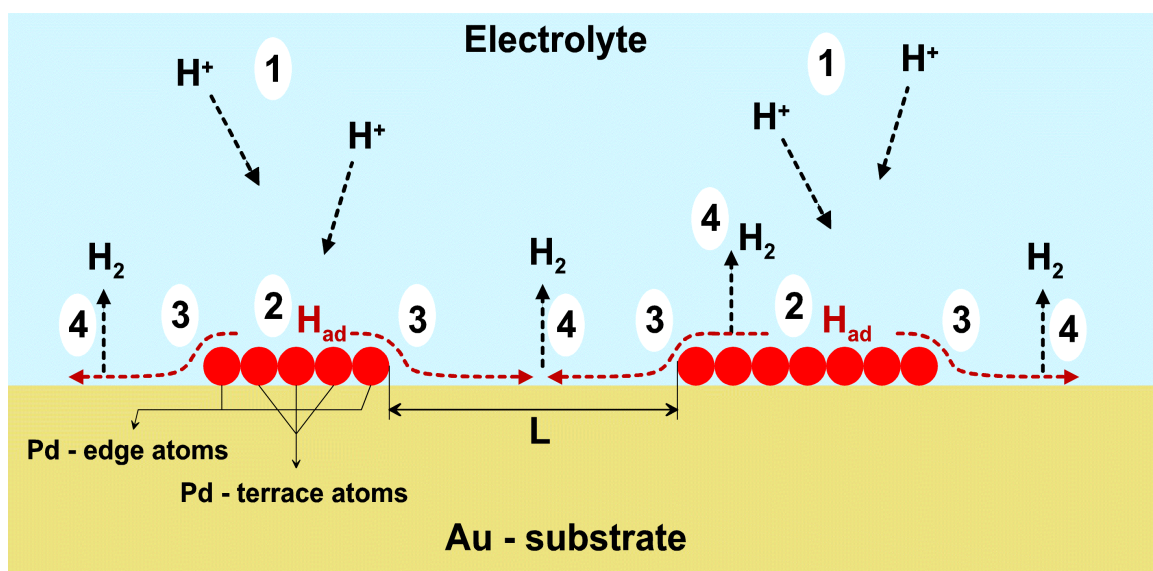
Fig.D.1: Illustration of the processes on the substrate surface involved in the reduction of protons: (1) bulk diffusion of protons, (2) proton discharge and formation of adsorbed hydrogen, (3) spillover and surface diffusion of adsorbed hydrogen and (4) recombination and desorption of molecular hydrogen.

Preliminary theoretical results, which support the spillover effect of hydrogen from Pd to Au, are shown in Fig.D.2. The calculated hydrogen coverages on Au and Pd are presented as a function of the electrode potential. Nørskov and coworkers [116] developed a method where the free energy (adsorption energy) of the reaction $H^+ + e^- \rightarrow H_{ad}$ is related to the electrode potential. The data of Fig.D.2 can be used for the estimation of the lowest possible barrier for the hydrogen spillover from Pd to the Au substrate at a given potential. For instance, the vertical distance between the point where the Pd line cuts the $U = -0.2\,V$ line and the low coverage Au point gives an indication of the spillover barrier at potential $-0.2\,V$. The barrier height of hydrogen spillover will decrease with lowering the potential and at around $-0.4\,V$ will be essentially zero. Due to the difference in the surface coverage and the small energy barrier the hydrogen will spillover from the Pd surface (with large H coverage) to the Au surface (with low H coverage). The electrode potential is strongly related to the spillover barrier height. Thus, if the hydrogen spillover is the rate-determining step, the reaction rate will be also potential dependent.
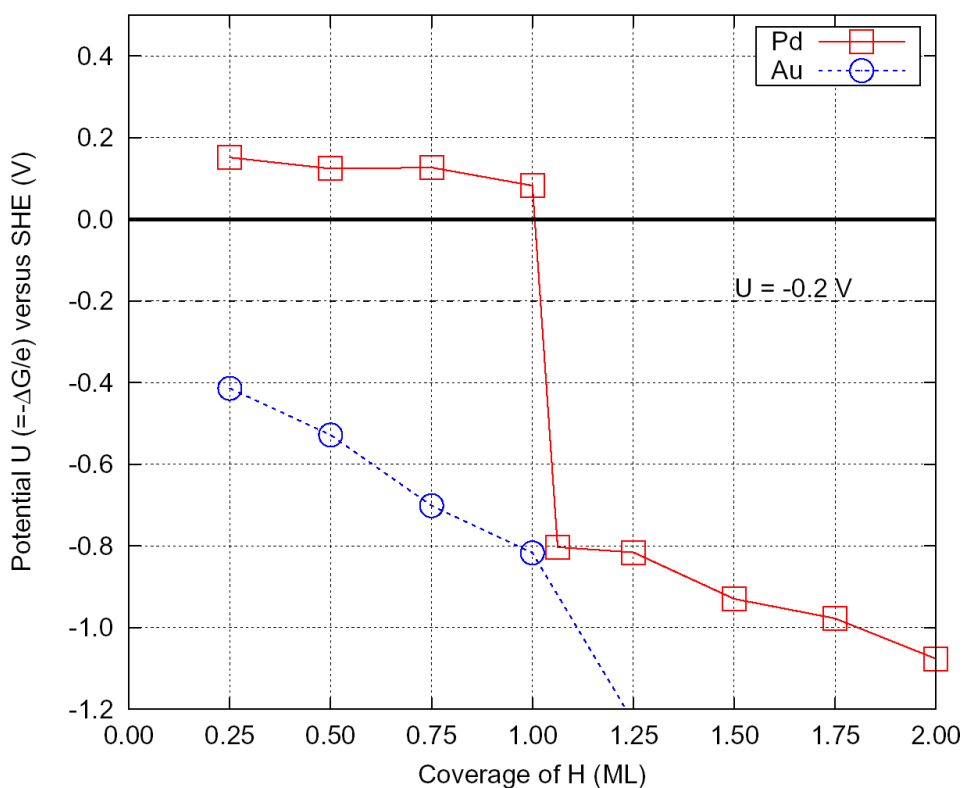
Fig.D.2: Hydrogen coverage at $pH = 0$ on Au and Pd as a function of the electrode potential (hydrogen adsorption energy) relative to the standard hydrogen potential [116].

Due to the spill over effect the rate determining step in the hydrogen evolution reaction on Pd nano-islands on Au(111) is the hydrogen adsorption ("Volmer" step). In case of extended Pd surfaces and Pd monolayers on Au (111) the rds is the hydrogen recombination and desorption the rate of which is much lower than the rate of hydrogen adsorption, especially if the adsorption rate is enhanced due to structural/electronic effects. The electronic effects are due to strain in the lattice of the supported Pd on Au (111). They affect the hydrogen adsorption energy [15, 17, 19, 21] and thus the hydrogen adsorption rate. The influence of electronic effects on the hydrogen evolution reaction can be observed only in systems with a rate determining hydrogen adsorption step, namely Pd nano-islands on Au (111). Therefore the enhanced reactivity of the hydrogen evolution reaction in the case of sub-monolayers of Pd on Au (111) as compared to a single complete monolayer Pd can be explained by electronic effects due to Hammer and Nørskov [15-17].

Summary

The interest in very small particles or nanoparticles, originates from their special physical properties. They are not only of fundamental importance, but also of interest for many potential applications such as heterogeneous catalysis. The Scanning Tunneling Microscopy (STM) was employed to study the formation and growth properties of small palladium nano-islands and monolayers, supported on Au(111) substrate. The standard electrochemical techniques, such as galvanostatic transients and cyclic voltammometry was used for reactivity measurements, regarding hydrogen evolution reaction and characterization of the Pd/Au(111) systems.

Only clean, well ordered Au(111) surfaces can serve as substrates for the deposition of Pd nano-islands and monolayers. The preparation and characterization of the Au(111) surfaces were presented in chapter 2. Furthermore, the fabrication of sharp STM tips and pH nano-sensor are discussed. It was found that hydrogen loaded Pd STM-tip can serve as a pH nano-sensor.

In chapter 3, the deposition of Pd on Au(111) from 0.5 mM $Pd(NO_3)_2$ in 0.1 M $HClO_4$ solution was described. According to the author's knowledge, the deposition of Pd on Au(111) in this solution has been performed for the first time. The potential pulse technique was engaged in order to produce Pd monoatomic high nano-islands on Au(111) with a narrow size distribution. Varying the duration and the amplitude of the pulse, the island size and the island number density were controlled. In addition, combining the potential pulse and the potentiostatic techniques a wide range of nano-islands size distributions were obtained. The smallest achieved distribution was from 0 to 3.8 nm, with a average nano-island diameter of 1.2 nm. Two-dimensional growth of up to two monolayers of palladium was reached by a stepwise increase of the overpotential. The deposition of the first monolayer Pd on Au(111) from the used solution, reveal fast deposition kinetics compared to the values published in the literature [33]. The palladium nucleation in the used solution have been found to begin spontaneously at the whole Au(111) surface without preferred surface areas.

Chapter 4 presents the characterization of the deposited Pd/Au(111) systems by cyclic voltammometry, EC-STM, FTIR and XPS measurements. The oxidation-reduction potentials of 1 ML Pd was different from that one for two and more monolayers Pd on Au(111). It was pointed out that a NO adlayer is adsorbed on top of the deposited first Pd layer, which lowered the deposition kinetics of the second Pd monolayer. The NO reduction procedure was developed and described. After the NO reduction procedure the surface was free from any adsorbate and ready for further electrochemical investigations. The last fact was verified by FTIR spectroscopy study. The stability of the deposited Pd nano-islands in 0.1 M HClO$_4$ solution was stable to a long time, allowing reactivity measurements. Even after oxidation-reduction cycles the nano-islands were stable, but with monoatomically deep holes in the middle (called nano-rings). The surface was investigated with *in-situ* STM images, which shows the Pd nano-rings on Au(111). The possible reason of formation of the nano-rings was discussed. Furthermore, an algorithm developed to determine the number, the sizes and the perimeters of the Pd nano-islands in STM images was described. It was verified that the ratio N_e/N_t show an reciprocal proportionality to the mean nano-island diameter. Additionally, the energy position of Pd(3d) core level *d*-lines of Pd/Au(111) samples with different Pd coverage was investigated by X-ray photo-electron spectroscopy. The XPS measurements show almost no shift (40 meV) in the *d*-band of Pd monolayers on Au(111). The observed shift was in the range of the device spatial resolution. The evaluated spectra revealed a good agreement between XPS intensity data and the coulometric measurements regarding palladium coverage.

In the last chapter the reactivity measurements with respect to hydrogen evolution reaction at Pd deposits in 0.1 M HClO$_4$ solution are described. The study was performed by galvanostatic transients, which were recorded with time duration of 60 ms. The evaluation procedure of the transient was also explained. The estimated data were presented as Tafel plots. The hydrogen reduction rate increases with decreasing the numbers of layers by a factor of three, and it is enhanced by up to two orders of magnitude for partial coverage down to 0.035 ML. The effect of coverage is so strong that even the current density per geometric area increases with decreasing coverage. There is no significant dependence of the current density for hydrogen evolution on the number of edge *vs.* terrace atoms, similar to the results of the single particle experiments [11, 12, 47]. Furthermore, a physical model and fit of the Tafel plot are presented. While there seems to be a consistent explanation for

the experimental data for hydrogen evolution on single and multiple Pd nanoparticles on Au(111) with respect to an involvement of the free Au surface in the reaction, a consistent physical model was proposed.

List of Symbols

B	Single beam FTIR spectrum, in a.u.
B_n	Single beam FTIR spectrum of the n potential step, in a.u.
c	concentration, in mol cm^{-3}
c_{H^+}	concentration of the H^+ ions in the solution, in mol cm^{-3}
$c_{Me^{z+}}$	concentration of the metal ions Me^{z+} in the solution, in mol cm^{-3}
C_{DL}	double layer capacity, in F cm^{-2}
d	thickness of the Pd deposits, in m
d_0	bulk interatomic distance, in m
e^-	electron
E_{kin}	kinetic energy of the photoelectrons, in eV
E_F	Fermi energy, in eV
g	change of the free energy of adsorption with coverage under Temkin conditions
i_p	current peak height, in A
I_T	tunneling current, in A
j	current density, in A m^{-2}
j_F	Faradaic current density, in A m^{-2}
j_L	Diffusion limited current density, in A m^{-2}
k_N	nucleation rate constant, in s^{-1}
k_i	reaction rate constants of step i, in mol cm^{-2} s^{-1}
mf	crystallographic misfit
$M_{ads.}$	deposited metal ions
$M_{solv.}$	solvated metal ions
n	number of the used electrons in the reaction
$N(t)$	number of the nucleation centers
N_∞	number of the active sites on the electrode surface
N_e	number of Pd edge atoms
N_t	number of Pd terrace atoms
$N_{Au,Pd}$	relative atom mass of Au,Pd
q_{max}	saturation charge, in C cm^{-2}

Q	charge density, in C cm^{-2}
r	number of transferred electrons in rate determining step (rds)
r_0	center of the tip radius
R	tip radius, in m
R_F	Faradaic resistance of the electrolyte, in Ω
s	tunneling distance (distance tip-sample), in m
t	time, in s
T	temperature, in K
U	electrode potential, in V
U_0	Nernst potential of the electrode, in V
U^θ	Standart potential of the electrode, in V
U_T	tunneling bias, iv V
U_i	initial potential, in V
U_f	final potential, in V
U_{WE}	Working electrode potential, in V
U_{CE}	Counter electrode potential, in V
U_i	initial potential, in V
v	sweep rate, in V/s
V_i	reaction rate of step i, in mol cm^{-2} s^{-1}

Greek symbols

$\alpha_{a,c}$	anodic, cathodic transfer coefficient
α_{eff}	effective transfer coefficient
β	symmetry factor
γ	electrons transferred in the steps preceding the rate-determining step (rds)
δ	diffusion layer thickness, in m
$\zeta_{T,S}$	density of states *tip,sample*
η	overpotential, V
θ	surface coverage by adsorbed intermediates
θ_H	hydrogen surface coverage
$\theta_{H,0}$	steady state hydrogen surface coverage

$\lambda_{Au,Pd}$	free path length of the electrons, in m
μ_i	electrochemical potential, in J mol^{-1}
σ	saturation value of adsorbed intermediates, in mol cm^{-2}
τ	relaxation time of the double layer, in s
υ	number of rds repetitions per single cycle of the overall reaction
$\Upsilon_{Pd,Au}$	XPS spectra intensity, in a.u.
ϕ_{tip}	work function of the tip, in eV
ϕ_{sample}	work function of the sample, in eV
Φ_T	tunneling barrier height, in eV
Ψ	binding energy, in eV

Bibliography

[1]   Baldauf, M. and D.M. Kolb. A Hydrogen Adsorption and Absorption Study with Ultrathin Pd Overlayers on Au(111) and Au(100). *Electrochimica Acta*, **38**(15): p. 2145-2153, 1993.

[2]   Baldauf, M. and D.M. Kolb. Formic acid oxidation on ultrathin Pd films on Au(hkl) and Pt(hkl) electrodes. *Journal of Physical Chemistry*, **100**(27): p. 11375-11381, 1996.

[3]   El-Aziz, A.M. and L.A. Kibler. Influence of steps on the electrochemical oxidation of CO adlayers on Pd(111) and on Pd films electrodeposited onto Au(111). *Journal of Electroanalytical Chemistry*, **534**(2): p. 107-114, 2002.

[4]   El-Aziz, A.M., L.A. Kibler, and D.M. Kolb. The potentials of zero charge of Pd(111) and thin Pd overlayers on Au(111). *Electrochemistry Communications*, **4**(7): p. 535-539, 2002.

[5]   Kibler, L.A. Hydrogen electrocatalysis. *Chemphyschem*, **7**(5): p. 985-991, 2006.

[6]   Kibler, L.A., *et al.* Tuning reaction rates by lateral strain in a palladium monolayer. *Angewandte Chemie-International Edition*, **44**(14): p. 2080-2084, 2005.

[7]   Kibler, L.A., A.M. El-Aziz, and D.M. Kolb. Electrochemical behaviour of pseudomorphic overlayers: Pd on Au(111). *Journal of Molecular Catalysis a-Chemical*, **199**(1-2): p. 57-63, 2003.

[8]   Naohara, H., S. Ye, and K. Uosaki. Thickness dependent electrochemical reactivity of epitaxially electrodeposited palladium thin layers on Au(111) and Au(100) surfaces. *Journal of Electroanalytical Chemistry*, **500**(1-2): p. 435-445, 2001.

[9]   Naohara, H., S. Ye, and K. Uosaki. Electrocatalytic reactivity for oxygen reduction at epitaxially grown Pd thin layers of various thickness on Au(111) and Au(100). *Electrochimica Acta*, **45**(20): p. 3305-3309, 2000.

[10]   Uosaki, K., *et al.* Keynote lecture: Electrochemical epitaxial growth, structure, and electrocatalytic properties of noble metal thin films on Au(111) and Bu(100). *Abstracts of Papers of the American Chemical Society*, **221**: p. U326-U326, 2001.

[11]   Meier, J., *et al.* Nano-scale effects in electrochemistry. *Chemical Physics Letters*, **390**(4-6): p. 440-444, 2004.

[12]   Meier, J., H. Kleine, and U. Stimming. Investigations of the stability of palladium clusters supported on gold. *Surface Science*, **597**(1-3): p. 127-132, 2005.

[13]   Meier, J., K.A. Friedrich, and U. Stimming. Novel method for the investigation of single nanoparticle reactivity. *Faraday Discussions*, **121**: p. 365-372, 2002.

[14]   Eikerling, M., J. Meier, and U. Stimming. Hydrogen evolution at a single supported nanoparticle: A kinetic model. *Zeitschrift Fur Physikalische Chemie-International Journal of Research in Physical Chemistry & Chemical Physics*, **217**(4): p. 395-414, 2003.

[15]   Hammer, B. and J.K. Norskov. Electronic factors determining the reactivity of metal surfaces. *Surface Science*, **343**(3): p. 211-220, 1995.

[16]   Hammer, B. and J.K. Norskov. Electronic factors determining the reactivity of metal surfaces (vol 343, pg 211, 1995). *Surface Science*, **359**(1-3): p. 306-306, 1996.

[17]   Hammer, B. and J.K. Norskov. Theoretical surface science and catalysis - Calculations and concepts. *Advances in Catalysis, Vol 45*, **45**: p. 71-129, 2000.

[18]   Kitchin, J.R., *et al.* Role of strain and ligand effects in the modification of the electronic and chemical properties of bimetallic surfaces. *Physical Review Letters*, **93**(15): p. -, 2004.

[19]   Norskov, J.K. Catalysis from first principles. *Reaction Kinetics and the Development of Catalytic Processes*, **122**: p. 3-10, 1999.

[20]   Norskov, J.K., et al. Universality in heterogeneous catalysis. *Journal of Catalysis*, **209**(2): p. 275-278, 2002.

[21]   Norskov, J.K., *et al.* Electronic factors determining the reactivity of metal surfaces. *Abstracts of Papers of the American Chemical Society*, **211**: p. 5-Phys, 1996.

[22]   Roudgar, A. and A. Gross. Local reactivity of thin Pd overlayers on Au single crystals. *Journal of Electroanalytical Chemistry*, **548**: p. 121-130, 2003.

[23]   Roudgar, A. and A. Gross. Local reactivity of metal overlayers: Density functional theory calculations of Pd on Au. *Physical Review B*, **67**(3): p. 033409, 2003.

[24]   Ruban, A., *et al.* Surface electronic structure and reactivity of transition and noble metals. *Journal of Molecular Catalysis a-Chemical*, **115**(3): p. 421-429, 1997.

[25]   Ruban, A.V., H.L. Skriver, and J.K. Norskov. Surface segregation energies in transition-metal alloys. *Physical Review B*, **59**(24): p. 15990-16000, 1999.

[26]   Rojas, M.I., M.G. Del Popolo, and E.P.M. Leiva. Simulation study of Pd submonolayer films on Au(hkl) and Pt(hkl) and their relationship to underpotential deposition. *Langmuir*, **16**(24): p. 9539-9546, 2000.

[27]   Rojas, M.I., *et al.* An embedded atom approach to underpotential deposition phenomena (vol 421, pg 59, 1999). *Surface Science*, **453**(1-3): p. 225-228, 2000.

[28]   Budevski, E.B., G.T. Staikov, and W.J. Lorenz. *Electrochemical Phase Formation and Growth.* Wiley, New York, 1996.

[29]   Paunovic, M. and M. Schlesinger. *Fundamentals of Electrochemical Deposition.* Wiley, New York, 1998.

[30]   Naohara, H., S. Ye, and K. Uosaki. Epitaxial growth of a palladium layer on an Au(100) electrode. *Journal of Electroanalytical Chemistry*, **473**(1-2): p. 2-9, 1999.

[31]   Naohara, H., S. Ye, and K. Uosaki. Electrochemical deposition of palladium on an Au(111) electrode: effects of adsorbed hydrogen for a growth mode. *Colloids and Surfaces a-Physicochemical and Engineering Aspects*, **154**(1-2): p. 201-208, 1999.

[32]   Kibler, L.A., *et al.* Initial stages of Pd deposition on Au(hkl) - Part I: Pd on Au(111). *Surface Science*, **443**(1-2): p. 19-30, 1999.

[33]   Tang, J., *et al.* Pd deposition onto Au(111) electrodes from sulphuric acid solution. *Electrochimica Acta*, **51**(1): p. 125-132, 2005.

[34]   Binning, G., *et al.* Surface Studies by Scanning Tunneling Microscopy. *Physical Review Letters*, **49**(1): p. 57-61, 1982.

[35]   Simmons, J.G. Generalized Formula for Electric Tunnel Effect between Similar Electrodes Separated by a Thin Insulating Film. *Journal of Applied Physics*, **34**(6): p. 1793-&, 1963.

[36]   Tersoff, J. and D.R. Hamann. Theory of the Scanning Tunneling Microscope. *Physical Review B*, **31**(2): p. 805-813, 1985.

[37]   Tersoff, J. and D.R. Hamann. Theory and Application for the Scanning Tunneling Microscope. *Physical Review Letters*, **50**(25): p. 1998-2001, 1983.

[38]   Hansma, P.K. and J. Tersoff. Scanning Tunneling Microscopy. *Journal of Applied Physics*, **61**(2): p. R1-R23, 1987.

[39]   Haiss, W., *et al.* Atomic Resolution Scanning Tunneling Microscopy Images of Au(111) Surfaces in Air and Polar Organic-Solvents. *Journal of Chemical Physics*, **95**(3): p. 2193-2196, 1991.

[40]   Zhang, X.G.G. and U. Stimming. The Use of Time-Resolved Scanning Tunneling Microscopy for the Determination of Microscopic Reaction-Rates. *Journal of Electroanalytical Chemistry*, **291**(1-2): p. 273-279, 1990.

[41]   Hugelmann, M. and W. Schindler. Tunnel barrier height oscillations at the solid/liquid interface. *Surface Science*, **541**(1-3): p. L643-L648, 2003.

[42] Hamann, C.H., A. Hamnett, and W. Vielstich. *Electrochemistry.* 2 ed, Wiley-VCH, Weinheim, 1998.

[43] Bockris, J.O.M. and A.K.N. Reddy. *Modern Electrochemistry 2.* 20 ed, Plenum, New York, 1970.

[44] Schmickler, W. *Interfacial Electrochemistry.* Oxford University Press, New York, 1996.

[45] Vetter, K.J. *Electrochemical Kinetics.* Academic Press, New York, 1967.

[46] Tilak, B.V. and C.P. Chen. Generalized Analytical Expressions for Tafel Slope, Reaction Order and Ac Impedance for the Hydrogen Evolution Reaction (Her) - Mechanism of Her on Platinum in Alkaline Media. *Journal of Applied Electrochemistry*, **23**(6): p. 631-640, 1993.

[47] Meier, J. Generation, Characterization and Reactivity of Surface Inhomogeneities at the Interface Solid-Liquid, Ph.D Thesis, Technical University Munich, 2003.

[48] Wintterlin, J., *et al.* Atomic-Resolution Imaging of Close-Packed Metal-Surfaces by Scanning Tunneling Microscopy. *Physical Review Letters*, **62**(1): p. 59-62, 1989.

[49] Bach, C.E., *et al.* Effective Insulation of Scanning-Tunneling-Microscopy Tips for Electrochemical Studies Using an Electropainting Method. *Journal of the Electrochemical Society*, **140**(5): p. 1281-1284, 1993.

[50] Schneeweiss, M.A., *et al.* Anodic oxidation of Au(111). *Canadian Journal of Chemistry-Revue Canadienne De Chimie*, **75**(11): p. 1703-1709, 1997.

[51] Schneeweiss, M.A. and D.M. Kolb. Oxide formation on au(111) - An in situ STM study. *Solid State Ionics*, **94**(1-4): p. 171-179, 1997.

[52] Hamelin, A. Cyclic voltammetry at gold single-crystal surfaces .1. Behaviour at low-index faces. *Journal of Electroanalytical Chemistry*, **407**(1-2): p. 1-11, 1996.

[53] Hamelin, A. and A.M. Martins. Cyclic voltammetry at gold single-crystal surfaces .2. Behaviour of high-index faces. *Journal of Electroanalytical Chemistry*, **407**(1-2): p. 13-21, 1996.

[54] Wolfe, R.C., *et al.* Measurement of pH gradients in the crevice corrosion of iron using a palladium hydride microelectrode. *Journal of the Electrochemical Society*, **152**(2): p. B82-B88, 2005.

[55] Eastman, J.A., L.J. Thompson, and B.J. Kestel. Narrowing of the Palladium-Hydrogen Miscibility Gap in Nanocrystalline Palladium. *Physical Review B*, **48**(1): p. 84-92, 1993.

[56]   Vasile, M.J. and C.G. Enke. Preparation and Thermodynamic Properties of a Palladium-Hydrogen Electrode. *Journal of the Electrochemical Society*, **112**(8): p. 865-&, 1965.

[57]   Yang, T.H., S. Pyun, and Y. Yoon. Hydrogen transport through Pd electrode: Current transient analysis. *Electrochimica Acta*, **42**(11): p. 1701-1708, 1997.

[58]   Karagounis, V.A., *et al.* A Pd-Pdo Film Potentiometric Ph Sensor. *Ieee Transactions on Biomedical Engineering*, **33**(2): p. 113-116, 1986.

[59]   Bloor, L.J. and D.J. Malcolmelawes. An Electrochemical Preparation of Palladium Oxide Ph Sensors. *Journal of Electroanalytical Chemistry*, **278**(1-2): p. 161-173, 1990.

[60]   Dobson, J.V. Potentials of Palladium Hydride Reference Electrode between 25 Degrees and 195 Degrees C. *Journal of Electroanalytical Chemistry*, **35**(NMAR): p. 129-&, 1972.

[61]   Flanagan, T.B. and W.A. Oates. The Palladium-Hydrogen System. *Annual Review of Materials Science*, **21**: p. 269-304, 1991.

[62]   Glab, S., *et al.* Metal-Metal Oxide and Metal-Oxide Electrodes as Ph Sensors. *Critical Reviews in Analytical Chemistry*, **21**(1): p. 29-47, 1989.

[63]   Grubb, W.T. and L.H. King. Palladium-Palladium Oxide Ph Electrodes. *Analytical Chemistry*, **52**(2): p. 270-273, 1980.

[64]   Liu, C.C., *et al.* Palladium - Palladium Oxide Miniature Ph Electrode. *Science*, **207**(4427): p. 188-189, 1980.

[65]   Macdonald, D.D., P.R. Wentrcek, and A.C. Scott. The Measurement of Ph in Aqueous Systems at Elevated-Temperatures Using Palladium Hydride Electrodes. *Journal of the Electrochemical Society*, **127**(8): p. 1745-1751, 1980.

[66]   Vracar, L.M., D.B. Sepa, and A. Damjanovic. Palladium Electrode in Oxygen Saturated Solutions - Rest Potentials in Solutions of Different Ph. *Journal of the Electrochemical Society*, **134**(7): p. 1695-1697, 1987.

[67]   Naohara, H., S. Ye, and K. Uosaki. Electrochemical layer-by-layer growth of palladium on an Au(111) electrode surface: Evidence for important role of adsorbed Pd complex. *Journal of Physical Chemistry B*, **102**(22): p. 4366-4373, 1998.

[68]   Wang, J. *Analytical Electrochemistry.* Chapter 2, John Wiley & Sons, New York, 2000.

[69]   Nicholson, R.S. and I. Shain. Theory of Stationary Electrode Polarography - Single Scan + Cyclic Methods Applied to Reversible Irreversible + Kinetic Systems. *Analytical Chemistry*, **36**(4): p. 706-&, 1964.

[70]   Kolb, D.M. Reconstruction phenomena at metal-electrolyte interfaces. *Progress in Surface Science*, **51**(2): p. 109-173, 1996.

[71]   Maillard, F., *et al*. Infrared spectroscopic study of CO adsorption and electro-oxidation on carbon-supported Pt nanoparticles: Interparticle versus intraparticle heterogeneity. *Journal of Physical Chemistry B*, **108**(46): p. 17893-17904, 2004.

[72]   Rosca, V. and M.T.M. Koper. Mechanism of electrocatalytic reduction of nitric oxide on Pt(100). *Journal of Physical Chemistry B*, **109**(35): p. 16750-16759, 2005.

[73]   Rosca, V., G.L. Beltramo, and M.T.M. Koper. Reduction of NO adlayers on Pt(110) and Pt(111) in acidic media: Evidence for adsorption site-specific reduction. *Langmuir*, **21**(4): p. 1448-1456, 2005.

[74]   de Vooys, A.C.A., *et al*. Mechanistic study on the electrocatalytic reduction of nitric oxide on transition-metal electrodes. *Journal of Catalysis*, **202**(2): p. 387-394, 2001.

[75]   de Vooys, A.C.A., *et al*. The nature of chemisorbates formed from ammonia on gold and palladium electrodes as discerned from surface-enhanced Raman spectroscopy. *Electrochemistry Communications*, **3**(6): p. 293-298, 2001.

[76]   de Vooys, A.C.A., *et al*. The role of adsorbates in the electrochemical oxidation of ammonia on noble and transition metal electrodes. *Journal of Electroanalytical Chemistry*, **506**(2): p. 127-137, 2001.

[77]   de Vooys, A.C.A., *et al*. Mechanisms of electrochemical reduction and oxidation of nitric oxide. *Electrochimica Acta*, **49**(8): p. 1307-1314, 2004.

[78]   Bagus, P.S., *et al*. Mechanisms responsible for chemical shifts of core-level binding energies and their relationship to chemical bonding. *Journal of Electron Spectroscopy and Related Phenomena*, **100**: p. 215-236, 1999.

[79]   Mavrikakis, M., B. Hammer, and J.K. Norskov. Effect of strain on the reactivity of metal surfaces. *Physical Review Letters*, **81**(13): p. 2819-2822, 1998.

[80]   Rodriguez, J.A., R.A. Campbell, and D.W. Goodman. Electron-Donor Electron-Acceptor Interactions in Bimetallic Surfaces - Theory and Xps Studies. *Journal of Physical Chemistry*, **95**(15): p. 5716-5719, 1991.

[81]   Sellidj, A. and B.E. Koel. Electronic and Co Chemisorption Properties of Ultrathin Pd Films Vapor-Deposited On Au(111). *Physical Review B*, **49**(12): p. 8367-8376, 1994.

[82]   Nascente, P.A.P., *et al.* X-Ray Photoemission and Auger Energy Shifts in Some Gold-Palladium Alloys. *Physical Review B*, **43**(6): p. 4659-4666, 1991.

[83]   Mojet, B.L., *et al.* A new model describing the metal-support interaction in noble metal catalysts. *Journal of Catalysis*, **186**(2): p. 373-386, 1999.

[84]   Koel, B.E., A. Sellidj, and M.T. Paffett. Ultrathin Films of Pd On Au(111) - Evidence For Surface Alloy Formation. *Physical Review B*, **46**(12): p. 7846-7856, 1992.

[85]   Hillebrecht, F.U., *et al.* Electronic-Structure of Ni and Pd Alloys .2. X-Ray Photoelectron Core-Level Spectra. *Physical Review B*, **27**(4): p. 2179-2193, 1983.

[86]   Hillebrecht, F.U., *et al.* Split-Off Narrow D-Band States Above Ef in Transition-Metal Alloys. *Physical Review Letters*, **51**(13): p. 1187-1190, 1983.

[87]   Grasso, V. and L. Silipigni. X-ray photoemission spectra and x-ray excited Auger spectrum investigation of the electronic structure of Pd-3(PS4)(2). *Journal of Vacuum Science & Technology a*, **21**(4): p. 860-865, 2003.

[88]   Brun, M., A. Berthet, and J.C. Bertolini. XPS, AES and Auger parameter of Pd and PdO. *Journal of Electron Spectroscopy and Related Phenomena*, **104**(1-3): p. 55-60, 1999.

[89]   Hammer, B., Y. Morikawa, and J.K. Norskov. CO chemisorption at metal surfaces and overlayers. *Physical Review Letters*, **76**(12): p. 2141-2144, 1996.

[90]   GandugliaPirovano, M.V., *et al.* Potential, core-level, and d band shifts at transition-metal surfaces. *Physical Review B*, **54**(12): p. 8892-8898, 1996.

[91]   Weinert, M. and R.E. Watson. Core-Level Shifts in Bulk Alloys and Surface Adlayers. *Physical Review B*, **51**(23): p. 17168-17180, 1995.

[92]   Hennig, D., M.V. GandugliaPirovano, and M. Scheffler. Adlayer core-level shifts of admetal monolayers on transition-metal substrates and their relation to the surface chemical reactivity. *Physical Review B*, **53**(15): p. 10344-10347, 1996.

[93]   Roudgar, A. and A. Gross. Local reactivity of supported metal clusters: Pd-n on Au(111). *Surface Science*, **559**(2-3): p. L180-L186, 2004.

[94]   Morf, W.E. Theoretical treatment of the amperometric current response of multiple microelectrode arrays. *Analytica Chimica Acta*, **330**(2-3): p. 139-149, 1996.

[95]   Morf, W.E. and N.F. de Rooij. Performance of amperometric sensors based on multiple microelectrode arrays. *Sensors and Actuators B-Chemical*, **44**(1-3): p. 538-541, 1997.

[96]   Morf, W.E., M. Koudelka-Hep, and N.F. de Rooij. Theoretical treatment and computer simulation of microelectrode arrays. *Journal of Electroanalytical Chemistry*, **590**(1): p. 47-56, 2006.

[97]   Wittstock, G., *et al.* Evaluation of microelectrode arrays for amperometric detection by scanning electrochemical microscopy. *Electroanalysis*, **10**(8): p. 526-531, 1998.

[98]   Wittstock, G. Sensor arrays and array sensors. *Analytical and Bioanalytical Chemistry*, **372**(1): p. 16-17, 2002.

[99]   Sandison, M.E., *et al.* Optimization of the geometry and porosity of microelectrode arrays for sensor design. *Analytical Chemistry*, **74**(22): p. 5717-5725, 2002.

[100]   Macpherson, J.V. and P.R. Unwin. Determination of the diffusion coefficient of hydrogen in aqueous solution using single and double potential step chronoamperometry at a disk ultramicroelectrode. *Analytical Chemistry*, **69**(11): p. 2063-2069, 1997.

[101]   Lenigk, R., *et al.* Recessed microelectrode array for a micro flow-through system allowing on-line multianalyte determination in vivo. *Fresenius Journal of Analytical Chemistry*, **364**(1-2): p. 66-71, 1999.

[102]   Feeney, R. and S.P. Kounaves. Microfabricated ultramicroelectrode arrays: Developments, advances, and applications in environmental analysis. *Electroanalysis*, **12**(9): p. 677-684, 2000.

[103]   Conway, B.E. and L. Bai. Determination of Adsorption of Opd H Species in the Cathodic Hydrogen Evolution Reaction at Pt in Relation to Electrocatalysis. *Journal of Electroanalytical Chemistry*, **198**(1): p. 149-175, 1986.

[104]   Conway, B.E. and L. Bai. State of Adsorption and Coverage by Overpotential-Deposited H in the H-2 Evolution Reaction at Au and Pt. *Electrochimica Acta*, **31**(8): p. 1013-1024, 1986.

[105]   Conway, B.E. and E. Gileadi. Kinetic Theory of Pseudo-Capacitance and Electrode Reactions at Appreciable Surface Coverage. *Transactions of the Faraday Society*, **58**(DEC): p. 2493-&, 1962.

[106]   Tavares, M.C., S.A.S. Machado, and L.H. Mazo. Study of hydrogen evolution reaction in acid medium on Pt micro electrodes. *Electrochimica Acta*, **46**(28): p. 4359-4369, 2001.

[107]   Dogonadze, R.R. and A.M. Kuznetsov. Electron-Transfer Rates in Levich and Dogonadze Theory of Redox Reactions - Comment W,Schmickler and W,Vielstich. *Electrochimica Acta*, **19**(12): p. 961-962, 1974.

[108] Conner, W.C. and J.L. Falconer. Spillover in Heterogeneous Catalysis. *Chemical Reviews*, **95**(3): p. 759-788, 1995.

[109] Machida, M., D. Kurogi, and T. Kijima. Role of hydrogen-spillover in H-2-NO reaction over Pd-supported NOx-adsorbing material, MnOx-CeO2. *Journal of Physical Chemistry B*, **107**(1): p. 196-202, 2003.

[110] Roland, U., R. Salzer, and S. Stolle. Investigation of Hydrogen and Deuterium Spillover on Y-Zeolites by Ft-Ir Microscopy - Rate-Determining Steps. *Zeolites and Related Microporous Materials: State of the Art 1994*, **84**: p. 1231-1238, 1994.

[111] Roland, U., *et al.* Investigations on Hydrogen Spillover .1. Electrical-Conductivity Studies on Titanium-Dioxide. *Journal of the Chemical Society-Faraday Transactions*, **91**(7): p. 1091-1095, 1995.

[112] Roland, U., R. Salzer, and L. Summchen. Electronic effects of hydrogen spillover on titania. *Spillover and Migration of Surface Species on Catalysts*, **112**: p. 339-348, 1997.

[113] Vayssilov, G.N. and N. Rosch. Reverse hydrogen spillover in supported subnanosize clusters of the metals of groups 8 to 11. A computational model study. *Physical Chemistry Chemical Physics*, **7**(23): p. 4019-4026, 2005.

[114] Bard, A.J. and L.R. Faulkner. *Electrochemical Methods-Fundamentals and Applications.* 1 ed, John Wiley & Sons, New York, 1980.

[115] Su, L. and B.L. Wu. Investigation of surface diffusion and recombination reaction kinetics of H-adatoms in the process of the hydrogen evolution reaction (her) at Au electrodes. *Journal of Electroanalytical Chemistry*, **565**(1): p. 1-6, 2004.

[116] Karlberg, G. and J.K. Norskov. Unpublished results.

Acknowledgments

Here, I would like to thank to all those who have contributed to the successful completion of this work.

First of all, I would like to thank to Prof. Dr. Ulrich Stimming for the offered opportunity of taking my Ph.D. degree in the Physics Department of München Technical University and for his guidance.

I am thankful to Prof. Dr. Dr. h. c. Alfred Laubereau and Dr. Hristo Iglev for their support and encouragement to finish this thesis.

I want to thank Dr. habil. Werner Schindler and Dr. Jürgen Meier for their useful advice for resolving of experimental problems and many useful discussions.

Thanks to Dipl. -Phys. Sven Bugarski and Dr. Philipp Hugelmann for the nice atmosphere in our underground ISL laboratory.

I acknowledge Ms. Perta Bele for her English corrections of the thesis.

I am grateful to my parents for their love and support during all my study.

Special thanks I owe to my wife Marchela. She is the only one who really knows how much time and work was invested by this thesis. She never complained but was always there for me.

Last but not least I thank my son Kliment for the relaxing games and his sunny smiles.